2006-02-07

# Human Rad51: Regulation of Cellular Localization and Function in Response to DNA Damage: A Dissertation

Brian Thomas Bennett
*University of Massachusetts Medical School*

# Human Rad51: Regulation of Cellular Localization and Function in Response to DNA Damage

A Dissertation Presented

By

Brian Thomas Bennett

Submitted to the Faculty of the

University of Massachusetts Graduate School of Biomedical Sciences, Worcester

in partial fulfillment of the requirements for the degree of

DOCTOR OF PHILOSOPHY

February 7, 2006

Biochemistry and Molecular Pharmacology

Human Rad51: Regulation of Cellular Localization and Function in Response to DNA Damage

A Dissertation Presented

By

Brian Thomas Bennett

Approved as to style and content by:

_____
Craig L. Peterson, Ph.D., Chair of Committee

_____
Anthony Carruthers, Ph.D., Member of Committee

_____
Gary S. Stein, Ph.D., Member of Committee

_____
Steven Grossman, Ph.D. M.D., Member of Committee

_____
Douglas L. Pittman, Ph.D., Member of Committee

_____
Kendall L. Knight, Ph.D.,
Dissertation Mentor

_____
Anthony Carruthers, Ph.D., Dean of the Graduate school of Biomedical Sciences

Biochemistry and Molecular Pharmacology
February 7, 2006

## ACKNOWLEDGEMENTS

I would like to thank those who helped me achieve this first milestone in my scientific career. I want to thank Dr. Anthony Carruthers for his ability to see past the non-traditional background and find a place for me within the GSBS program, additionally my mentor, Dr. Ken Knight also looked past what most felt was a non-compatible background and provided the proving ground for my success. I want to thank family and friends for the support, former lab members, and those I worked with in Animal Medicine for never forgetting our time together and always greeting me with an encouraging word with regards to my future direction. Most of all I want to thank the majority, those who just did not think I had what it takes, those who said I could not succeed, for it was their doubt that drove me even harder.

## ABSTRACT

Repair of DNA double-strand breaks via homologous recombination is an essential pathway for vertebrate cell development and maintenance of genome integrity throughout the organism's lifetime. The Rad51 enzyme provides the central catalytic function of homologous recombination while many other proteins are involved in regulation and assistance of Rad51 activity, including a group of five proteins referred to as Rad51 paralogs (Rad51B, Rad51C, Rad51D, Xrcc2, Xrcc3). At the start of my work, cellular studies of human Rad51 (HsRad51) had shown only that it forms distinct nuclear foci in response to DNA damage. Additionally, no information regarding the cellular localization, potential DNA damage-induced redistribution or cellular functions for any of the Rad51 paralog proteins was available. Therefore, the goals of this work were to (**1**) present a more complete description of the cellular localization and DNA damage-induced redistribution of Rad51 and the two paralog proteins known to specifically associate with Rad51, Rad51C and Xrcc3, and (**2**) to define specific functional roles for Rad51C and Xrcc3 in mediating Rad51 activity. I focused on the use of cellular, RNAi and immunofluorescence methods to study endogenous Rad51, Rad51C and Xrcc3 in human cells.

In my initial studies we showed for the first time that Xrcc3 forms distinct foci in both the nucleus and cytoplasm independent of DNA damage, that the distribution of these foci did not change significantly throughout the time course of DNA damage and repair, and that Xrcc3 focus formation is independent of Rad51. Additionally, and unlike most previously published images of

nuclear Rad51, we found that the majority of DNA damage-induced nuclear Rad51 foci do not colocalize with gamma H2AX, a histone marker used to indicate the occurrence of DNA double strand breaks.

As a consequence of these initial outcomes, a significant amount of effort was devoted to developing and optimizing immunofluorescence methods. Importantly, we developed a purification method for commercially available monoclonal antibodies against Rad51C and Xrcc3 that significantly improved their reactivity and specificity. My next study concentrated on Rad51C. Similar to Xrcc3, we found for the first time that Rad51C forms distinct nuclear and cytoplasmic foci independent of DNA damage and Rad51. An additional and surprising outcome was our discovery that Rad51C plays an important role in regulating the ubiquitination and proteasome-mediated degradation of Rad51. While biochemical functions for Rad51 paralog proteins had been suggested in the literature, this was the first demonstration of a specific biochemical function for Rad51C that contributes directly to the Rad51 activity in the homologous recombination pathway. Our improved immunofluorescence methods allowed us to see the accumulation of Rad51, Rad51C and Xrcc3 at the nuclear periphery early in response to DNA damage, suggesting the existence of a DNA damage-dependent trafficking mechanism that promoted movement of these proteins from the cytoplasm to the nucleus. This led to further studies in which we show distinct co-localization of cytoplasmic Rad51 with actin as well as alpha and beta tubulin. Using both immunofluorescence and sub-cellular fractionation methods our recent results strongly suggest that trafficking of Rad51 to the nucleus in response to DNA damage

is regulated at least in part by its association with cytoskeletal proteins, and involves movement of both existing pools of Rad51 and newly synthesized protein.

In a particularly exciting development, in collaboration with Leica Microsystems and Dr. Joerg Bewersdorf at The Jackson Laboratory, Bar Harbor, ME., I have been able to exploit a new technology, 4Pi microscopy, to provide the first images of endogenous nuclear proteins using this method.

Results presented in this thesis have added significantly to a more complete understanding of cellular localization Rad51, Rad51C and Xrcc3, and have provided important insights into possible mechanisms of cellular trafficking of Rad51 in response to response to DNA damage. Additionally, we have defined a specific function for Rad51C in its regulation of Rad51 ubiquitination. These findings open several new avenues of investigation for furthering our understanding of the cellular and molecular functions of proteins with critical roles in the maintenance of genome integrity in human cells.

## TABLE OF CONTENTS

# LIST OF FIGURES

# CHAPTER I

## INTRODUCTION AND BACKGROUND

Cellular DNA continuously endures damage to its structure by both exogenous agents and as a result of inherent metabolic processes leading to single and double-stranded breaks. The inefficient response and/or repair of these breaks can lead to chromosomal aberrations and cell death. Therefore, preservation of genome integrity is a critically important function and the cell takes advantage of multiple pathways for the maintenance and repair of DNA. In eukaryotic cells the repair of potentially lethal DNA double-strand breaks can be accomplished by several pathways including non-homologous end joining, single-stranded annealing and homologous recombination with all exploiting very different mechanisms as well as varying levels of efficiency. Non-homologous end joining catalyzes the direct joining of broken DNA ends, requiring proteins with specific end binding properties as well as enzymes for end processing and ligation. Given that the DNA breaks are processed before ligation, non-homologous end joining is an error prone repair mechanism. Single-strand annealing also suffers from being error prone because end processing to expose complementary single-strand regions results in the loss of genetic information.

In contrast to the above two pathways, homologous recombinational DNA repair is an error free mechanism and is found in all free-living organisms. Recombination plays a critical role in both the repair of DNA damage resulting from exposure to chemical mutagens as well as in pathways inherent to all eukaryotic cells, e.g. proper segregation of replicated chromosomes into daughter cells (Thompson and Schild, 2002). The mechanism of homologous recombination requires the

use of an undamaged sister chromatid, or a homologous chromosome, and a recombinase enzyme that interacts with both the damaged and undamaged DNAs to engage in a homology directed search (Sung et al., 2003). Recombinases are highly conserved both structurally and functionally across all bacterial (RecA), archaeal (RadA) and eukaryotic (Rad51) organisms (Thompson and Schild, 2001; McGrew and Knight, 2003; Conway et al., 2004; Wu et al., 2004). In eukaryotes, optimal function of the Rad51 enzyme requires other proteins many of which belong to the *RAD52* epistasis group. In vertebrates, these include a set of 5 proteins referred to as Rad51 paralogs, Rad51B/L1, Rad51C/L2, Rad51D/L3, Xrcc2 and Xrcc3 (Paques and Haber, 1999; Takata et al., 2001; Essers et al., 2002) that were identified in complementation screens or by sequence comparison with Rad51 (Albala et al., 1997; Tambini et al., 1997; Cartwright et al., 1998; Dosanjh et al., 1998; Liu et al., 1998). Each has been shown to play an important role in support of Rad51 function, and some of the work presented here addresses functional relationships between Rad51 and the paralog proteins.

Genes in the *RAD52* epistasis group, including *RAD50*, *RAD51*, *RAD52*, *RAD54*, *RAD55*, *RAD57*, *RAD59*, *MRE11* and *XRS2*, were originally identified in yeast by the sensitivity of mutants to ionizing radiation (IR) (Petes et al., 1991), and were later shown to be important for both mitotic and meiotic recombination, as well as DSB repair following exposure of cells to genotoxic agents (Petes et al., 1991; Paques and Haber, 1999). Yeast *rad51* null muants are viable but sensitive to ionizing radiation (Symington, 2002). In contrast, vertebrate *RAD51* knock-outs are embryonic lethal (Lim and Hasty, 1996; Tsuzuki et al., 1996). *RAD51*$^{-/-}$ mouse ES cells are sensitive to IR (Stark et al., 2002), a conditional *RAD51*$^{-/-}$ chicken cell line is sensitive to treatment with either IR or mitomycin C which results in accumulation of

chromosomal breaks and ultimately cell death (Morrison et al., 1999), and human cells treated with *RAD51*-specific siRNAs accumulate numerous DNA breaks leading to cell death (A. L. Forget, M. S. Loftus, D. A. McGrew, B. T. Bennett, and K. L. Knight, unpublished data). Additional differences between yeast and vertebrate homologs are seen also for *RAD52*. In yeast, *rad52* null mutants are highly sensitive to DNA damaging agents and show more severe defects in recombination pathways than mutations in any other *RAD52* group gene (Symington, 2002). In contrast, deletion of *RAD52* in vertebrate cells results in no increased sensitivity to DNA damaging agents, and creates only minor defects in recombination-based gene targeting (Yamaguchi-Iwai et al., 1998; Rijkers et al., 1998). However, it has been suggested that functions of Rad52 important for promoting Rad51 activities are accommodated in vertebrates by Rad51 paralogs and Brca2, for which there is no homolog in *S. cerevisiae* (see below). Functional similarities have been suggested between the yeast Rad55 and Rad57 proteins, and the 5 vertebrate Rad51 paralog proteins noted above. Deletion of *RAD55* or *RAD57* results in a cold sensitive phenotype for DNA repair, suggesting that both proteins interact or are involved in stabilizing a protein complex (Lovett and Mortimer, 1987; Hays et al., 1995; Johnson and Symington, 1995). *In vitro* studies show that Rad55 and Rad57 can exist as a stable heterodimer that assists with loading of Rad51 onto ssDNA (Sung 1997), thus serving as a mediator of Rad51 by overcoming the inhibitory effect of the single-stranded DNA binding protein, replication protein A (RPA) (Sung et al., 2003). The importance of Rad51 mediators is supported by the conservation of similar activities from bacteria, e.g. RecF, O and R (Lusetti and Cox, 2003), to vertebrates, e.g. Rad51B and Rad51C (Sigurdsson et al., 2001). The Rad54 protein is a member of the SWI/SNF family of chromatin remodeling enzymes, and genetic studies in yeast first suggested its involvement in recombinational DNA repair (Symington, 2002). In addition to its

Rad51 mediator activity (Wolner et al., 2003) studies show that it plays important roles in several steps in the Rad51 pathway including strand invasion of homologous duplex DNA, heterduplex extension, and possibly in removal of Rad51 following completion of the recombination process (Peterson and Cote, 2004).

In vertebrate cells, the Brca2 protein, originally identified by the association of mutated forms with the occurrence of familial breast cancer (Zhang et al., 1998; Rahman and Stratton, 1998), has also been shown to be an important regulator of homologous recombinational DNA repair (Sharan et al., 1997; Patel et al., 1998; Moynahan et al., 2001; Thompson and Schild, 2002; Yu et al., 2003). Brca2 interacts directly with Rad51 through its several BRC motifs, encoded by exon 11, as well as a C-terminal region that includes functional nuclear localization signals, encoded by exons 26 and 27 (Wong et al., 1997; Marmorstein et al., 1998). At the time this work began it had been proposed that Brca2 is responsible for nuclear entry of Rad51 in response to DNA damage, as well as delivery of nuclear Rad51 to the sites of DNA double-strand breaks (Davies et al., 2001; Yu et al., 2003). I will present work in Chapter VI that initiates our studies of the relationship between Rad51, Brca2 and two of the Rad51 paralog proteins, Rad51C and Xrcc3. This work strongly supports the existence of a Brca2-independent mechanism of Rad51 nuclear entry.

In response to DNA double-strand breaks Rad51 forms distinct nuclear foci that are thought to represent the site of repair (Haaf et al., 1999; Tashiro et al., 2000; Aten et al., 2004), although the work presented within this thesis calls this claim into question (Chapter V). At the site of a resected DNA double strand break, Rad51 self associates in a 5′ to 3′ direction on the ssDNA to

form a nucleoprotein filament that catalyzes invasion of a homologous duplex DNA and begins the search for homology. A detailed mechanistic description of how Rad51 performs this search, and how associated proteins, e.g. Brca2 and the Rad51 paralogs, may participate remains to be determined. However, it is known that Brca2 and each of the five Rad51 paralog proteins are required for Rad51nuclear focus formation following DNA damage, and in the absence of these proteins cells exhibit an increased sensitivity to DNA damaging agents as well as chromosomal abnormalities (Tebbs et al., 1995; Liu et al., 1998; Sonoda et al., 2001; Takata et al., 2001; Thompson and Schild, 2001; Yoshihara et al., 2004; Thacker, 2005). Suppression of the deleterious effects due to the loss of any Rad51 paralog protein can best be overcome by transfection of the specific gene and not by over expression of Rad51 or other paralog genes (French et al., 2002; Takata et al., 2001). This supports the idea that each paralog provides an important and non-redundant function that promotes Rad51 activity.

Specific protein-protein associations of the paralog proteins have been demonstrated (Schild et al., 2000) and several complexes have been identified in which the paralogs stably associate with one another, e.g. Rad51B/C/D/X2, Rad51C/Xrcc3, Rad51D/Xrcc2 and Rad51B/Rad51C (Braybrooke et al., 2000; Kurumizaka et al., 2001; Liu et al., 2002; Masson et al., 2001b; Miller et al., 2002; Sonoda et al., 2001; Wiese et al., 2002). Biochemical studies using purified paralog proteins and complexes have demonstrated various activities relevant to DNA repair, e.g. DNA binding, DNA-dependent ATPase, substrate specific strand exchange, strand-separation activities, association with a Holliday junction resolvase activity, etc. (Thacker, 2005), but an integrated model of how these functions contribute to the homologous recombination pathway *in vivo* remains to be determined. The only 2 paralog proteins shown to interact specifically with

Rad51 are Xrcc3 and Rad51C, with the affinity for Rad51C increasing in the presence of Xrcc3 (Schild et al., 2000). Additionally, Rad51C's appearance in 3 of the 4 complexes suggests that it may play an important role in regulating Rad51 paralog function as well as Rad51 activity. The Rad51C/Xrcc3 complex has been proposed to function as a stable heterodimer (Masson et al., 2001a; Henry-Mowatt et al., 2003; Liu et al., 2004a), but work in this thesis provides important evidence of an independent function for Rad51C - regulation of ubiquitin-mediated proteolysis of Rad51 (Chapter IV). While Rad51, Rad51C and Xrcc3 certainly interact, my work also suggests that this interaction is highly dynamic and transient in nature (Chapter VI). It has also been suggested that Rad51C may play a role in cytoplasmic-nuclear trafficking of associated DNA repair proteins as a non canonical, functional nuclear localization sequence has been identified (French et al., 2003). Discussion of the data in Chapter VI addresses this possibility.

When my work began the requirement for Brca2 and the Rad51 paralogs for Rad51 focus formation had been demonstrated, with focus development analyzed by employing both standard antibody directed immunofluorescence against endogenous Rad51, as well as arguably the more popular method, transfection of a Rad51–fluorescent fusion protein (Bishop et al., 1998; Yuan et al., 1999; Chen et al., 1999; Bhattacharyya et al., 2000; Tarsounas et al., 2003; Liu et al., 2002; Takata et al., 2001). Of particular interest to our work was the publication by Bishop et al. (1998) describing that formation of DNA damage-induced nuclear Rad51 foci requires the Xrcc3 protein. In this work focal development was observed for both the endogenous Rad51 protein as well as human Rad51 expressed from transiently transfected vectors. Further work from the Takeda group showed that in chicken DT40 cells knockout of any of the Rad51 paralogs limited Rad51's ability to form nuclear foci following DNA damage (Takata et al., 2001). Transfection

of a vector encoding the corresponding human or mouse paralogs restored the ability of each knock out cell line to form Rad51 foci. Given the complexity of the numerous protein-protein interactions required in vertebrate cells for proper regulation and catalysis of homologous recombination, there remained the question of how well human proteins would function in heterologous cell systems, e.g. chicken DT40 cells. In fact, Takata et al. (2001) noted the sequence homologies of chicken DT40 proteins relative to the human proteins as 71% (Rad51C), 65% (Rad51D), 69% (Xrcc2) and 55% (Xrcc3) and additionally point out that "chicken DT40 Rad51C and Xrcc3 cDNA clones lack the N-terminal portions corresponding to human amino acids 1-97 and 1-147". Therefore, while complementation of recombination defects in chicken cells using human cDNAs certainly provided important initial insights, we chose to study human Rad51 and the paralog proteins using human cell lines to eliminate concerns of possible species-specific differences in protein function.

For this pursuit, we took advantage of the newly developed RNAi technology, and our initial work is presented in Chapter II. Here, we confirmed the work of Bishop et al. (1998) by showing that formation of DNA damage-induced Rad51 foci requires the presence of Xrcc3. We also showed for the first time that the Xrcc3 protein forms foci, and that this occurs independent of Rad51 and DNA damage (Forget et al., 2004). Based on our continued studies, as well as those of other groups, we questioned whether use of a GFP-Rad51 fusion protein that becomes significantly over-expressed 12-16 hr post-transfection, would limit our ability to accurately assess protein function. Additionally, there was particular concern about how this would affect our ability to observe protein localization and possible re-distribution in response to DNA damage over an extended time course of DNA repair. Interestingly, we quickly observed a

rather deleterious side effect to the system, in that, left to it own devices the Rad51 fusion protein would form nuclear foci in the absence of DNA damage. Additionally, within 20-26 hr post-transfection we observed what we refer to as "nuclear noodles", i.e. the apparent coating of the chromatin by the fusion protein. We were in the end able to work out a rigid time course in which we could measure GFP-Rad51 function and make meaningful measurements of its cellular location before over-expression became a problem. Within the time frame in which there were no foci due to over-expression, I was able to induce focus formation by ionizing radiation, and subsequently provided confocal microscopy data for studies of several mutant Rad51 proteins. Although this work was some of my earliest work in the Knight lab, submission of this manuscript on which I am an author (A. L. Forget, M. S. Loftus, D. A. McGrew, B. T. Bennett and K. L. Knight, unpublished), was delayed by unforeseeable issues. It is currently in review.

Soon after the completion of this work my attention continued to focus on the inherent problem with the fusion proteins, expression induced focus formation. In a paper by Raderschall et al. (2002) the authors tested the hypothesis that over-expression of human Rad51 would reduce the number of double-strand breaks following DNA damage. Figure 1.1A, taken from their manuscript, shows several nuclei from rat TGR928.1-9 cells and what are described as Rad51 "higher order structures". Further, they claimed that these "structures" correlated with increased expression of the Cdk inhibitor p21 and the cessation of "DNA replication synthesis". My data using HEK293 cells transfected with pEGFP-*RAD51* construct shows the same higher order structures that result simply from over-expression of the GFP-Rad51 protein we see during the 20-30 hr period post-transfection (Fig. 1.1B). Given that over-expression leads to non-damage induced foci formation and ultimately "higher order structures", we abandoned the use of

fluorescent fusion proteins for the work described in this thesis on cellular localization of Rad51 and the Rad51 paralogs. At this point the focus of my immunofluorescence microscopy work turned to endogenous DNA repair proteins, more specifically Rad51, Rad51C and Xrcc3. From the time this work was initiated until present, there have been no published accounts of endogenous Xrcc3 and/or Rad51C immunolocalization other than the publications derived from work in this thesis.

The cellular localization of Rad51 has been and still remains a point of contention in the DNA repair field. A major effort of my work has been to present controlled and verifiable immunofluorescent data for Rad51 and the paralogs Rad51C and Xrcc3. In the published literature, while it is clear that Rad51 forms nuclear foci in response to DNA damage, staining of Rad51 also showed varying amounts of cytoplasmic protein (Bishop et al., 1998; Yuan et al., 1999; Morrison et al., 1999; Bhattacharyya et al., 2000; Tashiro et al., 2000; Canitrot et al., 2004; Hauptner et al., 2004; Li and Maizels, 1997; Hussain et al., 2003; Yuan et al., 2003; Tarsounas et al., 2003; Liu et al., 2002; Pichierri et al., 2002; O'Regan et al., 2001; Essers et al., 2002; van Veelen et al., 2005; Lesca et al., 2005; Liu and Lim, 2005), yet report of the cytoplasmic localization was avoided in every manuscript. Understandably, the focus of many researchers within the field remains on the nuclear function of DNA repair proteins and the cytoplasmic dynamics may not be of interest, but should it be ignored? While many publications simply choose not to report the cytoplasmic staining that is obvious, it is also apparent that some

**FIGURE 1.1A/B**

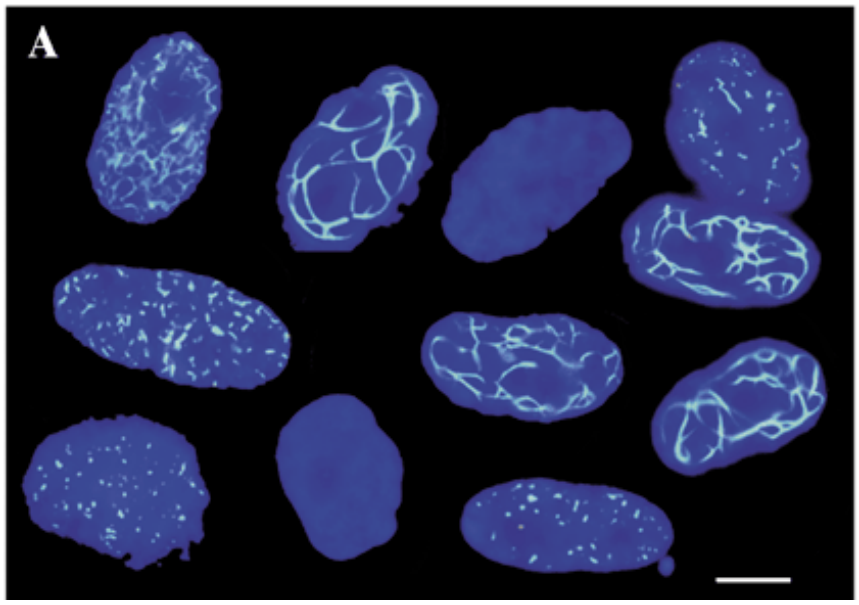


**Higher -order nuclear structure of HsRad51. Overexpressed in the TGR928.1 -9 cell line.**

**Raderschall et al., 2002**

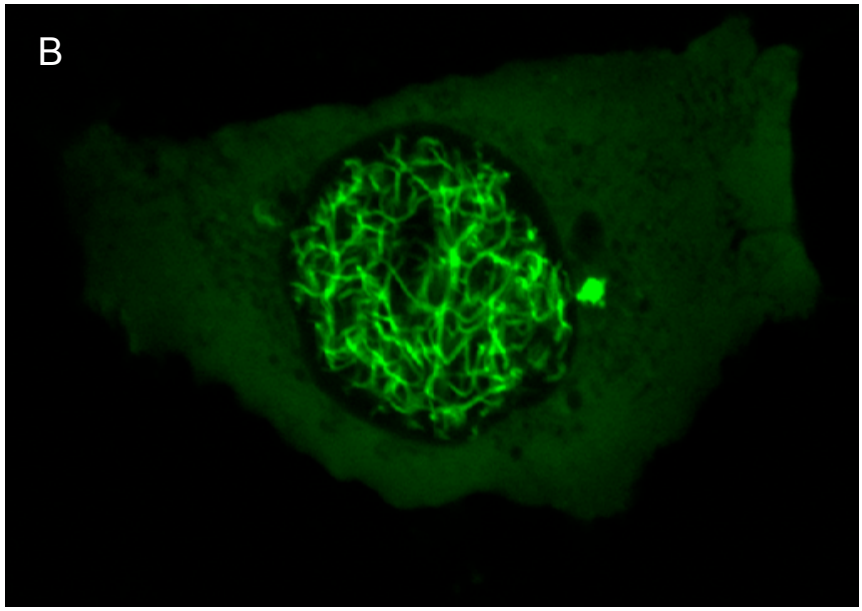


**Higher -order nuclear structure of HsRad51. Overexpressed in the HEK293 cell line.**

**Bennett, B.T. (unpublished)**

**Figure 1.1 – Rad51 Higher Order Structure. A.** Over-expression of human Rad51 in a stably transfected rat fibroblast cell line, TGR928.1-9. Rad51 was immunostained using a rabbit anti-Rad51 antibody and a FITC-conjugated secondary antibody (from Raderschall et al., 2002). **B.** HEK293 cells transfected with a *GFP-RAD51* vector. Cells were imaged 24 hr post-transfection using a Leica confocal TCS DMIRE2 SP2 microscope. Cells were not exposed to DNA damage.

manuscripts are formatted in such a way as to avoid the cytoplasm all together, in that images are reduced to the display of a single nucleus (Dong et al., 1999; Hussain et al., 2004; Ivanov et al., 2003; Kao et al., 2003; Paull et al., 2000; Wu et al., 2003) and in fact, many of the afore cited articles show partial nuclei. To further the ambiguity in the literature, there are manuscripts in which an image will show exclusively nuclear Rad51 in one figure, and then in another show that it is also in the cytoplasm (Maser et al., 1997; Tarsounas et al., 2003). Over the course of my thesis work and from discussions with students and post-docs at various meetings, I have also come to understand that many images in the literature showing exclusive nuclear localization of DNA repair proteins more than likely represent post processing manipulations of the image. Surprisingly, the vast majority of manuscripts showing immunofluorescence images of Rad51 do not list the editing program and/or the changes made to the image. Also, while many publications do not show cytoplasmic Rad51, interestingly, several papers demonstrate by Western blot the existence of significant amounts of cytoplasmic Rad51 (Yoshikawa et al., 2000; Davies et al., 2001; Essers et al., 2002; Liu and Lim, 2005). Our work clearly demonstrates significant amounts of cytoplasmic Rad51 in human cells using both immunofluoescence and cell fractionation procedures (Chapters II, IV and V), and studies continuing from those presented in this thesis are designed to address important issues regarding the trafficking of cytoplasmic Rad51 and associated proteins in response to DNA damage.

In a field that now relies so heavily on immunofluorescence imaging as a means to assess the dynamics of protein movement and protein-protein interactions in response to DNA damage, more specific descriptions of the methodology used to acquire the data should be demanded, i.e.,

antibodies used and validation of their specificity, the method of antibody application (see below and Chapter V), specific details regarding the microscope used and all settings, as well as specific mention of any post image processing that was done. For example, in many cases primary antibodies are noted as being a "gift" from a colleague and no verification of specificity is provided. Another concern is that claims of protein co-localization are frequently made without considering potential cross-over of fluorophore signals. Using human fibroblast cell lines Bischof et al. (2001) showed cell cycle-dependent and DNA damage-dependent co-localization of several protein pairs including Rad51/promyelocytic leukemia protein (PML), Rad51/Bloom syndrome helicase (BLM), RPA/BLM and PML/BLM. In each case primary antibodies were imaged using fluorescein isothiocyanate (FITC) or Texas Red secondary antibody conjugates and the authors mention that foci were scored using either epifluorescent and/or single photon laser confocal microscopy. However, there is no description of exactly how the 100 nm cross-excitation and emission of these two fluors was dealt with, nor was it stated what images were collected using which microscope. The possibility of fluor cross-over could result in some degree of apparent co-localization, in addition to the fact that scoring foci in wide field images introduces the risk that the total sample fluorescence of the entire depth of the cell will also contribute to the false impression of co-localization. Finally, in this paper it is stated that cells were stained using antibody cocktails, a practice we have found to be commonly used in immunofluorescence studies. However, my data in Chapter V clearly demonstrates that use of antibody mixes can lead to artifactual appearance of protein co-localization. As another example, the paper by Paull et al. (2000), which was largely responsible for establishing the dogma that Rad51 co-localizes with the histone marker for DNA double strand breaks, gamma H2AX, appears fraught with methodological problems, or at least ambiguities. Various primary

antibodies for 5 proteins, gamma H2AX, Rad50, Rad51, Nbs1 and Brca1, are listed but in no case is evidence shown or cited to support their specificity. Additionally, secondary antibodies in all cases were FITC and Alexa 546 conjugates, and while excitation with the He-Ne laser will induce Alexa 546-specific emission, excitation with the argon laser (as described in their Methods section) will excite both fluors. Therefore, a specific description of how the microscopes were used is necessary to assure the reader that co-localization is not the result of cross-excitation. Also, the methods description implies that antibody cocktails were used in all cases where protein co-localization was examined. Again, in Chapter V, I address the fact that this antibody application method can create artifactual co-localization, especially for human Rad51 and gamma H2AX.

Upon the inception of the work presented here and review of the homologous recombinational DNA repair literature, my specific goals were to provide functional and cellular information for Rad51 paralog proteins, and to address the general methodological problems regarding immunofluorescence studies of DNA repair proteins that were evident in the literature, some of which are described above. Given our early realization of the limitations imposed by use of the popular fluorescent fusion proteins, an important part of this work was to study endogenous proteins in human cells.

## PREFACE TO CHAPTER II

The work in Chapter II describes the first successful attempt to visualize an endogenous Rad51 paralog protein, Xrcc3. Published data using CHO and chicken DT40 cells demonstrated that Xrcc3 was required for formation of DNA damage-induced nuclear Rad51 foci. Ours was the first study to show this in a human cell line. This work reveals a distinct cellular localization for Xrcc3 both before and in response to DNA damage.

The system described herein was designed to assay both Rad51 and Xrcc3 with as little disruption to the cellular environment as possible. We imaged only endogenous protein, thus eliminating the artifactual localization patterns we had seen using transfected vectors. Additionally, depletion of Rad51 and Xrcc3 was accomplished using RNAi methods eliminating the need for the creation of null cell lines. The use of RNAi was also important as the loss of Rad51 is lethal, whereas cell health and relevant cell responses to DNA damage were maintained over the 1-3 day course of Rad51 depletion.

My specific contributions to this work were the development of the immunofluorescent methods. Hypothesis development, experimental design, and interpretation of the data were shared between myself and Anthony Forget, while design and implementation of the RNAi technology was the work of Anthony Forget.

# CHAPTER II

# XRCC3 IS RECRUITED TO DNA DOUBLE STRANDED BREAKS EARLY AND INDEPENDENT OF RAD51


## Abstract

Rad51-mediated homologous recombination is essential for the maintenance of genome integrity. The Xrcc3 protein functions in homologous recombination DNA repair and studies suggest it has multiple roles at different stages in this pathway. Defects in vertebrate Xrcc3 result in elevated levels of spontaneous and DNA damage-induced chromosomal abnormalities, as well as increased sensitivity to DNA damaging agents. Formation of DNA damaged-induced nuclear Rad51 foci requires Xrcc3 and the other Rad51 paralog proteins (Rad51B, Rad51C, Rad51D, and Xrcc2), thus supporting a model in which an early function of Xrcc3 involves promoting assembly of active Rad51 repair complexes. However, it is not known whether their stable association with breaks requires Rad51. Here we report for the first time that Xrcc3 forms distinct foci in human cells and that nuclear Xrcc3 begins to localize at sites of DNA damage within 10 minutes after radiation treatment. RNAi-mediated knock down of Rad51 has no effect on the DNA damage-induced localization of Xrcc3 to DNA breaks. Our data are consistent with a model in which Xrcc3 associates directly with DNA breaks independent of Rad51, and subsequently facilitates formation of Rad51 nucleoprotein filament.

## Introduction

Homologous recombination is an important pathway in mammalian cells for the repair of DNA double-strand breaks that result from exposure to exogenous DNA damaging agents as well as during normal metabolic processes such as DNA replication and meiotic chromosomal alignment (Pierce et al., 1999; Thompson and Schild, 2001). HR is essential for the maintenance of genome integrity, as defects in this pathway have been shown to result in chromosomal abnormalities that correlate with a number of cancers (Thompson and Schild, 2002). In this pathway, the ends of double-strand breaks are processed by endonucleases to produce a ssDNA tail onto which the Rad51 recombinase is loaded to form a nucleoprotein filament. Rad51 provides the central activity of homologous recombination by catalyzing strand exchange between the damaged DNA and an undamaged homologous chromosome, most frequently a sister chromatid, resulting in the formation of cross-over structures referred to as Holliday junctions (Sung et al., 2003; West, 2003). Genetic evidence demonstrates that successful initiation and completion of homologous recombination depends on the function of a group of structurally related proteins referred to as Rad51 paralogs; Rad51B, Rad51C, Rad51D, Xrcc2, and Xrcc3 (Tebbs et al., 1995; Liu et al., 1998; Takata et al., 2001; Thompson and Schild, 2001; Yoshihara et al., 2004). For example, knock-out of each of the paralog genes in chicken DT40 cells resulted in increased sensitivity to DNA damaging agents and elevated levels of chromosomal abnormalities (Takata et al., 2001). Specific protein-protein interactions between Rad51 paralog proteins have been demonstrated (Schild et al., 2000) and several complexes have been identified (Kurumizaka et al., 2001; Masson et al., 2001b; Sigurdsson et al., 2001; Kagawa et al., 2002; Wiese et al., 2002).

Recent studies of Xrcc3 suggest that it has a remarkably diverse set of functions and acts both early and late in the homologous recombination pathway. Xrcc3 has been shown to play an

active role in DNA damage-induced replication fork slowing, a function that occurs early in the homologous recombination pathway (Henry-Mowatt et al., 2003). Defects in fork slowing in both hamster and chicken *XRCC3*$^{-/-}$ cells were corrected by either introduction of a human *XRCC3* cDNA or by inclusion of purified human Rad51C-Xrcc3 complex in a permeabilized cell replication assay (Henry-Mowatt et al., 2003). Several lines of work also suggest that Xrcc3 functions during the late stages of homologous recombination. For example, defective processing of recombination intermediates is observed in both hamster and *Arabidopsis XRCC3*$^{-/-}$ cells (Bleuyard and White, 2004; Lio et al., 2004), and recent studies suggest that human Xrcc3 plays a direct role in Holliday junction resolution (Liu et al., 2004a).

Another early function for Xrcc3 likely involves recruitment of Rad51 to the sites of double-strand breaks. Many proteins directly involved in the catalysis of homologous recombination appear in distinct nuclear structures termed foci (Haaf et al., 1995; Li and Maizels, 1997; Essers et al., 2002) and their accumulation at sites of DNA damage suggests that these are active centers of DNA repair (Haaf et al., 1999; Tashiro et al., 2000; Aten et al., 2004). To date, only Rad51 has been studied regarding the requirement of other factors for its appearance within DNA damaged-induced foci. For example, in hamster, chicken, and human cell lines, formation of damage-induced nuclear Rad51 foci requires Xrcc3 (Bishop et al., 1998; Takata et al., 2001; Yoshihara et al., 2004). Studies using a chicken cell line show that formation of Rad51 foci also requires the other Rad51 paralog proteins (Takata et al., 2001). Despite their requirement at this early step in the homologous recombination pathway, it has not been determined whether any of the five Rad51 paralog proteins accumulate at the site of a DNA break. In the present study, using a combination of immunostaining, transient expression of fluorescent fusion proteins and

RNA interference, we show that Xrcc3 forms discrete nuclear foci that localize to double-strand breaks, and that this occurs independent of Rad51.

## Results

### Formation of Xrcc3 Foci Is Independent of Rad51

Immunostaining of HEK293 cells shows the presence of Rad51 in both the cytoplasm and nucleus (Fig. 2.1A-C), consistent with previous results (Yoshikawa et al., 2000). Exposure to ionizing radiation (10 Gy) results in an increase in both the number and size of nuclear Rad51 foci (Fig. 2.1, compare panels B and E). At the 1 h time point shown in Figure 2.1 some of the nuclear Rad51 has begun to co-localize with gamma H2AX (Fig. 2.1D-F), a phosphorylated histone variant (H2AX) that serves as a marker for sites of DSBs (Rogakou et al., 1998). Our data in Figure 2.1 also reveal for the first time the presence of Xrcc3 foci. We find that discrete, small Xrcc3 foci are present in both the cytoplasm and nucleus in the absence of DNA damage (Fig. 2.1M-O). Similar to Rad51, following exposure to ionizing radiation nuclear Xrcc3 foci are larger, greater in number, and begin to localize to DNA break sites within 1 h (Fig. 2.1P-R). Therefore, it appears that exposure to ionizing radiation results in the redistribution of nuclear Xrcc3 to sites of DNA damage, and that Rad51 and Xrcc3 accumulate at the sites of DNA breaks.

**FIGURE 2.1**

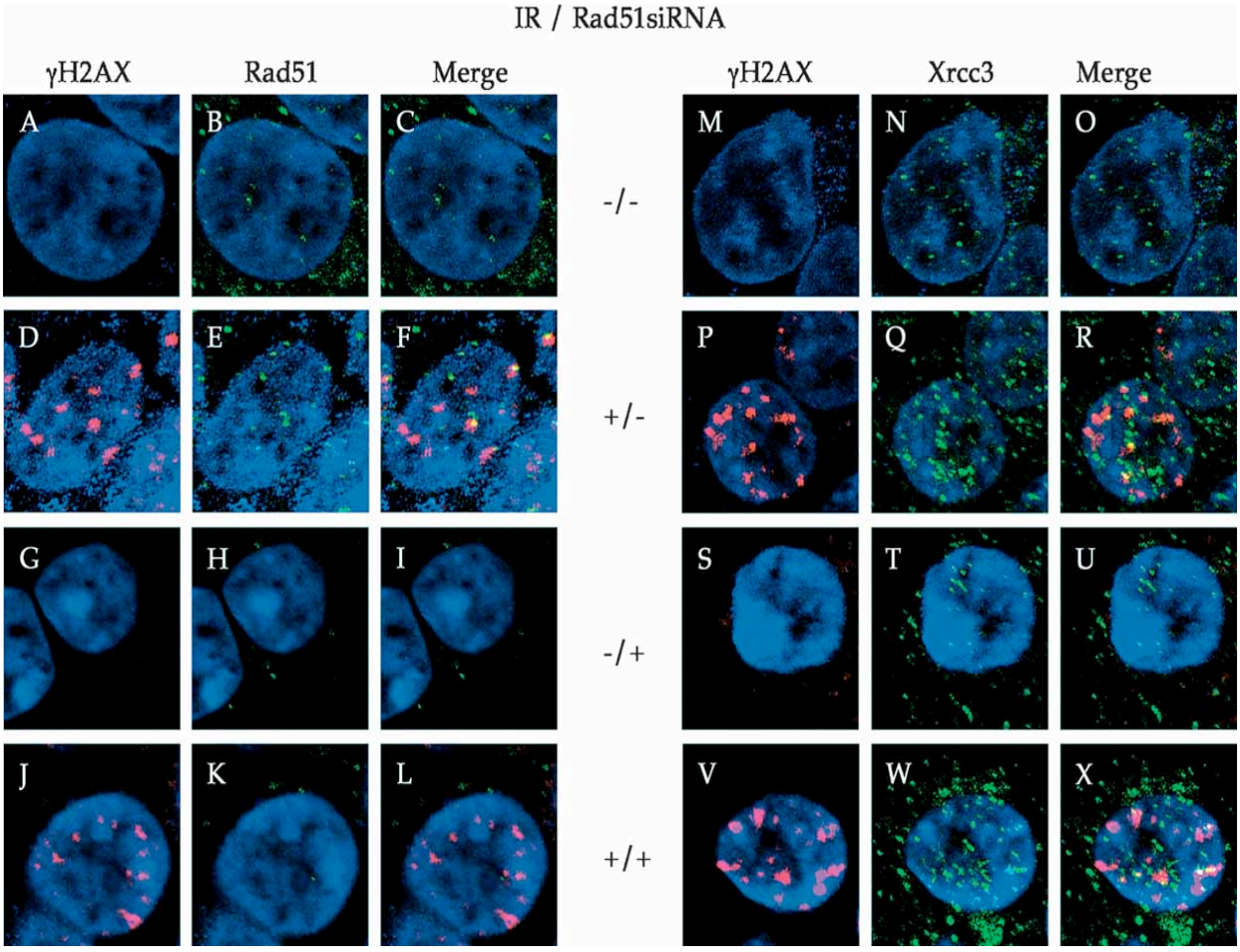
IR / Rad51siRNA
γH2AX
Rad51
Merge
γH2AX
Xrcc3
Merge
A
B
C
M
N
O
-/-
D
E
F
P
Q
R
+/-
G
H
I
S
T
U
-/+
J
K
L
V
W
X
+/+

**Figure 2.1 - Localization of Xrcc3 to DNA double strand breaks does not require Rad51.** HEK293 cells were immunostained for gamma H2AX (red) and either Rad51 (green) or Xrcc3 (green). Nuclei are stained with DAPI (blue). Where indicated, cells were exposed to 10 Gy ionizing radiation (IR+), and were fixed 60 min after exposure. Cells treated with Rad51-specific siRNA (Rad51 siRNA+) were transfected 16 h prior to IR exposure. Cells in each panel are typical of >90% of the total observed in a minimum of three independent experiments.

Previous studies have shown that Xrcc3 is required for formation of Rad51 nuclear foci upon DNA damage (Bishop et al., 1998; Takata et al., 2001; Yoshihara et al., 2004). Our results above provide the first evidence that this function of Xrcc3 is likely to occur directly at the site of the DNA break. This, together with the fact that Xrcc3 interacts directly with Rad51 (Schild et al., 2000), raises the question of whether stable association of Xrcc3 with DNA break sites requires the presence of Rad51. Therefore, we asked whether the DNA damage-induced localization of Xrcc3 to the sites of DSBs is dependent on Rad51. HEK293 cells transfected with a Rad51-specific siRNA showed a significant reduction in the amount of Rad51 prior to treatment of cells with ionizing radiation (Fig. 2.1G-I) and eliminated greater than 90% of the damage-induced nuclear Rad51 foci (Fig. 2.1J-L). However, treatment of cells with Rad51 siRNA had no visible effect on the Xrcc3 staining pattern either before or after DNA damage. Xrcc3 still formed small pre-damage foci in both the cytoplasm and nucleus (Fig. 2.1S-U). Following treatment with ionizing radiation, nuclear Xrcc3 foci increased in both number and size, and showed a partial localization to double-strand breaks similar to that seen in the presence of Rad51 (Fig. 2.1V-X). As expected, treatment of cells with Rad51-specific siRNA prohibited resolution of double-strand breaks and resulted in cell death (data not shown).

The specificity of Rad51 siRNA was confirmed using a RAD51-GFP transgene carrying a silent mutations (RAD51SM-GFP) rendering it immune to the actions of the siRNA.

**FIGURE 2.2**

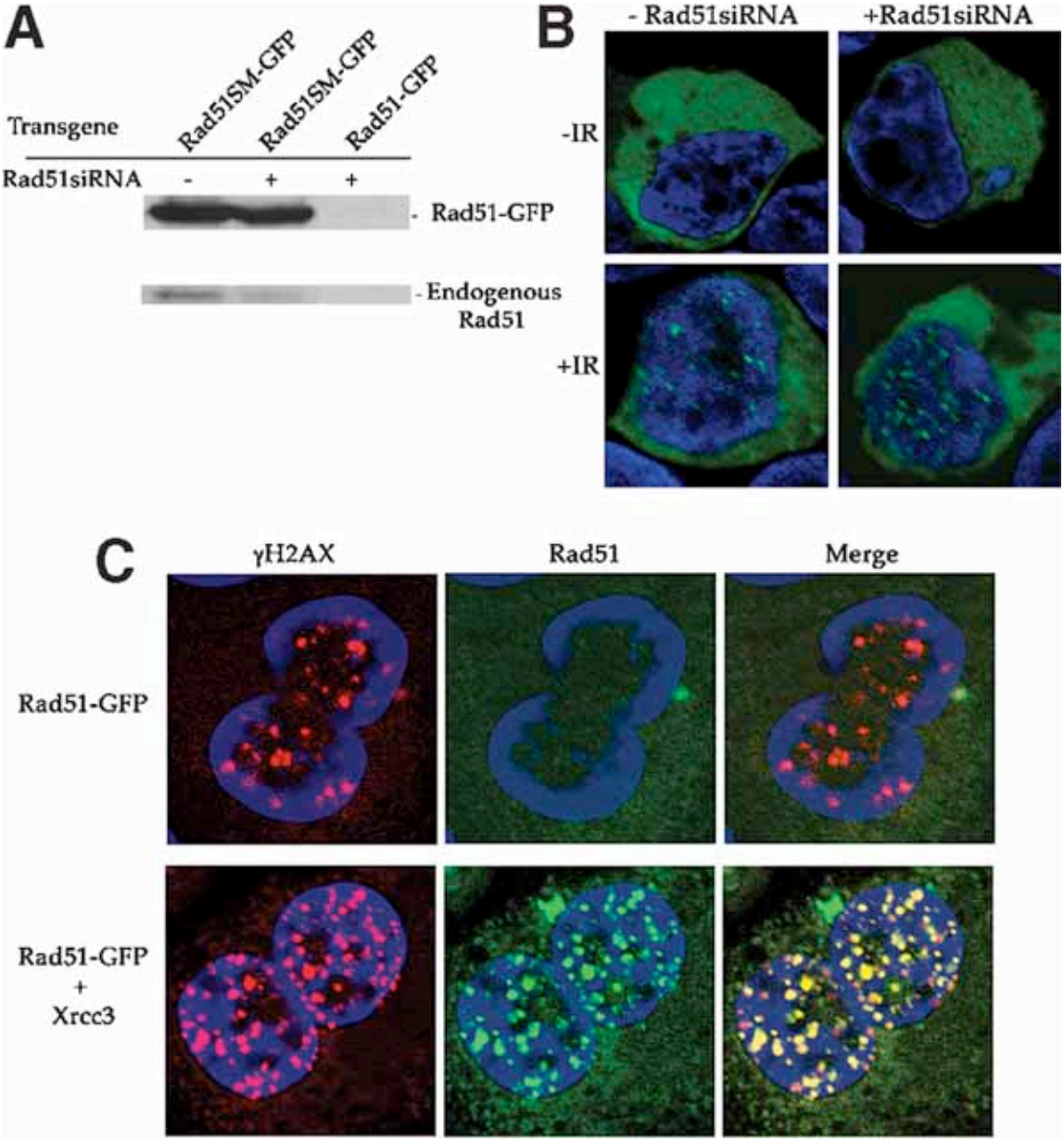
A
Transgene
Rad51SM-GFP
Rad51SM-GFP
Rad51-GFP
Rad51siRNA - + +
Rad51-GFP
Endogenous Rad51
B
- Rad51siRNA
+Rad51siRNA
-IR
+IR
C
γH2AX
Rad51
Merge
Rad51-GFP
Rad51-GFP + Xrcc3

**Figure 2.2 – RNAi-mediated knock-down of Rad51-GFP fusion protein**.

**A:** Western blot showing expression of both endogenous Rad51 and the Rad51SM-GFP protein (lane1), specific RNAi-mediated knock-down of endogenous Rad51 but not the fusion protein carrying silent mutations in the targeted region of the Rad51 sequence, Rad51SM-GFP (lane 2) and RNAi knock-down of both endogenous Rad51 and a Rad51-GFP fusion expressed from a wild type Rad51-GFP gene (lane 3). **B:** HEK293 cells transfected with a plasmid carrying the RAD51SM-GFP transgene were co-transfected with a Rad51-specific siRNA duplex and treated with 10Gy ionizing radiation as indicated. Cells exposed to radiation were incubated for 60 minutes before fixation. **C**: XRCC3-/- Chinese hamster ovary cells (irs1SF) were transfected with a plasmid carrying the RAD51SM-GFP transgene or co-transfected with this plasmid and another carrying the wild type HsXRCC3 gene. Cells were exposed to 10 Gy ionizing radiation and grown for 60 minutes before fixation.

Western blot analysis shows that cotransfection of the siRNA and Rad51SM- GFP depletes the cells of ≥ 90% of the endogenous Rad51 while expression of Rad51SM-GFP is maintained (Fig. 2.2A). The absence of Rad51 foci in siRNA treated HEK293 cells was rescued by cotransfection with RAD51SM-GFP which forms DNA damage-induced nuclear foci similar to those seen with the endogenous protein (Figs. 2.2B and 2.1J–L). We confirmed the functional relevance of the Rad51SM-GFP protein in the early stages of homologous recombination by recapitulating previous results using the Xrcc3-deficient irs1SF hamster cell line (Bishop et al., 1998). Expression of Rad51SM-GFP in irs1SF cells resulted in formation of no damage-induced Rad51 foci (Fig. 2.2C). However, co-expression with HsXRCC3 cDNA resulted in recovery of Rad51 focus formation following exposure to ionizing radiation (Fig. 2.2C). The fact that Xrcc3 localizes to double-strand breaks independent of Rad51 prompted us to look into the timing of DNA damage-induced Xrcc3 and Rad51 focus formation.

**Rad51 and Xrcc3 localize to the sites of DNA breaks within 10 minutes following Exposure to Ionizing Irradiation.**

If Xrcc3 is required for damage-induced Rad51 focus formation, but not the converse, then Xrcc3 may be localized to the site of a double-strand break prior to Rad51 in order to facilitate recruitment of Rad51. To observe the timing of Rad51 and Xrcc3 focus formation, HEK293 cells were fixed at 10, 30, and 60 min following exposure to 10Gy IR, and immunostained for endogenous Rad51 and Xrcc3. We find that both Xrcc3 and Rad51 nuclear foci begin to appear within 10 min after treatment with IR, and these foci

**FIGURE 2.3**

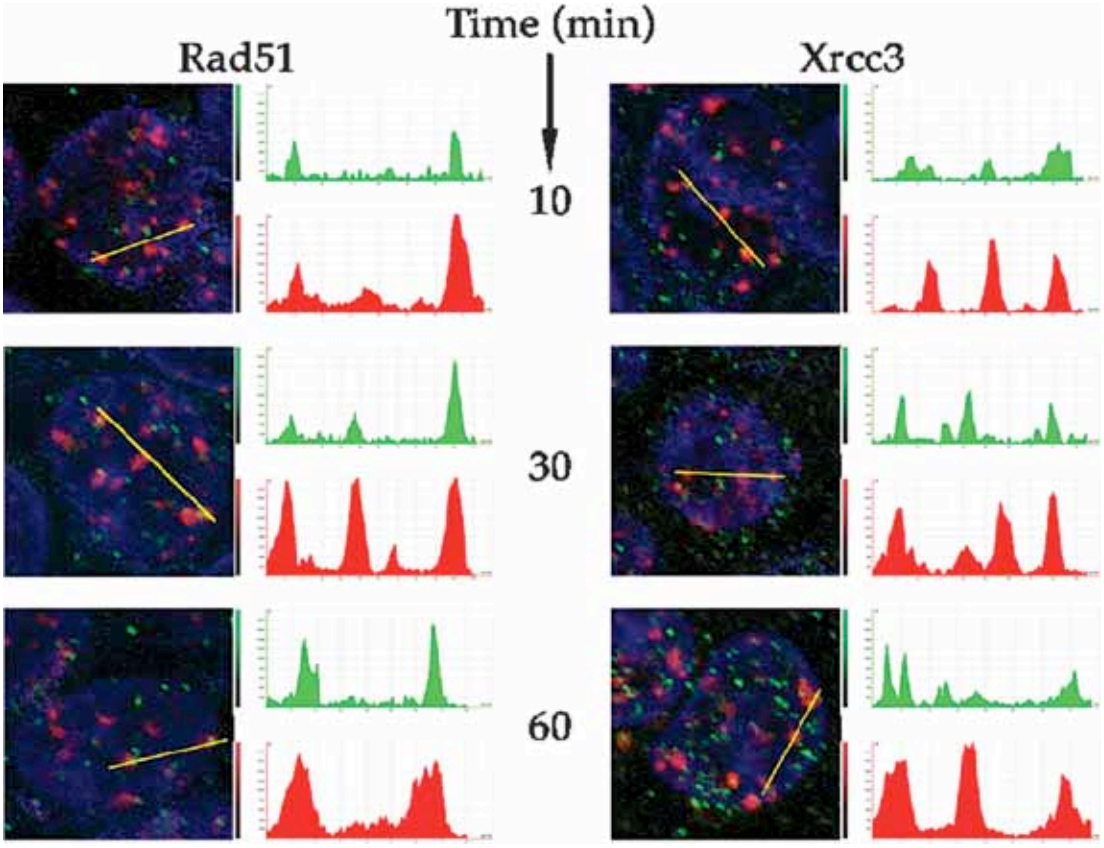

**Figure 2.3 – Rad51 and Xrcc3 localize to DNA double strand breaks within 10 minutes following exposure to IR.**

HEK293 cells were fixed 10, 30, and 60 minutes following exposure to 10 Gy ionizing radiation. Cells were immunostained for gamma H2AX (red) and Rad51 (green) in the left three panels and for gamma H2AX (red) and Xrcc3 (green) in the right three panels. Profiles at the right of each image indicate the fluorescence intensity of the green and red channels (measured independently) along the yellow line in the corresponding image.

show a partial colocalization with double-strand breaks as indicated by gamma H2AX foci (Fig. 2.3). The incidence of colocalization for several gamma H2AX foci (red) and either Rad51 or Xrcc3 foci (green) is displayed in the profiles to the right of each image in Figure 2.3. The fluorescence intensity (y-axis) is plotted against the position of the focus along the yellow line in the image (x-axis). The only other report of Rad51 focus formation at early times after damage (<60 min) noted that approximately 1% of human fibroblast cells (line Hs68) showed DNA damage-induced nuclear Rad51 foci 10 min after exposure to 9 Gy ionizing irradiation (Haaf et al., 1995). However, we find that over 80% of HEK293 cells show an increase in nuclear Rad51 foci 10 min after exposure to 10 Gy ionizing irradiation. The importance of our results lies in the fact that we observe a partial colocalization of these foci specifically to the site of DNA breaks and that both Rad51 and Xrcc3 begin to associate with breaks as early as 10 min post DNA damage. Under the conditions used we cannot determine whether both Rad51 and Xrcc3 are associated together at any particular gamma H2AX focus, but this method is currently under development.

## Discussion

The data presented here provide new insights into a developing model regarding the dynamics of recombinational repair proteins (Essers et al., 2002; Yu et al., 2003; Aten et al., 2004) and the function of Rad51 paralogs. We provide the first demonstration of DNA damage-inducible redistribution of Xrcc3 within the cell and formation of Xrcc3 nuclear foci that localize to the sites of double-strand breaks. Additionally; we show that both Xrcc3 and Rad51 appear at the sites of breaks within 10 min following exposure to ionizing radiation. Importantly, we demonstrate that formation of DNA break associated nuclear Xrcc3 foci occurs independent of

Rad51. Within the context of other studies regarding the function of Rad51 paralog proteins and the dynamics of recombinational repair proteins following DNA damage, our data supports the following model (Fig. 2.4) for the action of Xrcc3 early in the homologous recombination pathway. The fact that formation of DNA damage induced Rad51 nuclear foci requires the presence of Xrcc3 (Bishop et al., 1998; Takata et al., 2001; Yoshihara et al., 2004), and that we now show Xrcc3 beginning to localize with DNA breaks within 10 min following exposure to DNA damage, strongly suggests that Xrcc3 acts specifically at the site of a DNA break to assist in the formation of Rad51 foci, most likely by promoting assembly of the Rad51 nucleoprotein filament. Yu et al. (2003) recently reported that approximately 20% of nuclear Rad51 is sequestered in an immobile complex by virtue of its association with BRCA2, and that it is this pool of Rad51 that is selectively mobilized following replication arrest. However, this mobilization is preceded by a 60–75 min delay. We find that DNA break-associated Rad51 foci form within the first 10 min following DNA damage, suggesting that the Rad51 in these early foci is derived from a pool other than that associated with BRCA2, perhaps either the fraction that is immobile due to Rad51 self-association or the approximate 60% of Rad51 that constitutes the mobile fraction (Yu et al., 2003). Because Xrcc3 forms nuclear foci at the sites of breaks independent of Rad51 we propose that specific protein–protein interactions between Xrcc3 and Rad51 at the DNA break site are directly involved in formation of a Rad51 nucleoprotein filament. This function of Xrcc3 would not necessarily require that it arrives earlier than Rad51 at a DNA break site. We find that both proteins are associated with DNA breaks within 10 min after ionizing radiation treatment, but earlier measurements will be needed to provide more detail about the kinetics of the association of repair proteins with DNA breaks. Whether the BRCA2-associated Rad51 is delivered directly to the site of damage, or upon damage BRCA2 releases

bound Rad51 into the mobile pool, specific association of Rad51 with Xrcc3 would again promote assembly of Rad51 into nucleoprotein filaments. Although we currently have no information on the cellular localization of Rad51C either before or after DNA damage, we have included Rad51C in the model (Fig. 2.4) because Xrcc3 forms a specific heterodimeric complex with this protein (Masson et al., 2001a; Wiese et al., 2002). The Rad51C/Xrcc3 dimer associates with single-stranded but not double stranded DNA (Masson et al., 2001b), and therefore may be able to rapidly associate with the single-stranded regions that appear early at a break. Recent data shows that the stability of the Rad51C/Xrcc3 dimer is regulated by ATP binding and hydrolysis by Xrcc3 (Yamada et al., 2004). Given that Rad51 and each of the five Rad51 paralog proteins has an ATP binding site, regulation of the variety of protein–protein interactions required for the establishment of active repair complexes early in the homologous recombination pathway may be mediated by specific ATP binding and turnover events. In fact, recent studies by Shim et al. (2004) suggest that Xrcc2 acts as an NTP exchange factor by stimulating ATP processing by Rad51 in a Rad51D-dependent manner. We consistently find a larger number of Xrcc3 foci relative to Rad51 foci in the nucleus as well as the cytoplasm both before and after exposure to DNA damage. Although we currently do not understand the relationship between these differences in number and localization, further studies are designed to address this issue. While much remains to be discovered about the dynamics and function of recombinational repair proteins, work in this study provides important new information about the DNA damage-induced redistribution and site of action of the Xrcc3 protein early in the homologous recombinational DNA repair pathway.

**FIGURE 2.4**

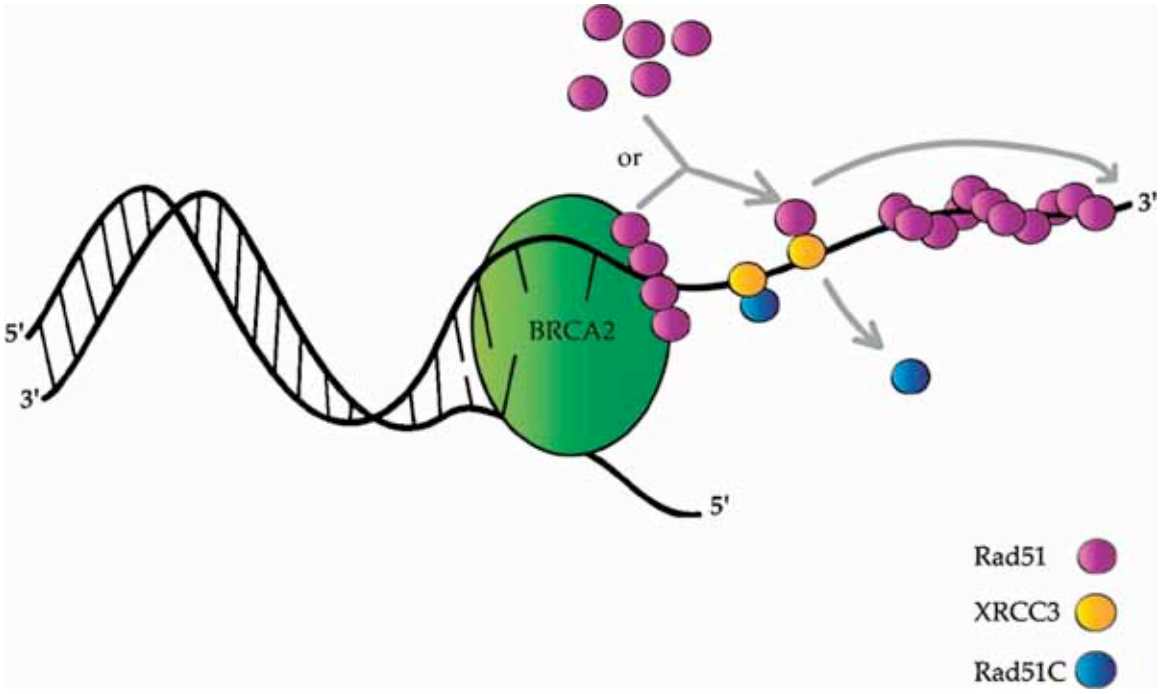

**Figure 2.4 - Model for an early function of Xrcc3 in the homologous recombination pathway.**

Given that our data shows Xrcc3 focus formation at the site of a DNA break 10 min after exposure to ionizing radiation, it is likely that at least one function of Xrcc3 occurs directly at the site of the break. The Rad51C/Xrcc3 heterodimer binds single strand DNA (Masson et al., 2001a) at the break and through direct interactions between Xrcc3 and Rad51, mediates the formation of the Rad51 nucleoprotein filament. Rad51 that forms foci within 10 min after DNA damage is likely derived from a mobile pool of Rad51 (Yu et al., 2003) whereas BRCA2-bound Rad51 (Yu et al., 2003) may contribute to formation of Rad51 foci at later times.

## Methods and Materials

***Cell lines and Transfections*** **-** HEK293 cells were obtained from ATCC and were maintained in DMEM supplemented with 10% fetal bovine serum (FBS) and 1% Pen/Strep. In preparation for transfection, cells were maintained in DMEM plus 10% FBS. Chinese hamster ovarian (CHO) irs1SF cells (XRCC3-/-) were maintained in DMEM supplemented with 10% FBS, 1% Pen/Strep, and 1% non-essential amino acids. The RAD51-GFP plasmid was made by inserting the HsRAD51 gene into the SalI-AgeI sites in the multicloning site of pEGFP-N1 (Clontech, Palo Alto, CA). The RAD51SM-GFP (SM = silent mutations) was made by introducing several silent base changes in the siRNA targeted region of the wild type RAD51 sequence. Transfection of both a Rad51- specific siRNA duplex (Qiagen, Studio City, CA) and plasmids was performed using a lipid transfection method (Lipofectamine 2000, Invitrogen, San Diego, CA). A control siRNA against lamin A/C and a 30-fluorescein labeled control siRNA with no matches in human genome(Qiagen, cat# 1022079) showed no effect on Rad51 or Xrcc3 focus formation, or protein levels as determined by Western blots, when transfected into HEK293 cells (data not shown). When used together the siRNA and plasmid were co-transfected.

***Antibodies*** **-** Primary antibodies used for immunofluorescence staining were mouse anti-phospho-histone H2AX biotin conjugate (clone JBW301, Upstate Biotechnology, Lake Placid, NY), mouse anti-Rad51 (clone3C10,Upstate Biotechnology), mouse anti-Xrcc3 (10F1/6, Novus Biologicals, Inc., Littleton, CO) and all were diluted 1:500. Alexa 488 and Alexa 555 (Molecular Probes, Eugene, OR), and Immunopure Streptavidin Rhodamine Conjugate (Pierce, Rockford,

IL) secondary antibodies were diluted 1:1,000. All dilutions were in PBS containing 1% BSA. DNA was counterstained with Vectashield Fluorescent Mounting Media containing DAPI (40, 60-diamidino-2- phenylindole; Vector Laboratories, Burlingame, CA).

***Immunostaining and Confocal Microscopy –*** Cells were grown on coverslips in a 6 well dish. For fixation, media was aspirated off and cells were washed once with PBS and immersed in 100% methanol at -20˚C for 5 min. Cells were blocked in PBS containing 4% BSA overnight at 4˚C. After blocking, cells were washed five times for 5 min each with PBS. Incubation with both primary and secondary antibodies was performed in 6 well dishes for 1 h at 37˚C in a humid environment using a slide warmer (Fisher, Medford, MA). Cells were washed five times for 5 min each in PBS after incubation with both primary and secondary antibodies. Coverslips were mounted using Vectashield with DAPI and sealed with polyurethane (nail polish) then stored in the dark at 4˚C. Visualization of immunostains was performed by confocal microscopy using a Leica TCS SP2 AOBS instrument and image processing was performed using the accompanying Leica Confocal Software TCS SP2.

***Damage-Induced DNA Double Strand Breaks -*** Cells were exposed to 10 Gy ionizing radiation (IR) (137Cs) using a Gammacell 40 (MDS Nordion Ottawa, Ont., Canada). After exposure, cells were allowed to recover at 37˚C (5% CO2) for the indicated times. Cells were then methanol fixed and prepared for immunostaining.

***Western Blotting -*** HEK293 cells were transfected with the appropriate transgene and/or siRNA as indicated (Fig. 2.2A). Cells were harvested 20 h post transfection washed with PBS and lysed

with RIPA buffer (25 mM Tris pH 7.4, 0.5% triton X-100, 0.5% sodium deoxycholate, 0.05% sodium dodecyl sulfate, 0.05 mM EDTA pH 7.0, 75 mM NaCl) and total protein was determined with BCA Protein Assay Kit (Pierce). Acrylamide mini-gels (10%) were run with 80 mg of total protein in each lane and transferred to PVDF membranes overnight at 200 mV in transfer buffer (192 mM glycine, 25 mM Tris, 20% methanol). Membranes were incubated in blocking buffer (10 mM Tris-HCl pH 8.0, 300 mM NaCl, 0.025% Tween 20) containing 15% instant nonfat dry milk for 45 min. Rad51 primary antibodies (Oncogene #PC130) were added (1:3,000) in blocking buffer containing 2% instant nonfat dry milk for 1 h and membranes were washed five times for 5 min each in blocking buffer. Peroxidase conjugated antirabbit secondary antibodies (Pierce #31462) were added (1:12,000) for 1 h and membranes washed as above. Membranes were incubated with LumiGLO chemiluminescent substrate (KPL #54-61-01) for 1 min, exposed to X-ray film, and developed (Kodak 2000A XOMAT processor).

# CHAPTER III

# ANTIBODY PURIFICATION – OPTIMIZATION OF IMMUNO-FLUORESENCE AND ANTIBODY SPECIFICITY

## INTRODUCTION

After the publication of my first manuscript [(2004) J. Cell. Biochem. 93, 429-436], the need to improve the quality of my immunofluorescent protocol was apparent if I wished to increase my ability to quantify localization data. Further, having had some initial success with increasing the specificity of the Xrcc3 antibody used in that work, I felt that the purification of commercially available antibodies would not only help to reduce immunofluorescence background and improve the image clarity, but would also eliminate the argument that the images may represent non-specific binding and artifactual staining patterns. At that time, it was apparent that the lack of immunofluorescence data for endogenous Rad51 paralogs in human cells, other than for Rad51D (Tarsounas et al., 2004a), and reliance on the use of fluorescent fusion proteins, was in large part due to the lack of antibodies proven to be specific for these antigens, as well as a useful purification system to improve antibody quality. The result of this endeavor was successful purification of monoclonal antibodies against all of the Rad51 paralog proteins, as well as several other DNA repair proteins. In addition to reducing background and non-specific signals in both Western blot and immunofluorescence applications, purification also allowed us to demonstrate antibody specificity using RNAi methods, which surprisingly had not been previously reported. The experimental design and subsequent bench work was singularly my effort.

## RESULTS

To optimize antibody signal and specificity I set out to test a wide range of commercially available antibodies against all 5 paralog proteins from a number of suppliers. Both monoclonal and polyclonal antibodies were available and we would need to be sure our purification system works efficiently for both. Surprisingly, I found that a number of antibodies produced little to no signal by any method of detection (at this point I learned that most companies selling antibodies do not perform quality control on the products). These were eliminated from further consideration. We also found that some antibodies labeled as "purified", in fact, showed varying degrees of specificity as demonstrated by Western blot analysis. We obtained a purified monoclonal antibody against human Rad51 from Upstate, Inc. and unpurified monoclonal antibodies in the form of raw ascites fluid against Rad51B, Rad51C, Rad51D and Xrcc3 from Novus Biologicals.

Our results show that we were able to purify each antibody to a high level and in each case we demonstrated significantly improved specificity by both Western blot analysis, i.e. a single band at the correct molecular weight (see below), and by RNAi methods using Western blot and immunofluorescence (shown in Chapter IV).

The following results are representative of data obtained for one of the monoclonal antibodies we put through our system. Additionally, we are able to purify several polyclonal antibodies with equivalent proficiency.

**Purification of anti HsXrcc3 IgG from raw ascites**

Anti HsXrcc3 monoclonal antibody in the form of raw ascites fluid was subjected to a protein A purification scheme developed in our lab. Raw ascites fluid (1 ml; clone 10F1/6, Novus Biologicals, Inc.) was run over a modified protein A bead column, washed with binding buffer at an appropriate pH to remove non-specific proteins, and the remaining IgG proteins were eluted by appropriate adjustment of the buffer pH. I also found that limiting the time of exposure of the antibody to extremes of pH was critical to obtaining functional antibody. Figure 3.1 illustrates the two components of the purification process, the flow through (lanes 3/4) and the elution (lanes 5/6) as well as the appropriate ladder and IgG standard (lanes 1 and 2, respectively). Lanes 3 and 4 (flow through in duplicate) show a low level signal for the IgG heavy and light chains. Heavy and light chain IgG bands (≈ 50 and 25 kDa, respectively) shown in the elution fraction (lanes 5/6) actually represent a minor fraction of the total protein in the flow through. In those instances where a larger amount of IgG remained in the flow through, this could be successfully purified by running the flow through over the column a second time. Average total recovery of IgG molecules was from 60 – 90%. The total elution volume in this experiment was 10 ml and 4 μl was loaded onto lanes 5 and 6. The estimated concentration in this case is 0.25 mg/ml and therefore the total yield from 1 ml of ascites fluid approximates 2.5 mg monoclonal IgG. Yields varied from 1 to 5 mg purified IgG per ml ascites fluid from different commercial preparations.

**FIGURE 3.1**

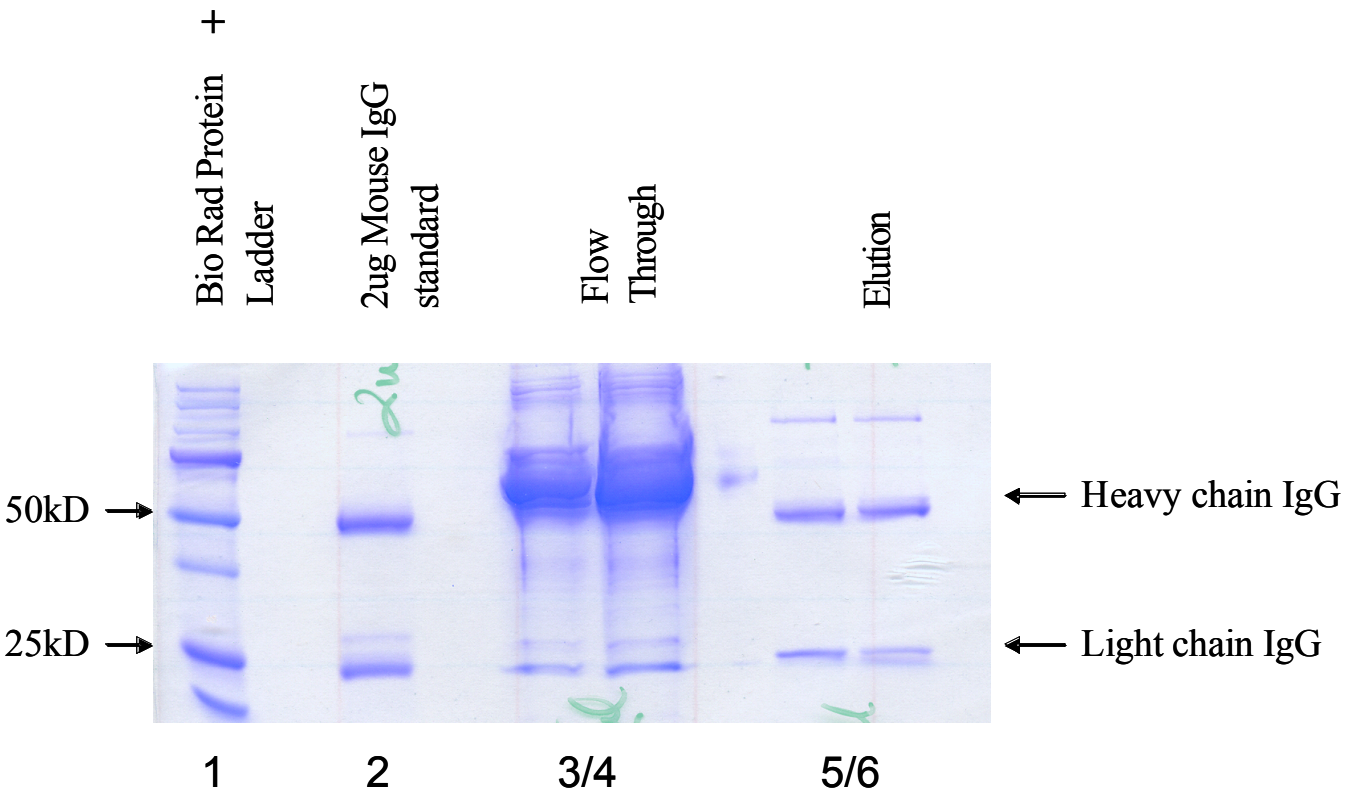
+
Bio Rad Protein Ladder
2ug Mouse IgG standard
Flow Through
Elution
50kD
25kD
Heavy chain IgG
Light chain IgG
1
2
3/4
5/6

**Figure 3.1 – Removal of IgG heavy and light chains from ascites fluid.** 10% Tris HCl gel stained with coomassie stain for protein detection in both the flow through and elution fractions of protein A purified monoclonal antibody. In addition, detection of an IgG standard and protein standards visualized.

It is important to note that we have successfully obtained active antibody from the residual amount that appeared in the flow through fraction by re-running that fraction over a fresh column. Also note that higher molecular weight bands appearing in lanes 5 and 6 are also present in the mouse IgG control lane and could represent non-reduced heavy chain dimers, or contaminating proteins. The elution fraction was dialyzed exhaustively against PBS and the preparation was stored at -20 °C at a final concentration of 1 mg/ml.

**Purification of anti HsXrcc3 monoclonal antibody enhances specificity and detection of Xrcc3 in whole cell extracts.**

To assess the efficacy of our purification procedure we performed Western blots on HEK293 whole cell extracts using the purified antibody *vs*. commercially obtained raw ascites fluid. HEK 293 cells were harvested and lysed as previously described in Chapter II. Total protein was determined with BCA protein Assay Kit (Pierce) and 60 μg total protein was loaded in lanes 1 and 2 (Fig. 3-2). Detection of the antibody was achieved using Visualizer™ Western Blot Detection Kit (Upstate, Inc). The Visualizer system provides a high level of detection not seen in conventional detection systems and requires low exposure times. This is beneficial as it is imperative to visualize any signal that exists on the blot using the purified antibody (lane 2) to ensure its specificity. Note that both lanes (lanes 1 and 2) are from the same gel and after transfer the blot was cut in two, ensuring that the gel, buffers or transfer process would not affect either sample differently. Additionally, incubation times in ECL and exposure times were equal.

**FIGURE 3.2**

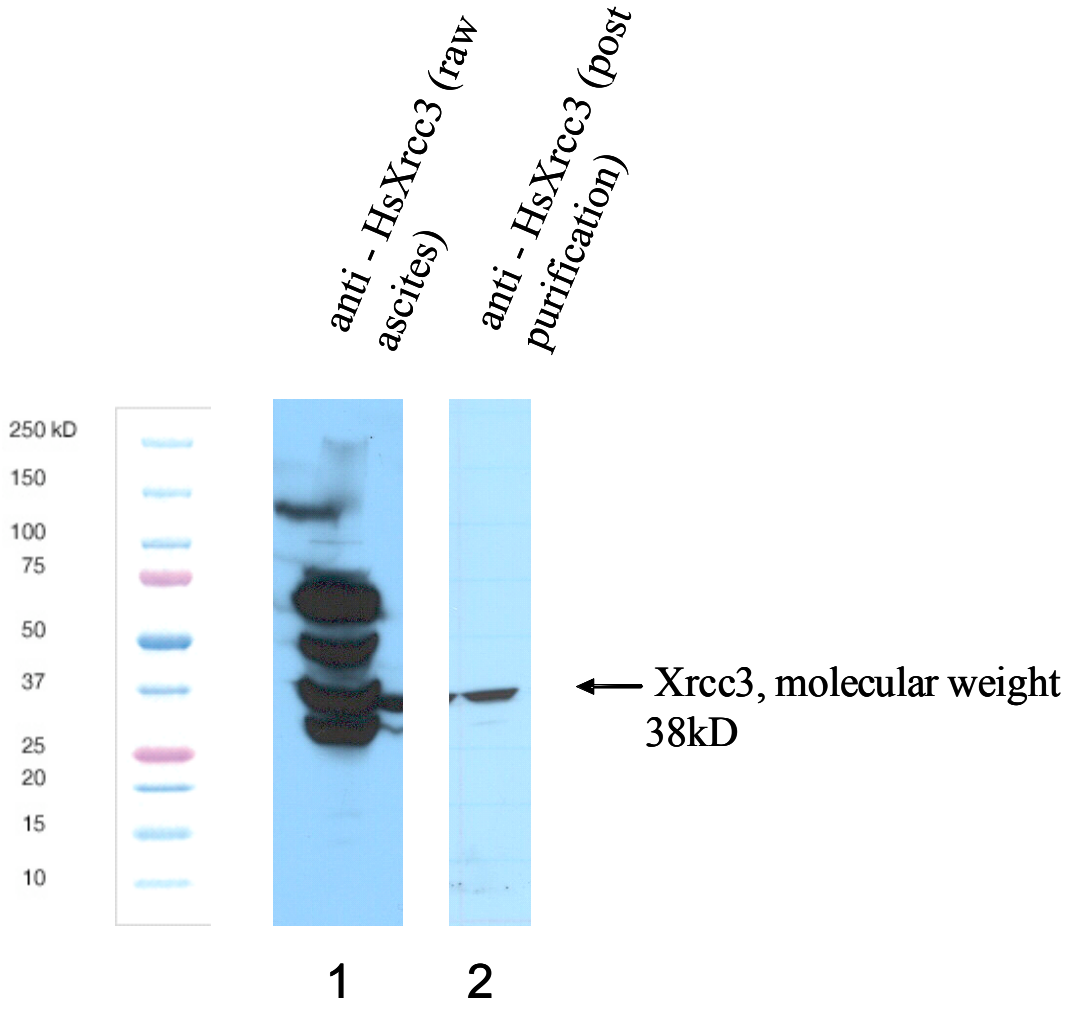
anti - HsXrcc3 (raw ascites)
anti - HsXrcc3 (post purification)
250 kD
150
100
75
50
37
25
20
15
10
1
2
Xrcc3, molecular weight 38kD

**Figure 3.2 - Purification of anti HsXrcc3 monoclonal antibody enhances specificity and detection of Xrcc3 in whole cell extracts.** Western blot developed using an anti HsXrcc3 monoclonal antibody on HEK293 whole cell extracts. 60ug total protein loaded in each lane. Lane 1 uses an ascites fluid containing the antibody. Lane 2 uses the same antibody following purification and dialysis into PBS. Two separate blots developed using equal ECL incubation times as well as exposure times.

Use of the raw ascites results in 4 strong bands and lesser amounts of 3 others appearing on the blot (Fig. 3.2, lane 1). In contrast, the blot developed using the purified Xrcc3 antibody showed a single band at the correct molecular weight (Fig. 3.2, lane 2). For the blots shown here primary antibodies, both ascites and purified, were used at a 1:1,000 dilution. Further dilution of the raw ascites, e.g. 1:5,000 and 1:12,000, resulted in only a minimal enhancement of the Xrcc3 band relative to cross-reacting bands. It is, therefore, clear by this comparison that the purification of the antibody enables clear and specific detection of the protein of interest. In Chapter IV, I use RNAi methods to provide further confirmation of the specificity of the purified antibody attained using the method described here.

**Purification of anti HsXrcc3 monoclonal antibody enhances specificity and detection of Xrcc3 in by Immunofluorescence (IF).**

I next set out to determine if the increased specificity as seen in Western blots would translate to immunofluorescence detection of HsXrcc3. The images in Figure 3.3 strongly suggest that separation of the targeted IgG molecule from other proteins in the ascites fluid enhances signal specificity (see Chapter IV) and also eliminates high level background staining. HEK293 cells exposed to 8 Gy ionizing radiation and were fixed and stained 2 hours post IR treatment as previously described in Chapter II. The top image (Fig. 3.3, panel 1) shows that foci do exist in both the cytoplasmic and nuclear compartments, however it is hard to discern the number and intensity of these foci because of the diffuse staining. In Figure 3.3 panel two, which is stained with our purified anti-HsXrcc3 monoclonal IgG, there a distinct lack of signal underneath the nuclear foci. This matches perfectly with the lack of signal outside the cells, i.e. the black area.

Thus, purification of the antibody provides a more distinct and specific image of the cellular localization of Xrcc3 in HEK293 cells. As shown in Chapters IV and VI, this increase in specificity and sensitivity is critical to our claims that significant amounts of Rad51, Rad51C and Xrcc3 exist in the cytoplasmic, but that the protein allocated to this compartment undergoes a dynamic sub-cellular re-distribution following DNA damage. Additionally, by removing the non-specific staining we were able to treat the cells with target specific siRNA and show that we all but eliminate the staining seen in panel 2 (see Chapter IV).

**FIGURE 3.3**

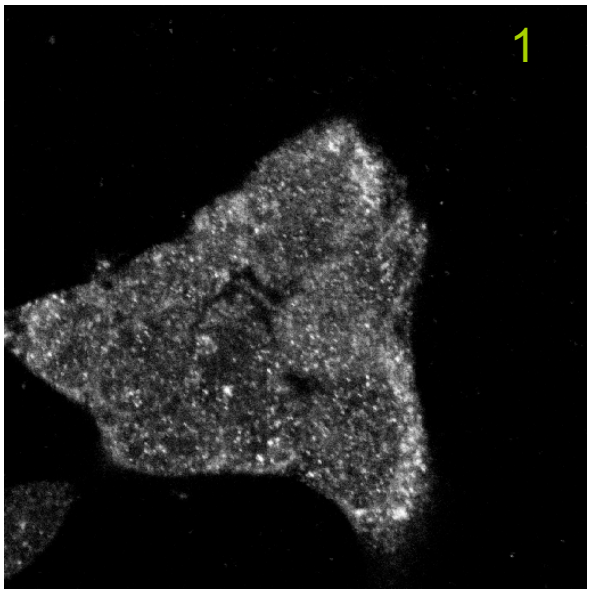


anti-HsXrcc3 (raw ascites – pre purification)

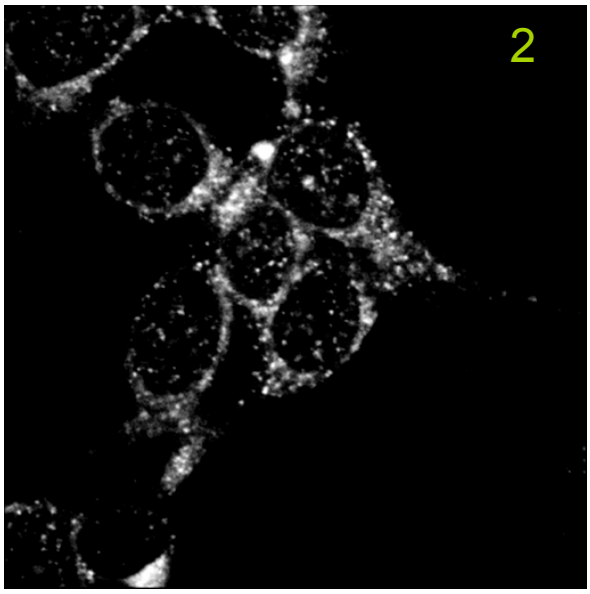


anti-HsXrcc3 (purified antibody)

**Figure 3.3 - Purification of anti HsXrcc3 monoclonal antibody enhances specificity and detection of Xrcc3 by Immunofluorescence.** HEK 293 cells were stained with anti HsXrcc3 contained in ascites fluid (panel 1) and anti HsXrcc3 purified into PBS (panel 2). Primary antibody was followed by a goat anti mouse Alexa 488 (grey). Images were taken using similar zoom and laser intensity settings to ensure continuity within samples. Primary antibodies were used at a dilution of 1:500, and secondaries at a dilution of 1:12,000.

**Collaborative development of purification processes and immunofluorescent studies**

As it was clear that we were able to purify the proteins necessary to answer the questions we had formulated about Rad51 and the paralog proteins, we would need to acquire volumes of antibodies in excess of 1-2 ml. I approached Novus Biologicals and Upstate, Inc with the data on the purification. I was able to organize a collaborative effort with both companies and have for the past two years been involved in successful research programs. The fact that the antibody purification led to such a significant improvement in the quality of the immunofluorescence images also led me to a collaboration with Leica Microsystems, Inc. The combination of these collaborations has provided me with the opportunity to explore the use of a new microscope technology under development at Leica (4Pi), and to use this technology to advance the cell biology and immunofluorescence efforts in the DNA repair field.

The following Figures 3.4 A and B are examples of some of the data found at **www.novusbio.com** and **www.upstate.com**. Figure 3.5 is an image of HeLa cells using the Upstate alpha-tubulin antibody in an application I have created for a new microscope technology called 4Pi. 4Pi microscopy improves light microscope resolution to approximately 100 nm (see Chapter VII).

**FIGURE 3.4**

A

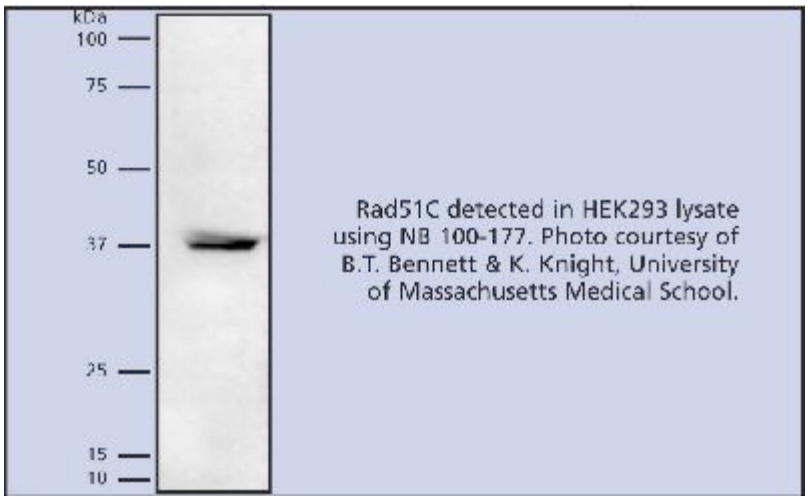


B

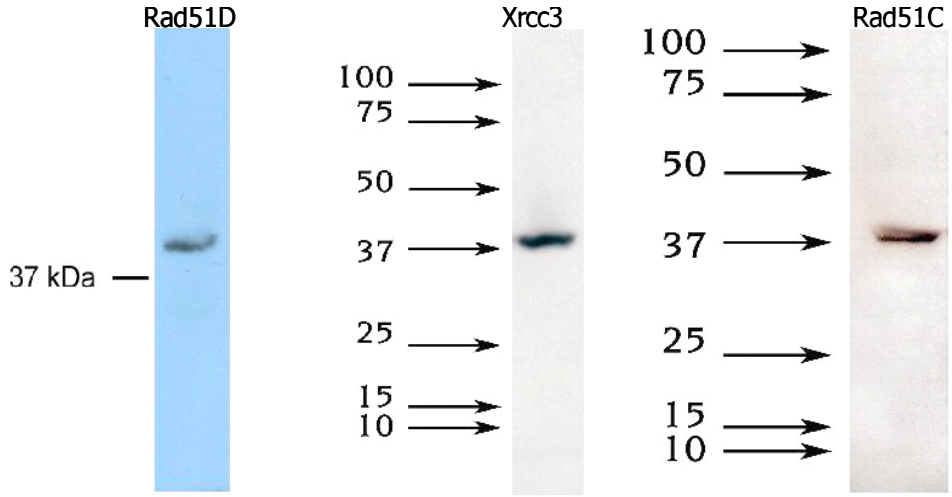


Rad proteins detected using HEK293 lysate and indicated antibodies (purified) at a dilution of 1:1,000. Photos courtesy of B. T. Bennett and K. Knight, University of Massachusetts Medical School.
(taken from Novus Biologicals website www.novus.com

**Figure 3.4A/B - Collaborative development of purification processes and immunofluorescent studies.** Full length western blots showing Rad51C (A) and Rad51D, Xrcc3 and Rad51C (separate citation) developed in our lab for use in demonstrating purification on Novus Biologicals web site.

**FIGURE 3.5**

## Anti-α-Tubulin, clone DM1A

HeLa cells stained with anti-α-Tubulin and visualized on the Leica 4 Pi imaging system at approximately 100 nm resolution. White bar is 309 nm. Image courtesy Brian Bennett, Leica Microsystems.

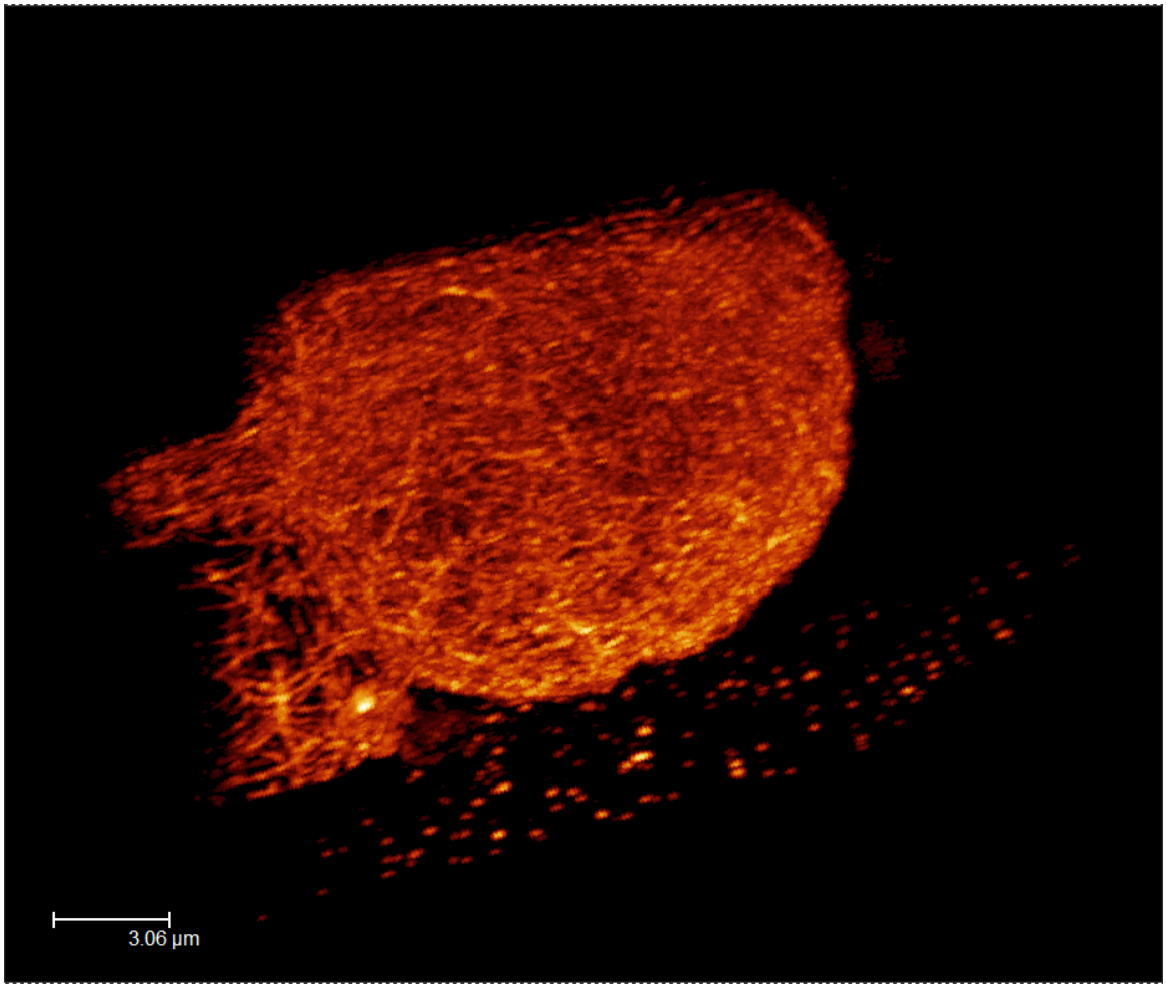

**Figure 3.5 – 4Pi image of HeLa cell stained for alpha tubulin.** HeLa cell stained for alpha Tubulin following DNA damage using 4Pi microscopy. Image is in an X, Z axis and is at approximately 100nm resolution. Below the cell are 100 nm beads used to calculate point spread function as a function of resolution within the image as in internal control for 4Pi.

# DISCUSSION

The work presented in this Chapter represents approximately 6 months of effort that included optimization of both the antibody purification as well as other aspects of my immunofluorescence methods and use of the confocal microscope. After the publication of the first manuscript (Forget, Bennett and Knight - 2004), I continued to address issues regarding antibody specificity and the accuracy of cellular staining patterns that we observed for these proteins. My motivation in part derived from my interaction with a prominent member of the DNA field during a poster session at an international meeting when I was presenting our recently published work. Because his group had been unsuccessful in using these antibodies for immunofluorescence applications, he chose to publicly berate me and dismiss my work as an artifact of poor immunofluorescence technique. Admittedly, this helped to push the work I was planning to do already – to develop an optimized system for collection of immunofluorescence data of DNA repair proteins in which controls are included to demonstrate antibody specificity and validation of the immunofluorescence signal. As presented in Chapter IV, these controls should include Western blots showing a single band at the correct molecular weight, depletion of that band using cells treated with a target-specific siRNA, as well as depletion of the immunofluorescence signal in the same siRNA-treated cells. Of course, if a genetic knock-out cell line is available this would serve as an excellent control. Because we have found that many commercially available antibodies fall far below standards for specificity as demonstrated by Western blot and immunofluorescence methods, I strongly believe that the onus is on the researcher to show in a manuscript that the antibodies used pass a stringent quality control.

## PREFACE TO CHAPTER IV

The work in Chapter IV provides the first visualization of endogenous Rad51C in human cells. Further, it shows for the first time that the cellular localization of Rad51C seems to mimic that of Xrcc3, supporting biochemical claims that they exist in a stable heterodimer. These studies also suggest a coordinated response of Rad51, Rad51C and Xrcc3 and may provide clues as to the timing of cellular events and possible protein interactions in response to DNA damage. Finally, this work reveals the first defined cellular function for a Rad51 paralog protein – we find that Rad51C regulates ubiquitin-mediated proteolysis of Rad51 following DNA damage.

The experimental system employed herein is an advance from that presented in Chapter II in that we combined a vast improvement in our immunofluorescent protocol with further optimized RNAi knock down of endogenous proteins. This allowed an investigation into the interdependency of Rad51, Xrcc3 and Rad51C regarding their cellular localization and response to DNA damage.

I performed all aspects of the experimental work, with assistance from Rachel Litman for the co-immunoprecipitation studies. Writing the manuscript was the combined effort of myself and Dr. Knight.

# CHAPTER IV

# CELLULAR LOCALIZATION OF HUMAN RAD51C AND REGULATION OF UBIQUITIN-MEDIATED PROTEOLYSIS OF RAD51


## Abstract

Rad51-catalyzed homologous recombination is an important pathway for repair of DNA double strand breaks and maintenance of genome integrity in vertebrate cells. Five proteins referred to as Rad51 paralogs promote Rad51 activity and are proposed to act at various, and in some cases, multiple stages in the recombination pathway. Imaging studies of native Rad51 have revealed its cellular response to DNA damage, yet visualization of the paralog proteins has met with limited success. In this study, we are able to detect endogenous Rad51C and Xrcc3 in human cells. In an effort to determine how Rad51, Rad51C and Xrcc3 influence the pattern of localization of each other over the time course of DNA damage and repair, we have made the unexpected observation that Rad51 degradation via the ubiquitin-mediated proteasome pathway occurs as a natural part of recombinational DNA repair. Additionally, we find that Rad51C plays an important role in regulating this process.

## Introduction

Repair of DNA double strand breaks resulting from either endogenous sources, e.g. errors in DNA replication, or following exposure to exogenous mutagens is critical for cell survival and the maintenance of genome integrity. Homologous recombination is an important pathway in mammalian cells for DSB repair (Pierce et al., 1999; Johnson and Jasin, 2001; Thompson and Schild, 2001). The Rad51 protein provides the central activity in this pathway by catalyzing formation of crossover structures (Holliday junctions) between damaged DNA and an undamaged homologous chromosome, most frequently a sister chromatid (Sung et al., 2003; West, 2003). A group of five Rad51-like proteins (Rad51 paralogs; Rad51B/L1, Rad51C/L2, Rad51D/L3, Xrcc2 and Xrcc3), originally identified in complementation screens and by sequence alignment with Rad51 (Albala et al., 1997; Tambini et al., 1997; Cartwright et al., 1998; Dosanjh et al., 1998; Liu et al., 1998), have been shown to play important roles in supporting Rad51 function. Vertebrate cells deficient for any of the five paralogs show increased sensitivity to DNA damaging agents and increased levels of chromosomal abnormalities (Tebbs et al., 1995; Liu et al., 1998; Thacker, 1999; Sonoda et al., 2001; Takata et al., 2001; Thompson and Schild, 2001; Yoshihara et al., 2004). Suppression of these defects is best achieved by transfection of the specific gene itself and not by over expression of *RAD51* or other paralog genes (Takata et al., 2001; French et al., 2002), thus providing evidence that each paralog has an important, non-redundant function in homologous recombination. In response to DNA damage, the Rad51 protein forms distinct nuclear foci that appear to associate with DNA breaks (Haaf et al., 1999; Tashiro et al., 2000; Aten et al., 2004). Each of the five paralog proteins is required for DNA damage-induced nuclear Rad51 focus formation, demonstrating a likely role early in the homologous recombination pathway (Bishop et al., 1998; Takata et al.,

2001; Yoshihara et al., 2004). Additional evidence supports other roles for the paralog proteins at different points in the homologous recombination pathway. For example, defective processing of recombination intermediates is observed in both hamster and *Arabidopsis XRCC3*$^{-/-}$ cells (Brenneman et al., 2000; Bleuyard and White, 2004). Additionally, recent studies show that Rad51C and Xrcc3 may play a direct role in Holliday junction resolution (Liu et al., 2004a).

Specific protein-protein interactions between Rad51 paralog proteins have been demonstrated (Schild et al., 2000) and several complexes have been identified (Braybrooke et al., 2000; Kurumizaka et al., 2001; Masson et al., 2001b; Sigurdsson et al., 2001; Liu et al., 2002; Miller et al., 2002; Wiese et al., 2002). It has been suggested that because Rad51C is present in three of the four complexes identified to date (BC, CX3, and BCDX2), it may play a more prominent role in regulating Rad51 and Rad51 paralog functions than other paralogs (French et al., 2003). Additionally, Rad51C may be involved in trafficking recombination proteins to the nucleus (French et al., 2003). Biochemical studies using purified paralog protein complexes have demonstrated DNA-dependent ATPase, DNA binding, substrate-specific strand transferase, and strand-separation activities (Thacker, 2005) but an integrated model of how these functions contribute to the homologous recombination pathway in the cell remains to be determined. Other than their requirement for the formation of DNA damage-induced Rad51 nuclear foci, little is currently known regarding specific cellular functions of the paralog proteins.

In this study we use immunofluorescence imaging to show the cellular distribution of endogenous human Rad51C and Xrcc3 before DNA damage and over an extended time course of DNA damage and repair. The data show that both proteins localize to positions at the nuclear

periphery and form distinct foci within the nucleus both before and after DNA damage. RNAi studies designed to understand the potential interdependence of the cellular localization of each protein have led us to discover a novel and unexpected function for Rad51C - regulation of ubiquitin-mediated degradation of Rad51.

## Results

### Cellular localization of Rad51, Rad51C and Xrcc3 prior to DNA damage and throughout a time course of DNA damage and repair

To detect the cellular localization of endogenous Rad51, Rad51C and Xrcc3 proteins, HEK293 cells were fixed and stained for each protein prior to damage and at t = 0.5, 1, 2, 4, 6 and 8 hours following exposure to ionizing radiation (IR, 8 Gy). We followed the staining of gamma H2AX as a marker for DNA double-strand breaks (Rogakou et al., 1998). At t = 0, only minor background gamma H2AX staining is observed (Figs. 4.1 – 4.3). At t = 0.5 hr there is a dramatic increase in the appearance of nuclear gamma H2AX. This persists for 6 hr and diminishes at t = 8 hr, indicative of repair of double-strand breaks. For Rad51, we find that prior to DNA damage protein staining appears in the cytoplasm, and there are occasional nuclear foci (Fig. 4.1). These have been previously described as S-phase foci (Chen et al., 1998; Chen et al., 1999; Tarsounas et al., 2004b). Significant levels of cytoplasmic Rad51 have also been observed by Western analysis of subcellular fractions (Yoshikawa et al., 2000; Davies et al., 2001).

**FIGURE 4.1**

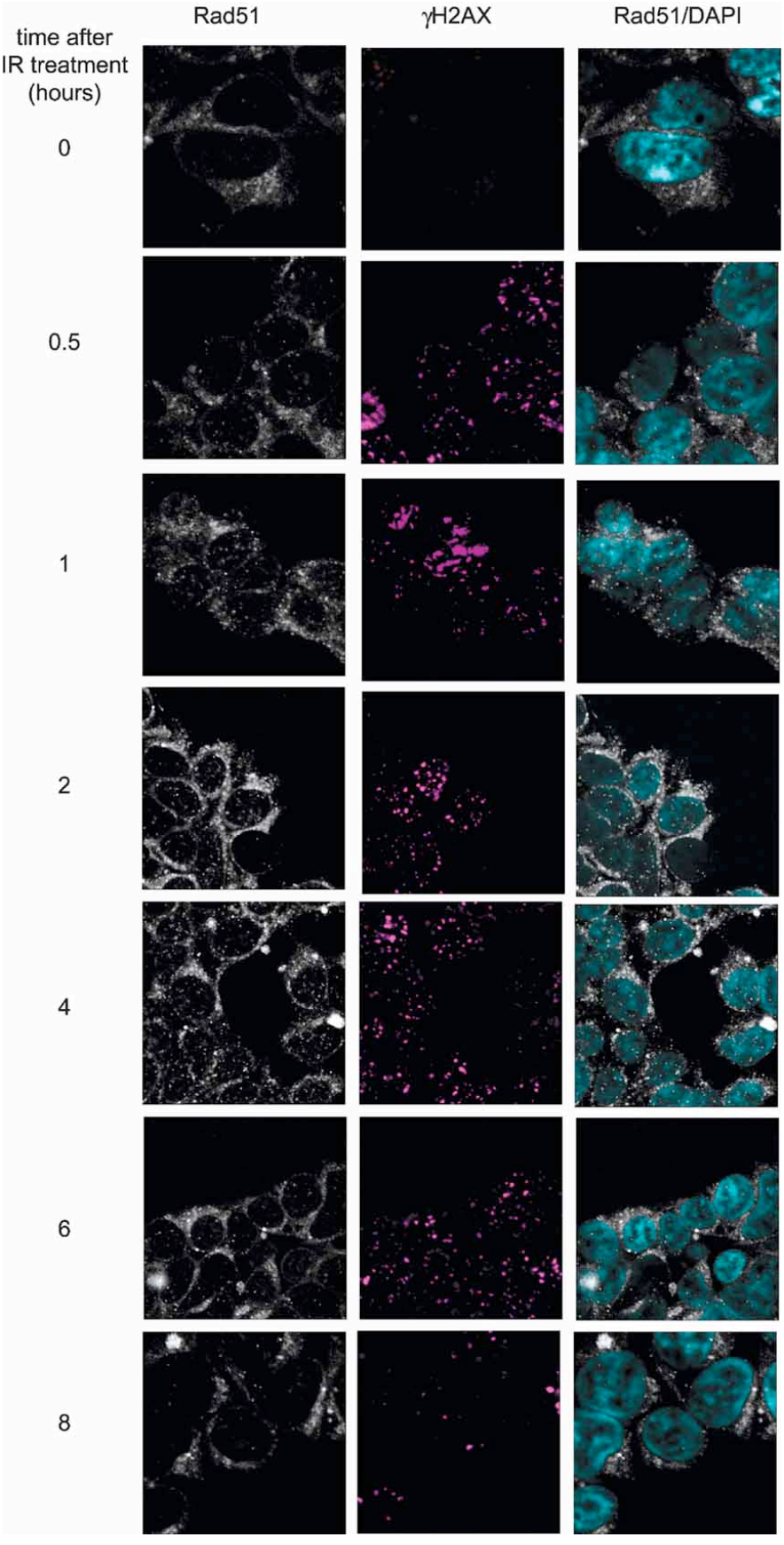
Rad51
γH2AX
Rad51/DAPI
time after IR treatment (hours)
0
0.5
1
2
4
6
8

**Figure 4.1 - Ionizing radiation-induced nuclear Rad51 foci form early following DNA damage and disassemble over an 8 hour time course of DNA repair.** HEK293 cells were stained with anti-Rad51 (gray), anti-gamma H2AX (magenta), and DAPI (cyan) at the indicated times before and after exposure to ionizing radiation (8 Gy).

**FIGURE 4.2**

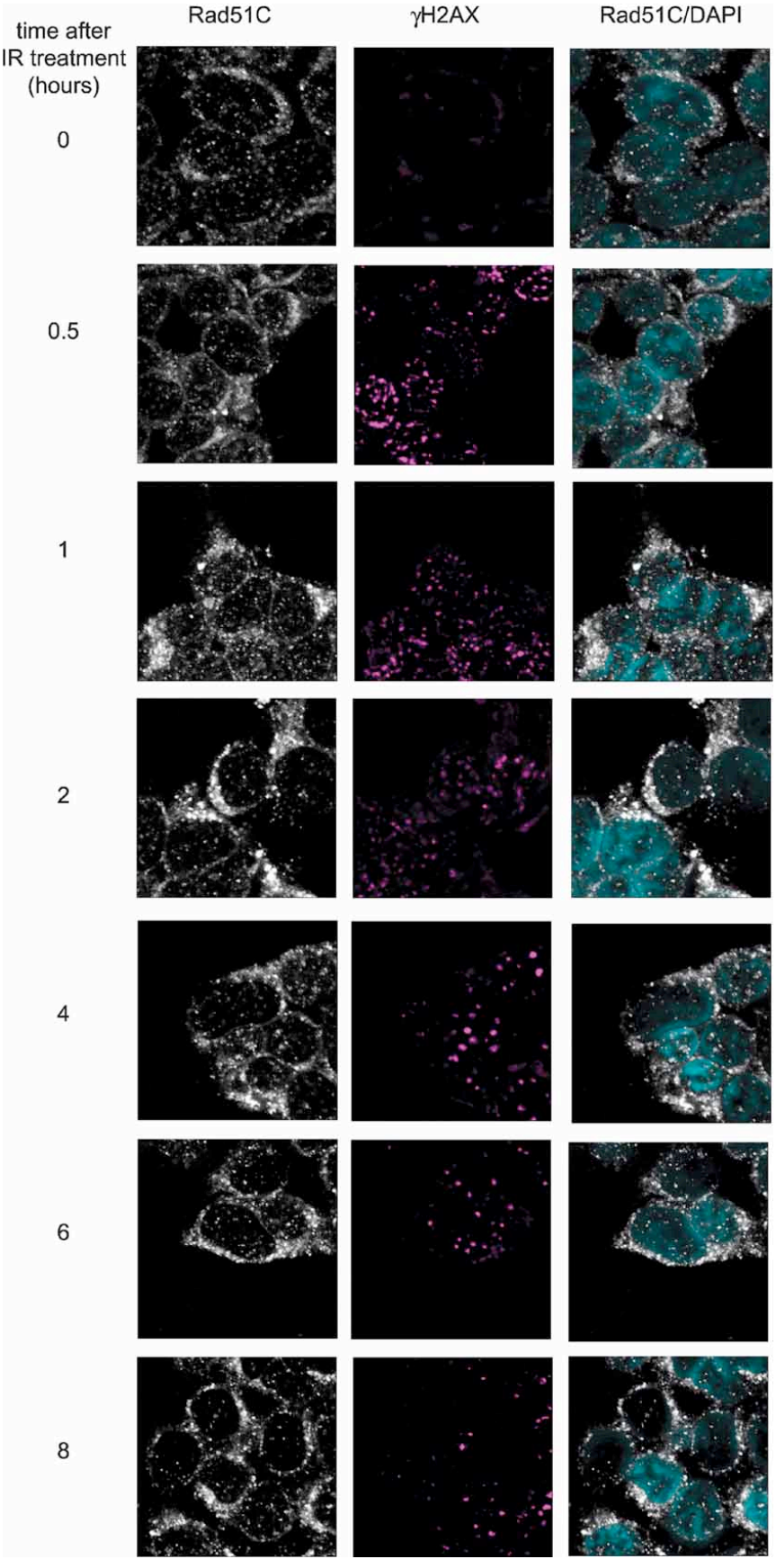
time after IR treatment (hours)
Rad51C
γH2AX
Rad51C/DAPI
0
0.5
1
2
4
6
8

**Figure 4.2 - Rad51C forms distinct nuclear foci prior to DNA damage that persist throughout the time course of DNA repair.** HEK293 cells were stained with anti-Rad51C (gray), anti-gamma H2AX (magenta), and DAPI (cyan) at the indicated times before and after exposure to ionizing radiation (8 Gy).

**FIGURE 4.3**

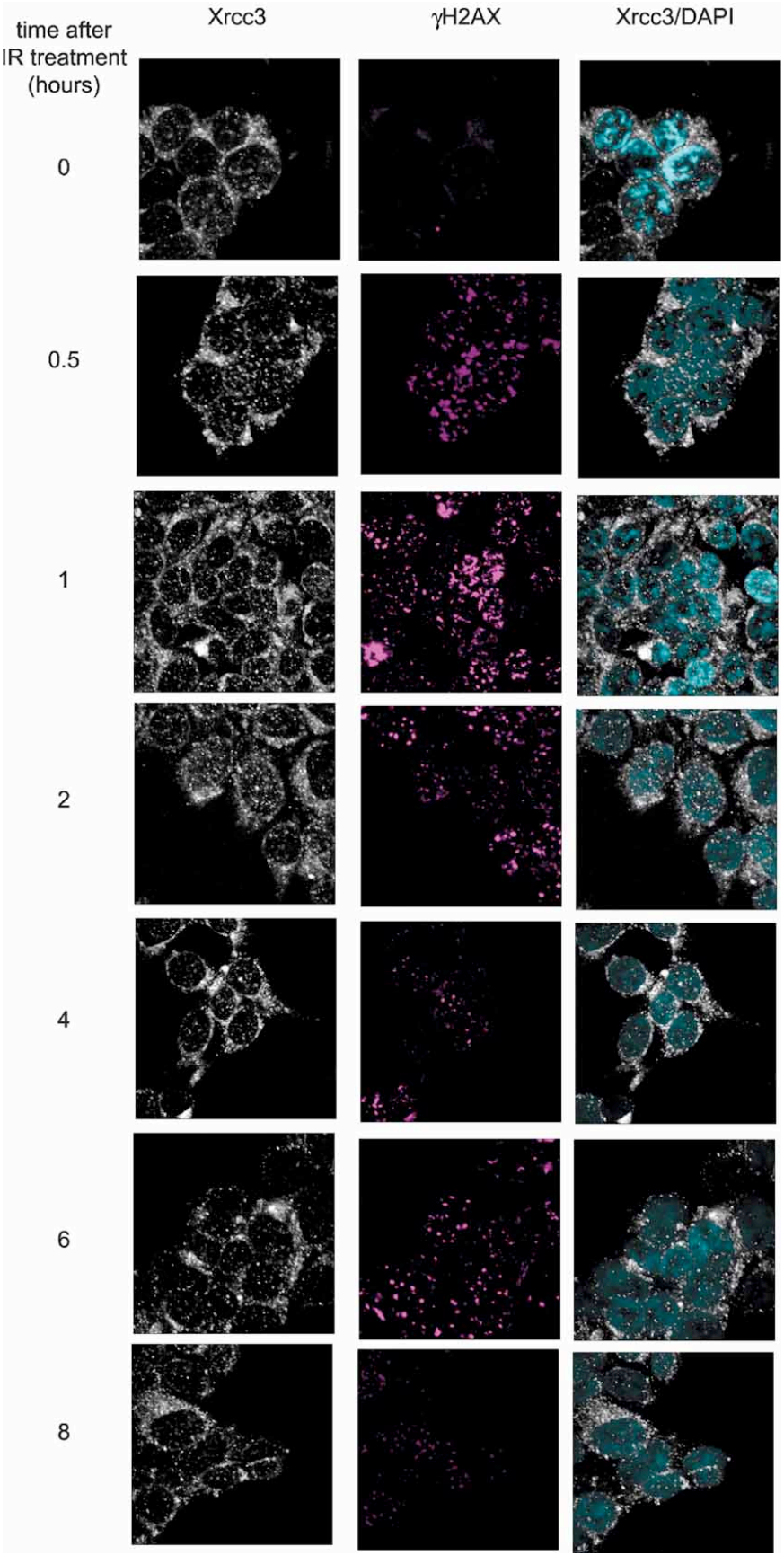
time after IR treatment (hours)
Xrcc3
γH2AX
Xrcc3/DAPI
0
0.5
1
2
4
6
8

**Figure 4.3 - Nuclear Xrcc3 foci are present at all times before and after exposure of cells to ionizing radiation.** HEK293 cells were stained with anti-Xrcc3 (gray), anti-gamma H2AX (magenta), and DAPI (cyan) at the indicated times before and after exposure to ionizing radiation (8 Gy).

At t = 0.5 hr, there is a distinct increase in the number of nuclear foci, and as time progresses the number and size of these foci peak between 2 and 4 hr. At t = 6 hr the number of nuclear Rad51 foci is noticeably diminished, and at 8 hr the staining appears similar to that seen at t = 0 (Fig. 4.1). We note also that while cytoplasmic staining of Rad51 is somewhat diffuse at t = 0, 0.5 and 1 hr following exposure to ionizing radiation, at 2 and 4 hr Rad51 cytoplasmic staining is concentrated more at the nuclear periphery, and returns to a more diffuse appearance at t = 8 hr. For all time points, > 90% of the cell population showed similar staining patterns.

In contrast to Rad51, staining for endogenous Rad51C revealed an unexpected pattern in that distinct nuclear foci were present in all cells prior to DNA damage (Fig. 4.2). As for Rad51, Rad51C also appears to concentrate at the nuclear periphery following DNA damage. While this perinuclear staining pattern appears slightly more diffuse at t = 0 and 0.5 hr relative to its more distinct appearance throughout the remainder of the time course, judging from the entire field of cells it is difficult to say to what extent this is a DNA damaged-induced phenomenon. However, it is clear from the data in Figures 4.1 and 4.2 that while the staining pattern of Rad51 shows a significant response to DNA damage and repair, especially with regard to nuclear focus formation, changes in the cellular staining pattern of Rad51C are more subtle. For all time points the number of cells containing Rad51C foci both before and after DNA damage was > 90%. Our observation of endogenous Rad51C in both the cytoplasm and nucleus is supported by previous studies in which endogenous human Rad51C was shown to exist in both cellular compartments using Western blot analysis of subcellular fractions (Miller et al., 2005).

The cellular appearance of endogenous Xrcc3 is similar to that observed for Rad51C (Fig. 4.3). Staining of Xrcc3 shows distinct nuclear foci prior to DNA damage (Forget et al., 2004) as well as clusters of protein in the cytoplasm and perinuclear region (Fig. 4.3). At 6 and 8 hr following exposure to ionizing radiation, the number of nuclear Xrcc3 foci appear to diminish, but as for Rad51C this change is significantly more subtle than that observed for Rad51 (Fig. 4.1). Also, perinuclear clustering of Xrcc3 appears more concentrated following DNA damage (for example, see Fig. 4.3, t = 4 hr ) as compared to a more diffuse staining at t = 0. Similar to Figures 4.1 and 4.2, > 90% of the cells at each time point showed similar staining patterns. The fact that the cellular staining pattern of Xrcc3 mimics that of Rad51C supports the observation that these two proteins can exist as a stable heterodimer (Kurumizaka et al., 2001; Masson et ., 2001a; Wiese et al., 2002). The primary antibodies used to stain both Rad51C and Xrcc3 are mouse monoclonals of the same iso-type, which prevents co-localization studies, but methods to achieve this are currently under development. Formation of DNA damage-induced nuclear Rad51 foci requires Xrcc3 as well as Rad51C and we now observe both Xrcc3 and Rad51C in nuclear foci prior to DNA damage. Whether these foci are centers at which Rad51C and Xrcc3 function, or serve to sequester both proteins for release during DNA repair remains to be determined (see Chapter VIII, Discussion and Future Directions).

**Validation of antibody specificity**

Prior use of the unpurified anti-Rad51C and Xrcc3 monoclonal antibodies on HEK293 and HeLa whole cell extracts revealed multiple bands in Western blots, thereby precluding their use in immunofluorescence studies (data not shown). However, we purified the anti-Xrcc3 monoclonal using a protein-A Sepharose procedure (http://www.novus-

biologicals.com/data_sheet.php/81/S/xrcc3/0) and have been able to successfully use this antibody in immunofluorescence studies (Forget et al., 2004). In the present study, monoclonal antibodies against Rad51C and Xrcc3 obtained from Novus Biologicals, Inc. were protein-A purified. To demonstrate that the staining patterns observed in Figures 4.1, 4.2 and 4.3 are specific to the proteins of interest, we analyzed immunofluorescence images of cells treated with small interfering RNAs (siRNAs). HEK293 cells were transfected with siRNAs specific to Rad51, Rad51C or Xrcc3 and exposed to ionizing radiation (8 Gy) 48 hr later. Two hours following ionizing radiation treatment, cells were fixed and stained using the procedure identical to that used in Figures 4.1, 4.2 and 4.3. We find that in each case the signal for Rad51, Rad51C and Xrcc3 is almost completely eliminated by its specific siRNA (Fig. 4.4A). A low level, residual staining can in part be explained by the slight background contributed by the AlexaFluor488 secondary antibody (Fig. 4.4B). The fact that staining with DAPI and anti-gamma H2AX is localized exclusively to the nucleus precludes the possibility that cytoplasmic and perinuclear staining of Rad51, Rad51C and Xrcc3 result from disruption of the nuclear membrane during fixation. Again, our observations are supported by previous studies of various human cell types, e.g. pancreatic and breast epithelial cells, which show a significant amount of cytoplasmic Rad51 (Yoshikawa et al., 2000; Davies et al., 2001), and HeLa cells showing cytoplasmic Rad51C (Miller et al., 2005).

**FIGURE 4.4A/B/C/D**

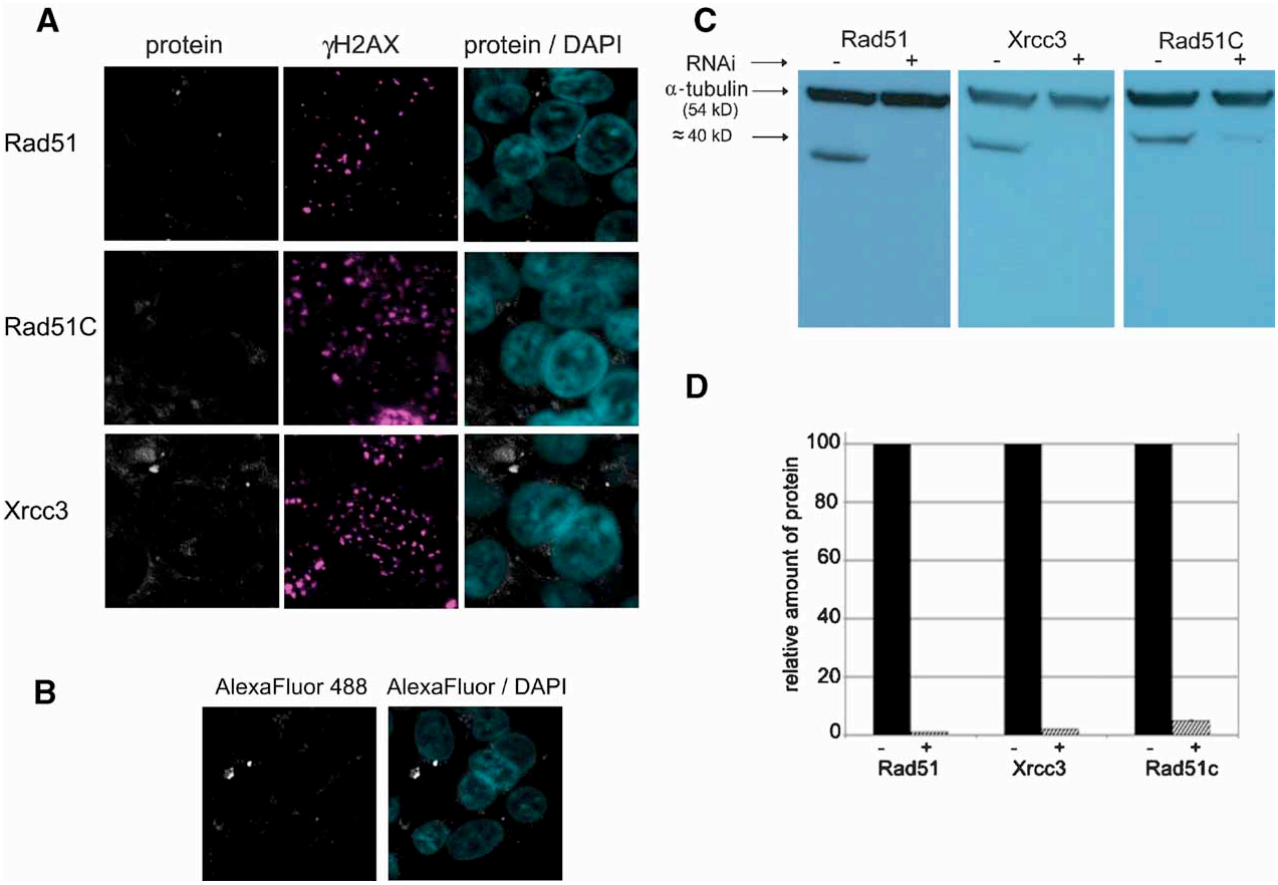

**Figure 4.4A/B/C/D - Antibodies and siRNAs are specific to the designated protein.**

(A) Cells were stained with antibodies against the indicated protein (gray), anti-gamma H2AX (magenta), and DAPI (cyan) two hours following exposure to ionizing radiation (8 Gy). (B) Cells were stained only with DAPI (cyan) and AlexaFluor488 secondary antibody (gray) that is used in all other immunofluorescence images to indicate the small background contribution made by this antibody. (C) Western blots were performed using anti-Rad51, anti-Rad51C or anti-Xrcc3 on whole cell extracts from cells incubated with the indicated siRNAs. Protein molecular mass is from http://www.hprd.org/protein: Rad51 = 36,968 Da; Xrcc3 = 37,842; Rad51C = 42,192. (D) Relative amounts of each protein following treatment with specific siRNAs were determined from scans of Western blots from 3 separate experiments.

The specificity of the primary antibodies, as well as the siRNAs, was further demonstrated by Western blot analysis of whole cell extracts. The data show that siRNAs directed against Rad51, Rad51C or Xrcc3 specifically reduce the amount of each protein by ≥ 95% (Fig. 4.4C and D). Coomassie-stained gels show a large number of bands both above and below the position of each protein of interest (not shown), yet the purified primary antibodies directed against each protein reveal only that protein (Fig. 4.4C). No cross-reacting protein was visible in many repeated Western blots of HEK293 whole cell extracts using each of the primary antibodies against Rad51, Rad51C and Xrcc3. Having established the specificity of both the siRNAs and the primary antibodies, we next performed experiments to determine the effect that knock down of each protein would have on the others.

**Loss of Rad51C results in degradation of Rad51 following DNA damage**

HEK293 cells transfected as above with siRNAs against Rad51, Rad51C or Xrcc3 were exposed to 8 Gy ionizing radiation and fixed 2 hours later. As expected, treatment of cells with Rad51 specific siRNAs resulted in specific loss of Rad51 staining (Fig. 4.5A). We find that Rad51C staining is unaffected by Rad51 specific siRNAs, and in agreement with recent studies we find that this treatment results in no change in Xrcc3 staining (Forget et al., 2004), and (Fig. 4.5B and C, respectively). Therefore, while formation of DNA damage-induced Rad51 foci requires each of the five Rad51 paralog proteins (Bishop et al., 1998; Takata et al., 2001), formation of Rad51C and Xrcc3 foci does not require Rad51.

**FIGURE 4.5**

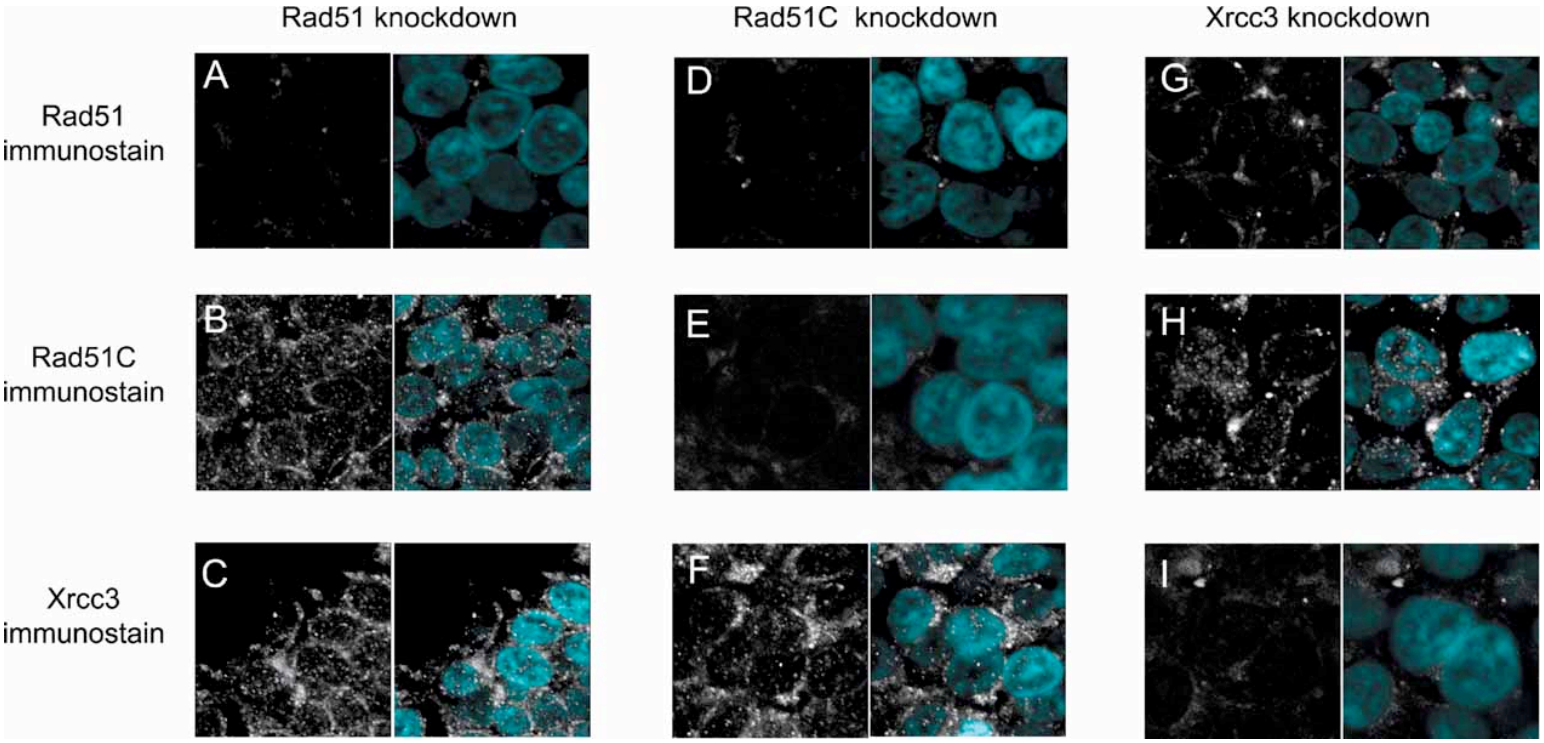
Rad51 knockdown
Rad51C knockdown
Xrcc3 knockdown
Rad51 immunostain
Rad51C immunostain
Xrcc3 immunostain
A
B
C
D
E
F
G
H
I

**Figure 4.5 - Knockdown of Rad51C results in complete loss of Rad51 immunostaining following DNA damage**. Cells were incubated with siRNAs directed against Rad51 (A-C), Rad51C (D-F), or Xrcc3 (G-I) for 46 hours and then treated with ionizing radiation (8 Gy). Two hours following DNA damage cells were stained using anti-Rad51 (A, D, G), anti-Rad51C (B, E, H) or anti-Xrcc3 (C, F, I) and DAPI. The images in panels A, E and I are the same as those shown in Figure 4.4A.

induced Rad51 foci requires each of the five Rad51 paralog proteins (Bishop et al., 1998; Takata et al., 2001), formation of Rad51C and Xrcc3 foci does not require Rad51.

Cells treated with siRNAs against Rad51C showed the expected loss of Rad51C staining (Fig. 4.5E), and while the total amount of Xrcc3 staining in these cells appears somewhat reduced (Fig. 4.5F) relative to non-siRNA treated cells (Fig. 4.3), the general Xrcc3 staining pattern in the nucleus, cytoplasm and perinuclear region remained very similar to non-treated cells. Remarkably however, we observe that treatment of cells with Rad51C-specific siRNA results in a total loss of Rad51 staining (Fig. 4.5D). Given the data shown below, and the fact that all siRNAs used in this study had no significant sequence similarity, this effect did not result from direct knock down of Rad51 mRNA by Rad51C siRNA.

Cells treated with siRNAs against Xrcc3 showed the expected loss of Xrcc3 (Fig. 4.5I), as well as the expected inability to form DNA damage-induced nuclear Rad51 foci (Fig. 4.5G). However, cellular staining of Rad51 is still apparent, although it appears to be somewhat reduced relative to cells not treated with Xrcc3 siRNAs (Fig. 4.1, 2 hr panel). Staining of Rad51C (Fig. 3.5H) is similar to that seen in untreated cells (Fig. 4.2). Therefore, these data reveal an entirely unexpected result in that knock down of Rad51C appears to result in loss of Rad51 following DNA damage.

To further explore this idea, we performed Western blot analysis of HEK293 cells treated with siRNAs against each protein and compared the levels of each of the other proteins both before and 2 hrs after DNA damage (8 Gy, ionizing radiation). In Figure 4.6A we show a Rad51 blot of

extracts from cells treated with each siRNA. In control cells not treated with siRNA, there appears to be a slight increase in the total amount of Rad51 following ionizing radiation exposure (lanes 1 and 2), consistent with a small cell cycle-dependent increase observed previously (Chen et al., 1997; Daboussi et al., 2002). Cells treated with Rad51 siRNA show a specific loss of protein in the absence (lane 3) or presence (lane 6) of IR exposure. Cells treated with Xrcc3 siRNA show little effect on the total amount of Rad51 with or without DNA damage (lanes 4 and 7). In contrast, cells treated with Rad51C siRNA show nearly a complete loss of Rad51 following exposure to IR (lane 8) and what appears to be an approximate 20% decrease in Rad51 protein levels in the absence of ionizing radiation exposure (lane 5). Previous studies (Lio et al., 2004) have shown a transient decrease in Rad51 levels of approximately 70-80% in HeLa cells treated with Rad51C siRNA but not exposed to DNA damage (see Chapter VIII, Discussion and Future Directions). We note also that studies of the Rad51C defective hamster cell line irs3 show little effect on levels of Rad51 prior to DNA damage (French et al., 2002). In that study there is still some Rad51 present in irs3 cells following DNA damage but it is unclear if a possible truncated form of Rad51C that may result from one of the exon 6 deleted transcripts still functions at some level to prevent loss of Rad51.

**FIGURE 4.6A/B/C**

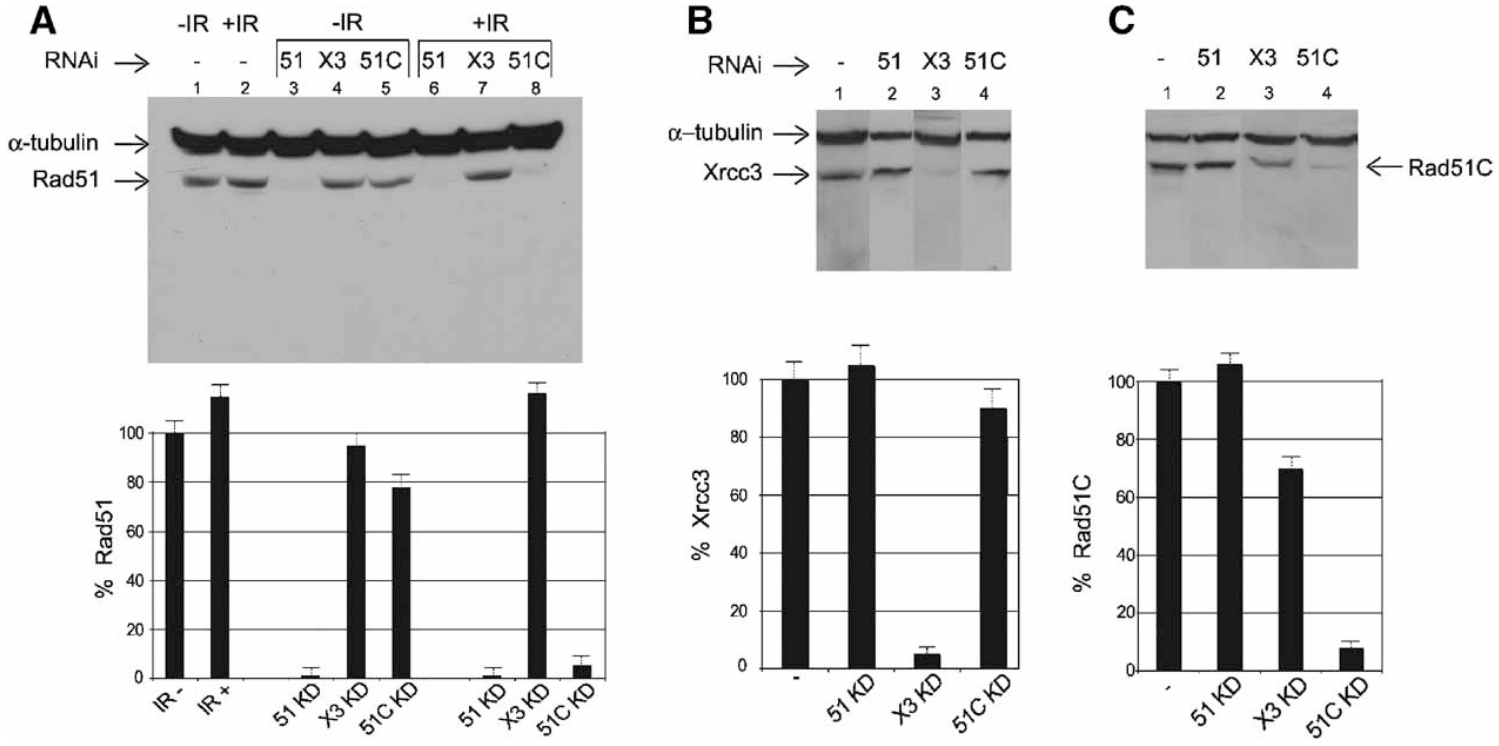

**Figure 4.6A/B/C - Lack of Rad51C results in degradation of Rad51.** (A) Western blot developed with anti-Rad51 using whole cell extracts from cells treated with the indicated siRNAs 48 hr prior to ionizing radiation exposure. Extracts were obtained from cells that had not been exposed to DNA damage (-IR) or two hours following exposure to 8 Gy ionizing radiation (+IR). (B and C) Western blots developed with anti-Xrcc3 and anti-Rad51C, respectively. Whole cell extracts were obtained from cells treated with the indicated siRNAs for 48 hr followed by exposure to ionizing radiation (8 Gy) and harvested 2 hr later. Histograms accompanying each blot show relative amounts of each protein averaged over 3 separate experiments.

Western blots stained with either anti-Xrcc3 (Fig. 4.6B) or anti-Rad51C (Fig. 4.6C) again show specific loss of the RNAi-targeted protein. Additionally, while treatment of cells with Rad51 siRNA showed no decrease in the levels of either Xrcc3 or Rad51C (lane 2 in Figs. 4.6B and C), treatment with Rad51C siRNA resulted in a slight decrease in Xrcc3 (Fig. 4.6B, lane 4). On the other hand, treatment of cells with Xrcc3 siRNA resulted in an approximate 30% decrease in the level of Rad51C (Fig. 4.6C, lane 3). The extracts used in Figures 4.6B and 4.6C are from cells exposed to ionizing radiation and very similar results are seen using cells not exposed to ionizing radiation (not shown). However, Lio et al. (2004) have reported a more substantial loss of Xrcc3 in HeLa cells treated with Rad51C siRNAs but not exposed to DNA damage. Our data show that in no instance was the decrease in protein levels nearly as dramatic as that seen for Rad51 following treatment of cells with Rad51C siRNA. Therefore, together with the immunofluorescence images in Figure 4.5, these data strongly support the idea that Rad51C serves to protect Rad51 against intracellular proteolysis, particularly following DNA damage.

**Rad51C protects Rad51 from ubiquitin-mediated degradation that is enhanced following DNA damage**

To investigate the mechanism of Rad51 degradation that occurs in the absence of Rad51C, we performed the following experiment using epoxomicin, a proteasome-specific inhibitor . Cells treated with Rad51C siRNAs for 48 hr were exposed to ionizing radiation and incubated for an additional 2 hr. One hour prior to IR treatment epoxomicin was added to a final concentration of 5 μM. Cells were harvested and Rad51 was immunoprecipitated. Controls included cells not exposed to ionizing radiation, as well as mock epoxomicin treatment (DMSO alone in all – epoxomicin lanes in Fig. 4.7). The Western blots in Figure 4.7A were developed using mouse

monoclonal anti-Rad51 and anti-mouse secondary antibodies, and therefore show the heavy and light chains of the monoclonal anti-Rad51 used for immunoprecipitation. Although these results reveal more Rad51 following ionizing radiation exposure of Rad51C siRNA treated cells (Fig. 4.7A, lane 3) than the Western blot of whole cell extracts from similarly treated cells (Fig. 4.6A, lane 8), we note that epoxomicin results in an approximate 3-fold increase in the level of Rad51 whether cells had been exposed to ionizing radiation or not (Fig. 4.7A, lane 1 vs. 2, and lane 3 vs. 4). Therefore, inhibition of the proteasome clearly increases the steady state level of Rad51. These blots were stripped and re-probed with rabbit anti-ubiquitin and anti-rabbit secondary antibodies (Fig. 4.7B). Lanes 6 and 8 reveal a significant band of ubiquitinated Rad51 migrating at a position on the gel that approximates the molecular mass of Rad51 plus four ubiquitin chains. This number of Ub chains is suggested to be the minimum signal for targeting to the proteasome (Lam et al., 2002). Cells not treated with Rad51C siRNA showed no detectable ubiquitinated-Rad51 in either the absence or presence of epoxomicin when not exposed to DNA damage (Fig. 4.7C, lanes 9 and 10). However, Ub-Rad51 is clearly present following exposure to ionizing radiation when cells were treated with epoxomicin (compare Fig. 4.7C, lanes 11 and 12). Based on the total amount of protein loaded in each lane and scans of the Western blot, we estimate that the amount of Rad51-Ub trapped in the presence of epoxomicin is approximately 2-3 times greater in cells treated with Rad51C siRNA (Fig. 4.7B, lane 8) than in cells not treated with siRNA.

**FIGURE 4.7A/B/C**

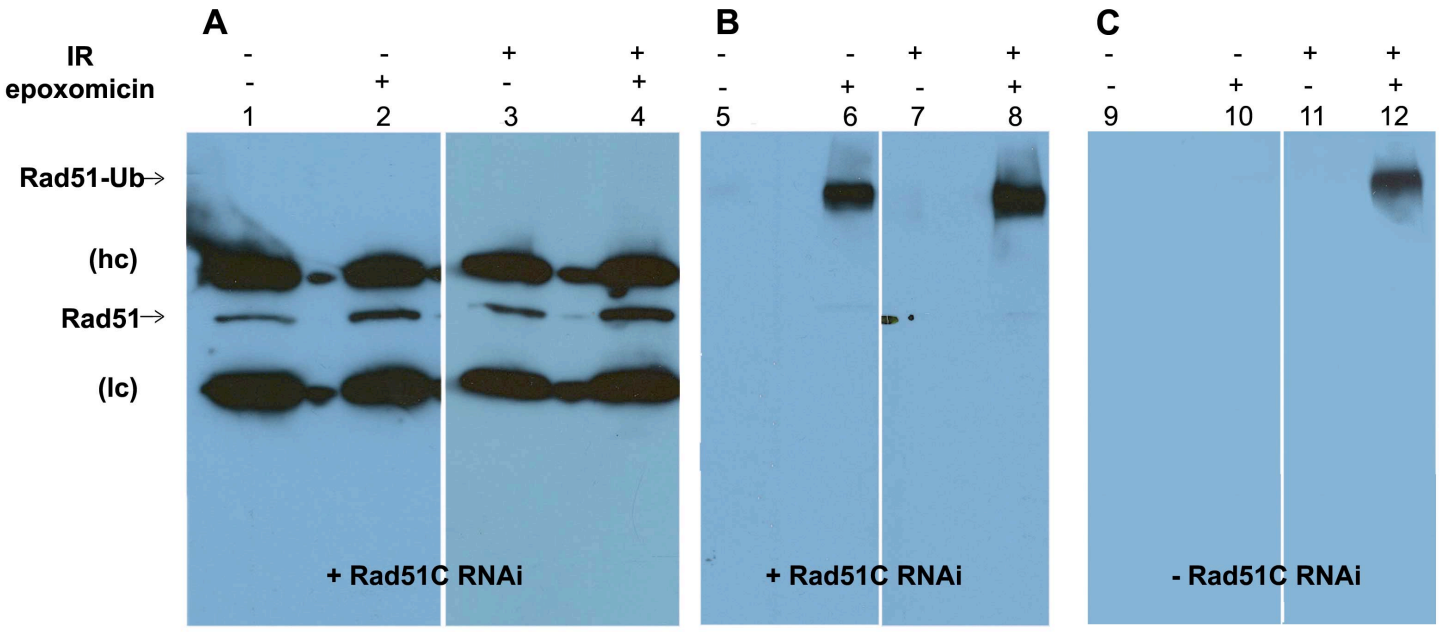


Bennett and Knight Figure 7

**Figure 4.7 - Rad51C regulates ubiquitin-mediated proteasomal degradation of Rad51.** (A) Rad51 was immunoprecipitated from cells that had been treated with Rad51C siRNAs for 48 hr, exposed to ionizing radiation (8 Gy) and subsequently incubated with epoxomicin. The blots were developed with the same antibody used for Rad51 immunoprecipitation, and the heavy and light chains of the monoclonal anti-Rad51 are indicated as (hc) and (lc), respectively. (B) The blots in (A) were stripped and re-probed with anti-ubiquitin. (C) HEK293 cells not treated with siRNA were processed exactly as those in panel (A) and the Western blot was probed with anti-ubiquitin.

(Fig. 4.7C, lane 12). Therefore, while it appears that ubiquitination and proteasomal degradation of Rad51 is a normal part of the DNA repair process, our data also reveal that Rad51C plays an integral role in regulating this effect.

## DISCUSSION

The Rad51C and Xrcc3 proteins have been implicated as having important roles both early and late in the Rad51-catalyzed homologous recombination DNA repair pathway. In this study we have focused on determining the cellular distribution of endogenous Rad51C and Xrcc3, as well as Rad51, over the course of ionizing radiation -induced DNA damage and repair. As has been shown previously, we find that Rad51 forms discrete nuclear foci in response to DNA damage (Haaf et al., 1995; Bishop et al., 1998; Tashiro et al., 2000; Paull et al., 2000; Takata et al., 2001; Tarsounas et al., 2004b). We also show that these foci dissipate as DNA repair finishes, visualized by the disappearance of gamma H2AX foci. In contrast, we find that both Rad51C and Xrcc3 form discrete nuclear foci prior to DNA damage, and that these foci persist throughout the time course of DNA repair. It has been shown that formation of DNA damage-induced nuclear Rad51 foci requires the presence of each of the five Rad51 paralog proteins (Bishop et al., 1998; Takata et al., 2001) and that Xrcc3 nuclear foci form independently of Rad51 (Forget et al., 2004) (this study). We also show here that Rad51C nuclear foci form independently of Rad51. It may be, therefore, that the pre-damage nuclear Rad51C and Xrcc3 foci represent sites of protein function regarding their potential role in assisting the assembly of Rad51 nucleoprotein filaments at the sites of DNA breaks. We note that Rad51C and Xrcc3 can exist as a stable heterodimer (Kurumizaka et al., 2001; Masson 2001a; Wiese et al., 2002), and that the relatively weak interaction between Rad51C and Rad51 is increased in the presence of Xrcc3

(Schild et al., 2000). Alternatively, these foci may represent storage sites that release protein as needed during the DNA repair process. Further studies will be required to define the exact content and functional nature of these foci.

Our immunofluorescence images also show distinct staining for all 3 proteins in the cytoplasm and perinuclear region. Controls presented for antibody specificity using both Western blot and immunofluorescence methods, and the fact that both DAPI and gamma H2AX stains are localized exclusively to the nucleus, makes it unlikely that this results from artifacts in fixation or staining procedures. In fact, we note that other studies have reported a significant amount of Rad51 (Yoshikawa et al., 2000; Davies et al., 2001) and Rad51C (Miller et al., 2005) in the cytoplasm of human cells using Western blot analysis of sub-cellular fractions. It has been previously suggested that because Rad51C has a functional nuclear localization signal it may serve as a transporter for those proteins with which it interacts but lack an nuclear localization signal (French et al., 2003), Rad51 being one of those (Schild et al., 2000). Partial localization of Rad51C at the perinuclear region is consistent with this idea. While studies of BRCA2 provide evidence for its direct participation in nuclear localization of Rad51 (Yuan et al., 1999; Spain et al., 1999; Godthelp et al., 2002; Davies et al., 2001; Tarsounas et al., 2004b), further studies of Rad51C will be required to determine if it also contributes to the nuclear localization of Rad51 and related repair proteins in response to DNA damage.

Given that Rad51C and Xrcc3 form a stable heterodimer (Kurumizaka et al., 2001; Masson 2001a; Wiese et al., 2002) and that Xrcc3 promotes the physical interaction of Rad51C and Rad51 (Schild et al., 2000), an important aspect of this work was to study the interdependence of

the pattern of localization and the response to DNA damage for each protein. As expected, we observed that formation of DNA damage-induced Rad51 foci required the presence of Xrcc3. However, we have made the unexpected observation that RNAi-mediated knockdown of Rad51C leads to decreased levels of Rad51, and that this effect appears to be increased following DNA damage. Our data support the idea that in both cases, depletion of Rad51 results from ubiquitin-mediated proteasomal degradation because in the presence of epoxomicin, a proteasome-specific inhibitor, we observe the accumulation of ubquitinated-Rad51. The fact that the depletion of Rad51 and accumulation of epoxomicin-dependent Ub-Rad51 is significantly greater after cells have been exposed to ionizing radiation suggests that this process is amplified by DNA damage. This is especially apparent in control cells not treated with any siRNAs. In this case we observe no Ub-Rad51 prior to DNA damage, and a level of Ub-Rad51 following DNA damage that is approximately 2-3 fold less than in the absence of Rad51C. These results show that ubiquitination and degradation of Rad51 occur during the normal course of DNA repair, and that Rad51C plays an important role in regulating this process. This effect appears specific to Rad51C because RNAi-mediated knockdown of Xrcc3 does not diminish the level of Rad51 either before or after exposure of cells to DNA damage. Therefore, while a function for Rad51C in nuclear transport and/or loading of Rad51 onto a DNA break may be inferred from available genetic and cellular data, these new results identify a specific function for Rad51C in regulating Rad51 ubiquitination and degradation.

Other studies show that treatment of HeLa cells with Rad51C RNAi results in equivalent loss of both Rad51C and Xrcc3 that extends from 2 to 4 days post-RNAi transfection, while Rad51 levels shows a transient decrease at day 2 followed by recovery at day 3 (Lio et al., 2004). In that

study, cells were not exposed to DNA damage. In contrast, we see no significant decrease of Xrcc3 in cells treated with Rad51C RNAi whether or not cells had been exposed to DNA damage. Because we observed such a dramatic loss of Rad51 in cells treated with Rad51C RNAi that had subsequently been exposed to ionizing radiation and very little effect of Xrcc3 knock down on Rad51 levels, we pursued studies of the mechanism of Rad51C regulation of Rad51 degradation. In ongoing work we are following a more detailed time course and ionizing radiation does dependence of the effect of loss of Rad51C and Xrcc3 on the ubiquitination and degradation of Rad51.

Earlier studies reported a non-covalent association of Ubl1 (SUMO 1) and Ubc9 (a SUMO E2 conjugating enzyme) with human Rad51 as demonstrated by yeast two-hybrid and co-immunoprecipitation experiments (Kovalenko et al., 1996; Shen et al., 1996). Additional studies have shown that in mink cells, treatment with TGF beta leads to ubiquitination and degradation of Rad51 (Kanamoto et al., 2002). In yeast, both components of the 26S proteasome, the 19S regulatory cap and the 20S catalytic core, associate with an HO-induced DSB, and it has been suggested that the proteasome plays a role in DNA repair by clearing proteins following repair (Krogan et al., 2004). The fact that we observe accumulation of Ub-Rad51 in normal HEK293 cells exposed to IR and treated with epoxomicin strongly suggests that proteasome-mediated clearing of DNA repair proteins also occurs in vertebrate cells. Our results also show that when Rad51C is removed from cells, Rad51 ubiquitination and degradation occurs both in the absence of DNA damage and to a greater extent following exposure of cells to ionizing radiation. Therefore, this suggests that proteasome-mediated degradation plays a role in removing Rad51 from breaks following DNA repair and that Rad51C is involved in the regulation of this activity.

We note that BRCA1 has been shown to have E3 ubiquitin ligase activity (Lorick et al., 1999; Hashizume et al., 2001; Ruffner et al., 2001) but specific substrates have yet to be identified. If Rad51 is a BRCA1 E3 ligase substrate, it may be that Rad51C and BRCA1 compete for association with Rad51, and that following DNA repair, Rad51C is signaled to release Rad51 in favor of BRCA1, thereby resulting in ubiquitination and degradation of Rad51. With this link between the ubiquitin-mediated degradation pathway and Rad51C now established, it will be of great interest to understand the relationship between the homologous recombination DNA repair proteins and components of the proteasome pathway to understand how activities are regulated to permit appropriate initiation, catalysis and termination of DSB repair.

## MATERIALS AND METHODS

***Cell lines and Transfections -*** HEK293 cells were obtained from ATCC and were maintained in DMEM supplemented with 10% fetal bovine serum (FBS) and 1% Pen/Strep. In preparation for transfection, cells were maintained in DMEM plus 10%FBS. Transfection of specific siRNA duplexes (*SMART* pool, Dharmacon) was performed using a lipid transfection method (Dharmafect, Dharmacon). A control siRNA against lamin A/C and a 3´-fluorescein labeled control siRNA with no matches in human genome (Qiagen, cat# 1022079) showed no effect on Rad51, Rad51C or Xrcc3 focus formation or protein levels as determined by Western blots (data not shown). Epoxomicin, a specific proteasome inhibitor (Sigma) was added at a final concentration of 5 μM to cells 1 hr prior to exposure of cells to ionizing radiation (IR) for immunoprecipitation experiments (see below).

***Antibodies -*** Primary antibodies were mouse monoclonal anti-phospho-histone H2AX biotin conjugate (clone JBW301, Upstate Biotechnology), mouse monoclonal anti-Rad51 (clone 3C10, Upstate Biotechnology), mouse monoclonal anti-Rad51C (clone 2H11/6, Novus Biologicals, Inc.), mouse monoclonal anti-Xrcc3 (10F1/6, Novus Biologicals, Inc.) and all were diluted 1:500 for immunofluorescence studies. Monoclonal Rad51C and Xrcc3 antibodies were protein-A purified. Alexa647 streptavidin conjugate and Alexa488 secondary antibodies (Molecular Probes) were diluted 1:1000. All dilutions were in PBS containing 20% marine blocking agent (East Coast Biologicals, Inc.). DNA was counterstained with Vectashield Fluorescent Mounting Media containing DAPI (4′, 6′-diamidino-2-phenylindole; Vector Laboratories). Antibodies used for immunofluorescence were the same used for Western blots and immunoprecipitation experiments. Western blot analysis for ubiquitin was performed using rabbit polyclonal anti-ubiquitin (Upstate Biotechnologies) at a 1:500 dilution.

***Immunostaining and Confocal Microscopy -*** Cells were grown on coverslips in a 6 well dish. For fixation, media was aspirated off and cells were washed once with PBS and immersed in 100% methanol at -20 °C for 8 minutes. Cells were blocked in a marine blocking agent overnight at 4 °C. Incubation with primary and secondary antibodies was performed in 6 well dishes for 1 hr at 37 °C in a humid environment using a slide warmer (Fisher). For all double staining procedures, cells were stained in sequential fashion as opposed to using mixes of antibodies. For example, cells were incubated first with the primary antibody directed against Rad51, Rad51C or Xrcc3 followed by incubation with the secondary Alexa488. Subsequently, cells were incubated with anti-gamma H2AX biotin conjugate primary antibody followed by the

secondary Alexa647 streptavidin conjugate. Cells were washed five times for five minutes each in PBS after incubation with both primary and secondary antibodies. Coverslips were mounted using Vectashield with DAPI and sealed with polyurethane (nail polish) then stored in the dark at 4 °C. Visualization of immunostains was performed by confocal microscopy using a Leica TCS SP2 AOBS instrument and image processing was performed using the accompanying Leica Confocal Software TCS SP2. Microscope settings are identical for all images shown. Additionally, all images were corrected to the same values using Leica software. Images were processed and are presented in CMYK colors to avoid loss of resolution during the RGB to CMYK transition.

***Damage-Induced DNA Double Strand Breaks -*** Cells were exposed to 8 Gy ionizing radiation ($^{137}$Cs) using a Gammacell 40 (MDS Nordion Ottawa, ON Canada). After exposure cells were allowed to recover at 37 °C (5% $CO_2$) for the indicated times. Cells were then methanol fixed and prepared for immunostaining.

***Western Blotting -*** HEK293 cells were transfected with the appropriate siRNA as indicated. Cells were harvested 48 hr post transfection washed with PBS and lysed with RIPA buffer (25 mM Tris pH 7.4, 0.5% triton X-100, 0.5% sodium deoxycholate, 0.05% sodium dodecyl sulfate, 0.05 mM EDTA pH 7.0, 75 mM NaCl) and total protein was determined with BCA Protein Assay Kit (Pierce). Acrylamide mini-gels (10%) were run with 60 μg of total protein in each lane and transferred to PVDF membranes using a semi-dry procedure (Bio-rad) at 20 V for 20 min. Membranes were incubated in blocking buffer (10 mM Tris-HCl pH 8.0, 300 mM NaCl, 0.025% Tween 20) containing 15% instant nonfat dry milk for 45 min. Primary antibodies were

added (1:1,000) in blocking buffer containing 2% instant nonfat dry milk for 1 hr. and membranes were washed five times for 5 min each in blocking buffer. Mouse anti-alpha-tubulin (TU-02, Santa Cruz Biotechnology) was diluted 1:10,000. Peroxidase conjugated anti-mouse and anti-rabbit secondary antibodies (Visualizer, Upstate) were added (1:12,000) for 45 min and membranes washed as above. Membranes were incubated with the appropriate chemiluminescent detection reagent for 10 to 60 sec., exposed to X-ray film and developed (Kodak 2000A XOMAT processor). To detect ubiquitinated Rad51, blots that had been stained for Rad51 were incubated in stripping buffer (62.5 mM Tris-HCl, pH 6.0, 2% SDS, 100 mM beta ME) at 50 °C for 30 min, washed twice for 20 min with blocking buffer and stained as above using anti-ubiquitin antibodies.

***Immunoprecipitation -*** Cells were harvested and treated with lysis buffer (20 mM Tris, pH 8.0, 150 mM NaCl, 1 mM EDTA, 0.5% NP-40, 1 mM phenylmethylsulfonyl fluoride, leupeptin [10 µg/ml], aprotinin [10 µg/ml]) for 30 min at 4 °C. Extracts were clarified by centrifugation for 10 min at 12,500 x g. The supernatant was incubated with anti-Rad51 (see above) and 30 µl protein A beads (Amersham) for 2 hr at 4 °C and washed three times using the following buffer (20 mM Tris [pH8.0],150 mM NaCl, 1 mM EDTA, 0.5% NP-40). Beads were boiled in SDS loading buffer and proteins were analyzed by Western blots as described above.

# CHAPTER V

## IMMUNOFLUORESCENT ARTIFACTS DUE TO STAINING METHODS: USE OF ANTIBODY COCKTAILS *VS.* SEQUENTIAL ADDITION ANTIBODIES INFLUENCES THE APPEARANCE OF PROTEIN COLOCALIZATION

## INTRODUCTION

Having felt satisfied that the work described in Chapter IV clearly demonstrated antibody specificity there still remained the issue of colocalization. Phosphorylation of histone H2AX, referred to as gamma H2AX, is commonly used as a marker to indicate the presence of DNA double-strand breaks (Rogakou et al., 1998). Several initial manuscripts studying Rad51 by immunofluorescence showed that DNA damage-induced Rad51 nuclear foci colocalize with gamma H2AX, thereby establishing the dogma that nuclear Rad51 foci represent active sites of ongoing repair at the indicated DNA breaks. In contrast, my immunofluorescence images show no colocalization of these 2 markers. Having already encountered resistance at meetings and on the part of reviewers regarding my images showing significant amounts of cytoplasmic Rad51, Rad51C and Xrcc3, the lack of Rad51 and gamma H2AX colocalization further fueled the anger of some colleagues in the DNA repair field. We also found it curious that apparently, no one had questioned the absence of cytoplasmic Rad51 in published immunofluorescence studies despite the fact that significant levels of cytoplasmic Rad51 had been reported in several manuscripts using cellular fractionation and Western blot methods (Yoshikawa et al., 2000). Therefore, it was important to resolve the discrepancy between our work and that in the literature. Studies in this Chapter address two major conflicts with published work and established dogma. First, if

significant levels and a potentially functionally important pool of Rad51 exists in the cytoplasm, why are we the only ones who see it? And second, why is it that we see little to no colocalization of Rad51 with gamma H2AX following DNA damage, while virtually all published studies show nearly perfect colocalization of these 2 proteins?

The work presented here demonstrates that immunofluorescence methods, specifically the protocol used for application of antibodies to fixed cells, can influence the data obtained.

## RESULTS

To determine whether the method of application of antibodies to fixed cells has a causal relationship to the final staining pattern, we first needed to define various methods of application. We did this by comparing our methods to those described in publications relevant to our field. Upon compiling every paper that had been published showing Rad51 foci it was apparent that very seldom are we provided a clear methodology for immunoassaying, beyond stating that a mix, combination or cocktail was used. Further, these publications provided little to no information as to the particulars of the microscopy such as the uniformity of the settings beyond telling us what microscope was used. I therefore decided to compare our immunofluorescence methods, involving sequential addition of primary and secondary antibodies, to the commonly used procedure of using antibody cocktails (Fig. 5.1). The column labeled “COCKTAIL” (Fig. 5.1) outlines a popular method of immunostaining whereby you have multiple antigen targets and you seek to bind them in one step by mixing the primary antibodies together in an incubation media. This is frequently done when primary antibodies from multiple species are available. In row 1 (MIX – “COCKTAIL”) the cartoon depicts the addition of a mix of primary antibodies

(mouse and rabbit) to fixed cells. For obvious reasons this would not be a preferred method if the primary antibodies were of the same species. Following incubation with this mix, row 2 shows the use of mixed secondary antibodies (fluorophore-conjugated donkey anti-mouse and donkey anti-rabbit). The right column ("Sequential Staining") depicts the alternative method in which fixed cells are incubated with one primary antibody (row 1), washed and incubated with the appropriate secondary antibody (row 2). This is followed by incubation with another primary (row 3) then secondary antibody (row 4). This can be repeated as many times as necessary to target multiple antigens of interest. Note that in the sequential staining method we eliminate the possibility of free primary antigen by quenching with its secondary before adding an additional primary. This is the method we have used for all of our immunofluorescence studies.

While it may seem that the multiple steps used in the sequential staining protocol are time consuming and unnecessary, especially given that the 2 primary antibodies are from different species, the data I show below clearly demonstrate that for some proteins the use of antibody cocktails can lead to artifactual staining patterns and in the case of Rad51 and gamma H2AX has led to inaccurate reports of protein colocalization.

**FIGURE 5.1**

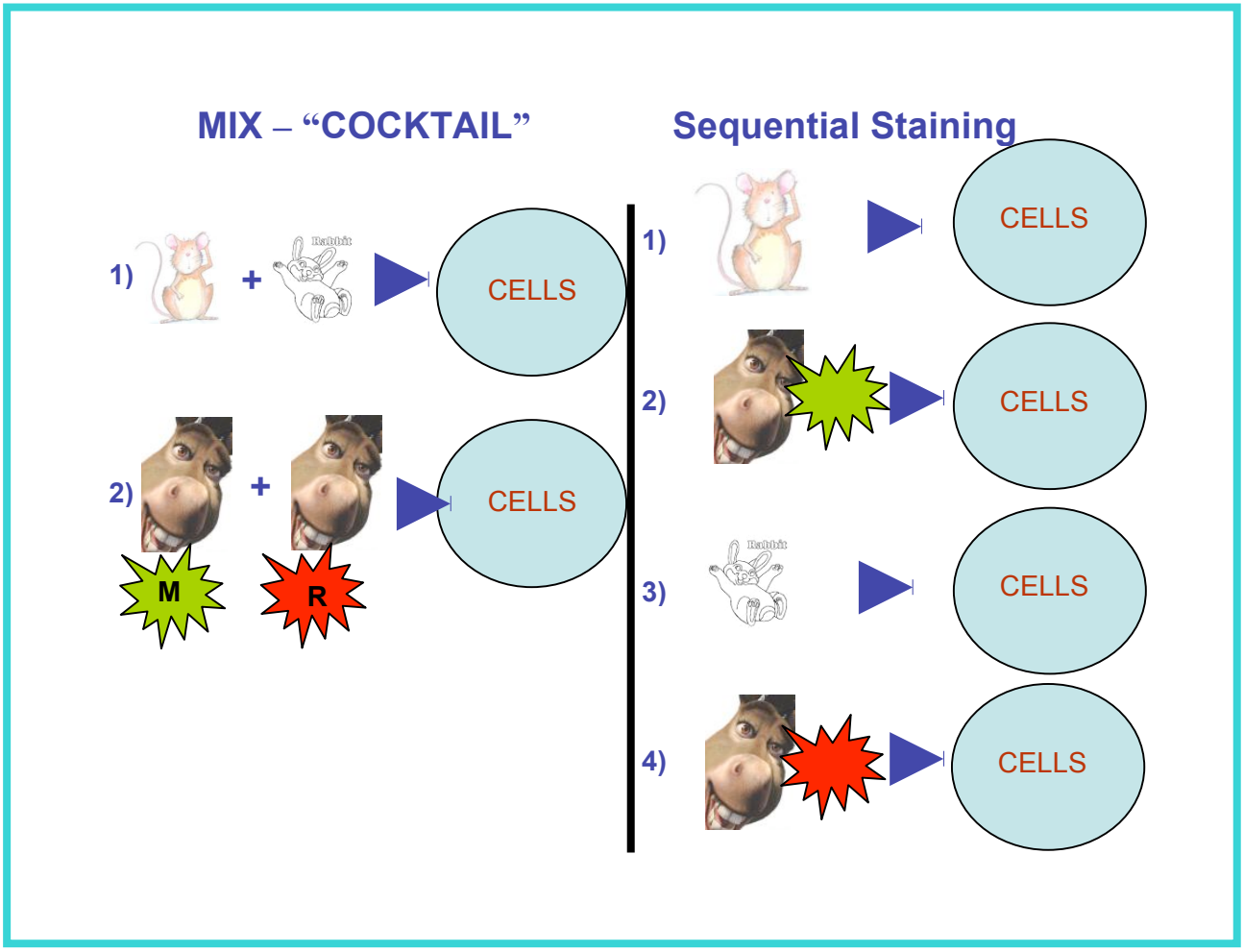
MIX – "COCKTAIL"
Sequential Staining
1)
+
CELLS
2)
+
M
R
CELLS
1)
CELLS
2)
CELLS
3)
CELLS
4)
CELLS

**Figure 5.1 – Sequential staining method vs. cocktail staining.** Column heading "cocktail" describes in row 1 that in this particular application of mixing antibodies addition of multiple primaries, even of different species are mixed together in a incubation media and then added to the cells to bind their appropriate targets. Row 2, same column shows that following incubation, fluorophores conjugated secondary antibodies are added to an incubation media and combined with the cells to find and bind their appropriate primary. Column heading "sequential staining" describes the addition of one primary to one antigen, followed in row 2 by its appropriate secondary; this is then followed by any additional primary and secondary antibodies we chose.

**Mixing primary antibodies directed against Rad51 and gamma H2AX gives false colocalization following DNA damage**

Several publications showing colocalization of Rad51 and gamma H2AX state or imply that antibody cocktails were used to stain cells. To test how the 2 methods described in Figure 5.1 compare when visualizing these 2 proteins we performed several experiments. HEK293 cells were grown, damaged, and fixed as previously described in Chapters II and IV. The primary antibodies used in Figure 5.2 were a purified rabbit polyclonal against Rad51 and a purified mouse monoclonal antibody against gamma H2AX. Secondary antibodies were a highly cross-adsorbed donkey anti-rabbit Alexa488 conjugate and a highly cross-adsorbed donkey anti-mouse Alexa647. From left to right in both rows A and B, the panels show (1) DAPI stain to indicate the nucleus, (2) Rad51 in green, (3) gamma H2AX in red and (4) a merge of the green and red channels (overlay). The merge depicts events of coincidence or more popularly, and incorrectly, termed colocalization. DAPI was not included in the merge of the green and red channels as it convolutes the data. Row A shows the results of using the antibody "cocktail" method, in which the primary antibodies are applied as a mix, followed by application of the secondary antibodies as a mix. The overlay in row A shows very high, if not complete, coincidence of Rad51 and gamma H2AX. Additionally, there is a complete absence of Rad51 from the cytoplasm. This result is very similar to most reports in the literature. Row B shows the results when using the sequential staining procedure. Here the overlay shows virtually no coincidence of Rad51 and gamma H2AX. Additionally, images in row B show a robust cytoplasmic Rad51 signal. It is important to note that the microscope settings in both sets of data, rows A and B, were identical. The DAPI channel appears less intense in row A due to an error in conversion of file type

following data collection; however this does not affect the localization of the other stains. Virtually identical results were obtained using different primary and secondary antibodies, in this case a purified mouse monoclonal against Rad51 and a purified rabbit polyclonal against gamma H2AX (Fig. 5.3). Again, almost complete coincidence of the signals in the nucleus, and the absence of cytoplasmic Rad51, was observed using antibody cocktails, whereas little coincidence of the nuclear signals and robust cytoplasmic Rad51 staining was observed using sequential staining. Further, it is worth mentioning that the 488 and 647 nm fluorophores have no overlap and eliminate the possibility of bleed through. Additionally, these were sequential scans requiring that only one laser line be active at any given time, eliminating bleed from channel to channel. Finally the Leica TCS SP2 confocal microscope has tunable photomultiplier tubes rendering bleed impossible by elimination of overlapping spectra. In the next set of experiments we stained HEK293 cells using only Rad51 antibodies. This was done to verify the cellular localization of Rad51 on its own by eliminating the unlikely but finite possibility that other antibodies may affect its immunofluorescence pattern when applied using the sequential staining method.

**FIGURE 5.2**

**Cocktail – primary mix followed by secondary mix**

**A**

**DAPI** **Rad51 polyclonal** **γH2AX monoclonal** **overlay**

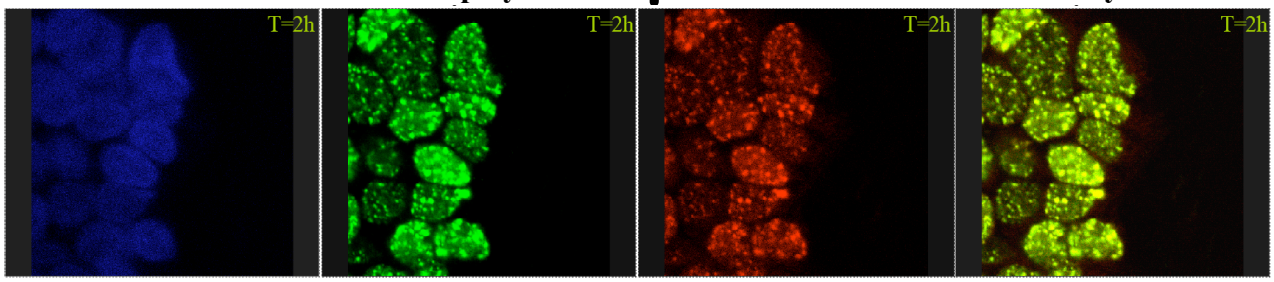


**Sequential staining – 1st primary/1st secondary followed by 2nd primary/2nd secondary**

**B**

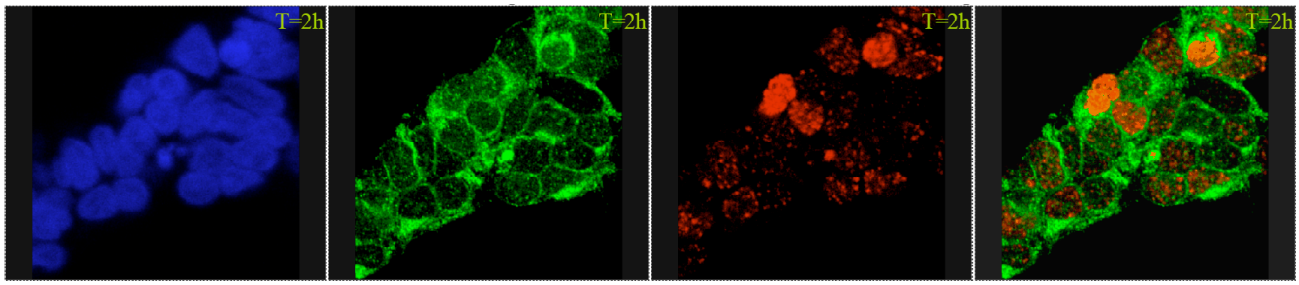

**Figure 5.2 - Mixing primary antibodies directed against Rad51 and gamma H2AX gives false colocalization following DNA damage.** HEK293 cells were sustained on glass coverslips, damaged with ionizing radiation (8 Gy) and then methanol fixed two hours after damage. Cells were immunostained using either the cocktail method (row A) or the sequential method (row B). Rows A and B left hand image is the nuclear stain DAPI. The next column of images is staining for Rad51 (green) followed by gamma H2AX (red) with the last column being the merge or overlay of the previous two columns, green and red. Antibodies used were purified rabbit polyclonal (Rad51) and purified mouse monoclonal (gamma H2AX).

**FIGURE 5.3**

**Cocktail – primary mix followed by secondary mix**

**A**

**DAPI** **Rad51 monoclonal** **γH2AX polyclonal** **overlay**

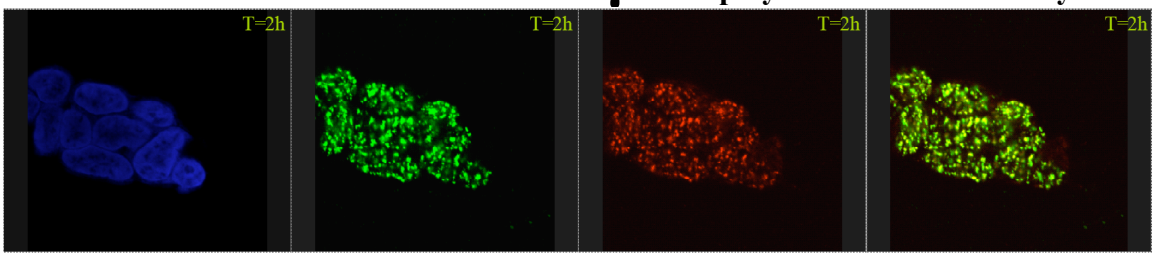


**Sequential staining – 1st primary/1st secondary followed by 2nd primary/2nd secondary**

**B**

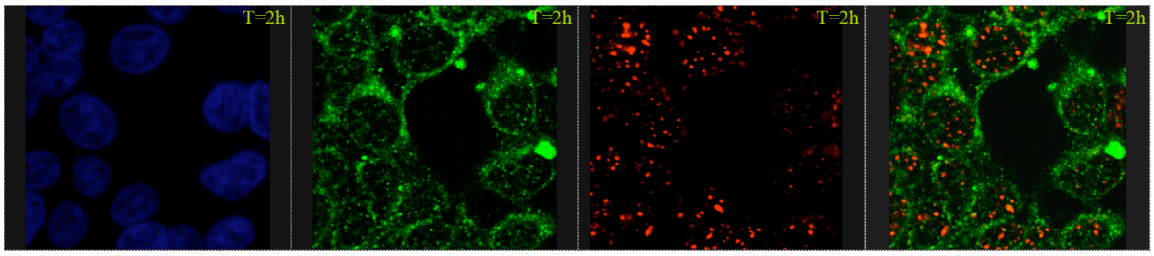

**Figure 5.3 - Mixing primary antibodies directed against Rad51 and gamma H2AX gives false colocalization following DNA damage.** As described for Figure 5.2, except the antibodies used were a purified mouse monoclonal (Rad51) and purified rabbit polyclonal (gamma H2AX).

**Rad51 shows significant a immunofluorescence signal in both the nuclear and cytoplasmic compartments.**

Bearing in mind that any primary antibody we use has gone through our purification system (Chapter III) and further, that we have done all proper controls to ensure specificity (Chapter IV), staining against Rad51 alone in HEK293 cells under the same conditions as described above should precisely reveal Rad51's localization. Additionally, it had been suggested that the methanol fixation method used in our system could be the cause of differences seen between our staining pattern for Rad51 vs. those commonly seen in the literature. Therefore, we tested various conventional fixation methods, e.g. 4% paraformaldehyde, and the result was the same for all (data not shown). In Figure 5.4 we show staining of HEK293 cells 2 hr post DNA damage (8 Gy ionizing radiation) using a purified polyclonal rabbit antibody against Rad51. The secondary antibody was a highly cross absorbed donkey anti rabbit Alexa 488 conjugate. These images show that Rad51 stains throughout the entire cell with distinct DNA damage-induced nuclear foci (red arrow) as well as a robust cytoplasmic signal (green arrow). Additionally, not only do we see Rad51 staining in the cytoplasm both before and after damage we have observed dynamic changes in its localization pattern as a function of time after DNA damage that is very reproducible (Chapter IV). However the regulation and functional consequence of these changes are currently undefined. Our initial work towards addressing these issues is described in Chapter VI.

**FIGURE 5.4**

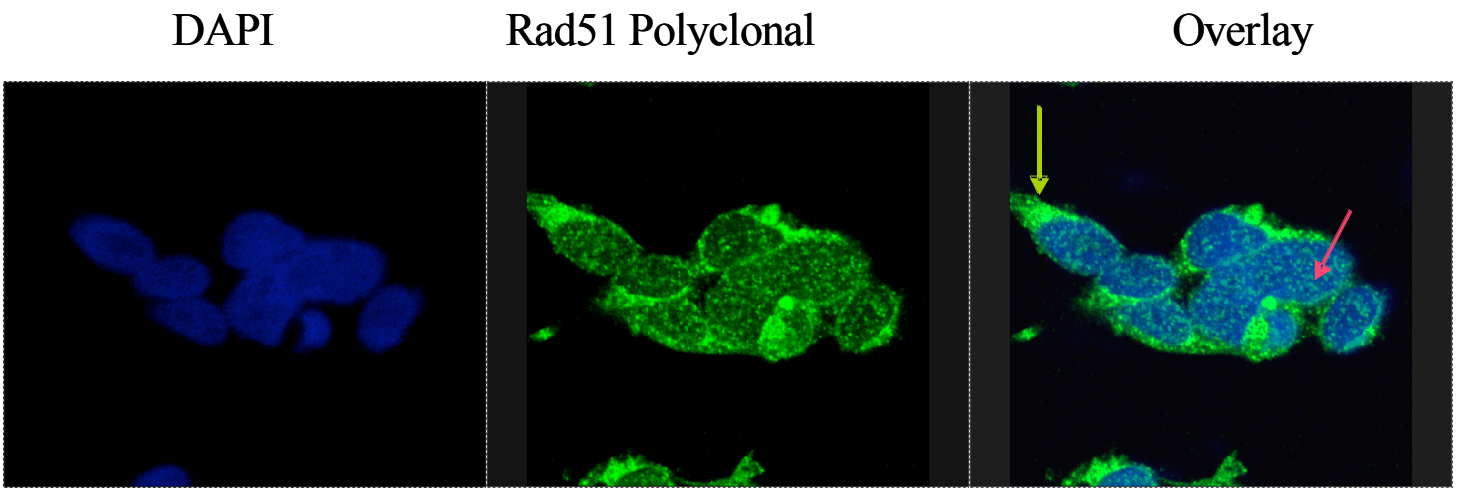


Green arrow denotes cytoplasmic staining

Red arrow shows nuclear staining

**Figure 5.4 - Rad51 occupies both nuclear and cytoplasmic compartments following DNA damage.** HEK293 cells were sustained on glass coverslips, damaged with 8Gys of ionizing radiation and then alcohol fixed two hours after damage. Far left image is DAPI stained for the nucleus. The middle figure is stained for Rad51 (green) with the far left image being the overlay. Green arrow indicates cytoplasmic staining for Rad51 while the red arrow shows nuclear staining.

Finally, it appears that while there is no credible knowledge to date as to what a protein "focus" is, there is clearly Rad51 focus development in the cytoplasm of the cell. To investigate the mechanism by which staining of gamma H2AX skews the appearance of Rad51 staining, we performed experiments in the next section.

**Competitive binding assays show that staining for gamma H2AX negatively influences staining of Rad51.**

Experiments in the next two sections address the possibility that staining of gamma H2AX somehow influences the staining of Rad51. Our thought was that the possible extreme excess of gamma H2AX antigen following DNA damage relative to the amount of Rad51 antigen causes the artificial appearance of co-localization of these two proteins. First, we performed an experiment in which the primary antibodies against gamma H2AX and Rad51 are derived from the same species, either 2 mouse monoclonals or 2 rabbit polyclonals. Therefore, while the secondary antibody could not distinguish between the 2 primary antibodies, we should still see nuclear staining representing a combination of gamma H2AX and Rad51, as well as the cytoplasmic staining of Rad51 that we have observed and verified many times. HEK293 cells were grown, damaged and prepared for staining as described previously. Figure 5.5 shows images of cells stained sequentially with mouse monoclonal or rabbit polyclonal antibodies (rows A and B, respectively) followed by application of the appropriate secondary antibody Alexa 488 conjugate. We find that the Alexa 488 signal is localized exclusively to the nucleus, with no hint of cytoplasmic signal. This result looks virtually identical to that in Figures 5.2 and 5.3 in which antibody cocktails were used. Additionally, it mimics the staining pattern that we see for gamma H2AX alone (Forget et al., 2004; Bennett and Knight, 2005). It appears,

therefore, that given the opportunity to bind either target the secondary only sees and binds the gamma H2AX primary antibody. That is not to say that some of the nuclear signal does not represent Rad51, but if this is true, how can we explain the lack of signal in the cytoplasmic compartment? This result suggests that what we are seeing is competition for binding of the secondary antibody created by the overwhelming epitope availability of gamma H2AX and, therefore, an extreme excess of the primary antibody against gamma H2AX. We were left with a simple query. If the epitope availability of gamma H2AX is out-competing Rad51, then it stands to reason that we should recover Rad51 signal if we were to reduce the gamma H2AX availability. This is addressed in the next section.

**FIGURE 5.5**

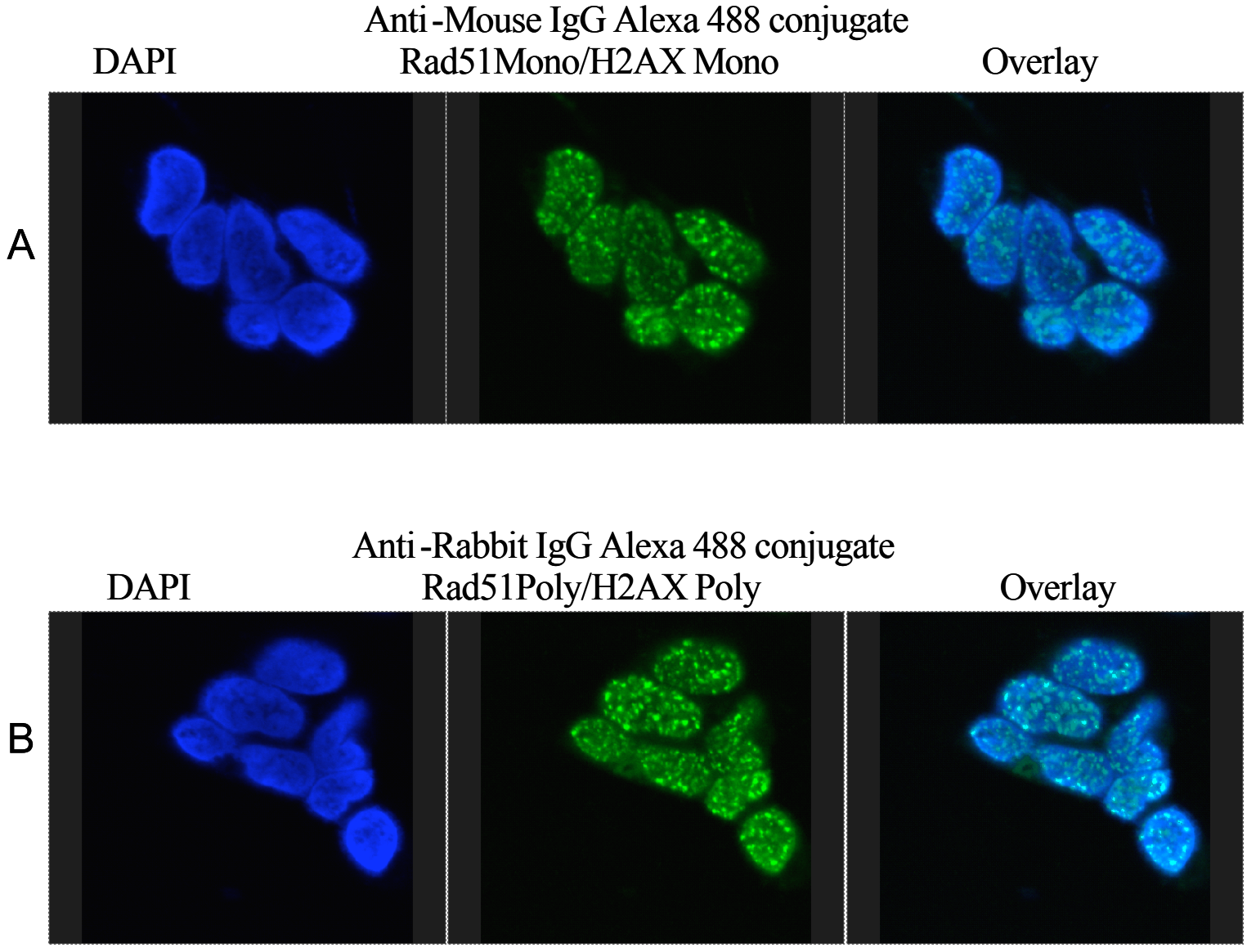
Anti-Mouse IgG Alexa 488 conjugate
DAPI
Rad51Mono/H2AX Mono
Overlay
A
Anti-Rabbit IgG Alexa 488 conjugate
DAPI
Rad51Poly/H2AX Poly
Overlay
B

**Figure 5.5 - Gamma H2AX staining influences secondary antibodies in competitive binding assay.** HEK293 cells were sustained on glass coverslips, damaged with 8Gys of ionizing radiation and then alcohol fixed two hours after damage. Rows A and B cells were DAPI (blue) was used to counterstain nucleus. Row A, middle column, cells were stained sequentially with monoclonal antibodies against both Rad51 and gamma H2AX followed by an anti mouse Alexa 488 conjugate (green). Row B, middle column, cells were stained sequentially with polyclonal antibodies against both Rad51 and gamma H2AX followed by an anti rabbit Alexa 488 conjugate (green). Far left column rows A and B are the merge of the two channels, DAPI and Alexa 488.

**Reduction of epitope availability for gamma H2AX reduces competition for binding by secondary antibodies and recovers Rad51staining.**

I performed the following experiment to directly test the idea that excess epitope availability of gamma H2AX relative to Rad51 results in loss, or at least minimization, of Rad51 staining. The hypothesis was that by reducing the amount of gamma H2AX primary antibody while keeping the amount Rad51 antibody constant we should see recovery of Rad51 signal, and hence cytoplasmic signal.

In Figure 5.6, I show that titration of the primary antibody against gamma H2AX from the standard 1:1,000 dilution used in the literature (top row = 1:1,000 dilution; middle row = 1:10,000; lower row = 1:50,000 dilution), while maintaining the Rad51 antibody at a constant 1:1,000 dilution, demonstrates a titration-dependent increase in cytoplasmic signal. Identification of nuclei by DAPI staining clearly indicates recovery of cytoplasmic signal as the gamma H2AX antibody is diluted. Given that gamma H2AX is exclusively nuclear, we conclude that the cytoplasmic signal is Rad51. Again, we have verified this Rad51 localization pattern previously by RNAi knock down of Rad51 (Forget et al., 2004; Bennett and Knight, 2005). Also, it is important to note that we stained for gamma H2AX on its own to ensure that at both 1:10,000 and 1:50,000 dilutions we had sufficient antibody to produce signal (not shown). I also performed similar "cocktail" *vs*. "sequential" staining experiments using primary antibodies for Rad51C, Xrcc3, Mre11 and Rad50 and all displayed exactly the same result. Not surprisingly when these experiments were conducted using antibodies directed against

**FIGURE 5.6**

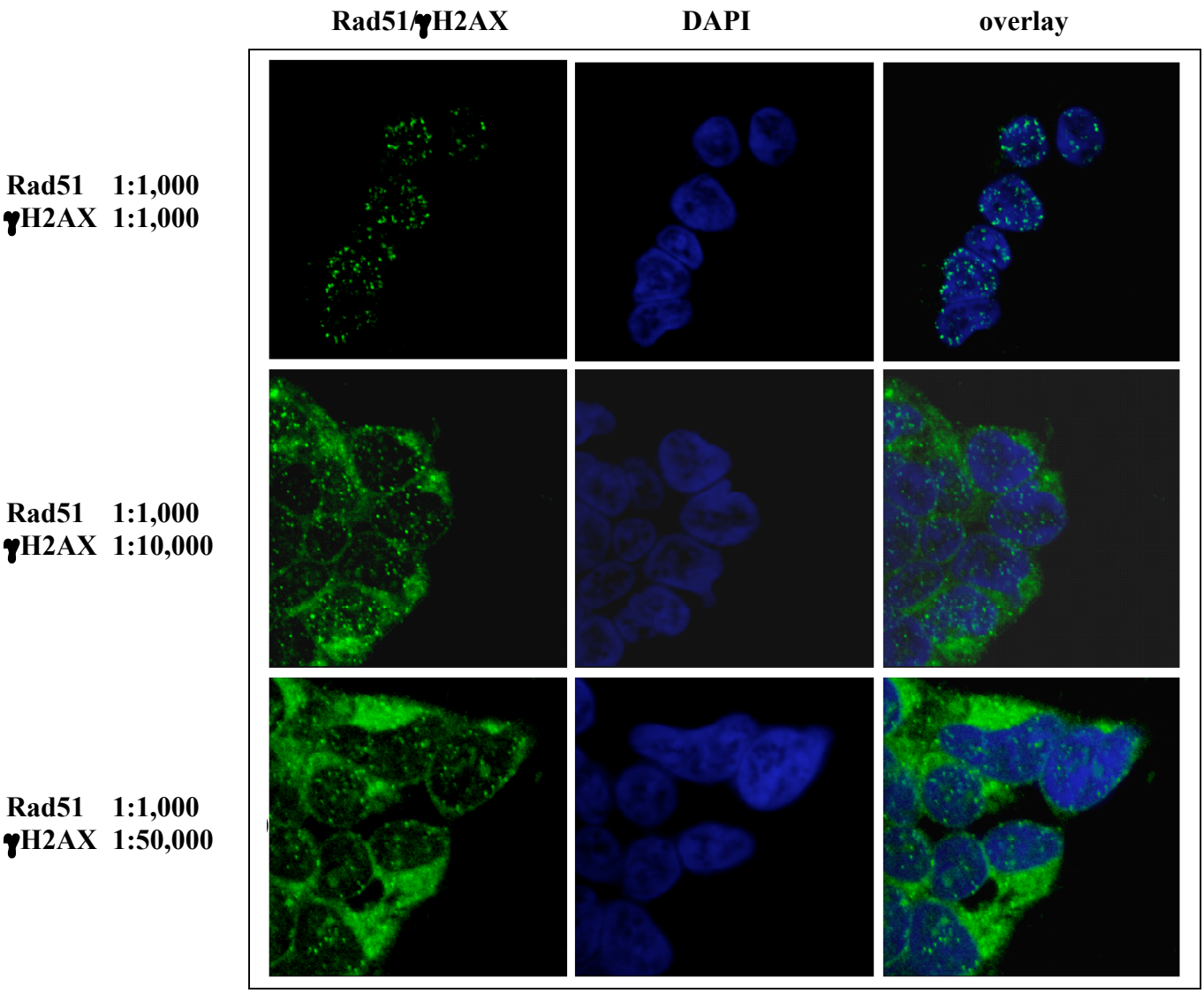
Rad51/γH2AX
DAPI
overlay
Rad51 1:1,000
γH2AX 1:1,000
Rad51 1:1,000
γH2AX 1:10,000
Rad51 1:1,000
γH2AX 1:50,000

**Figure 5.6 - Reduction of epitope availability for gamma H2AX reduces competition for binding by secondary fluorophores and recovers Rad51 staining.** HEK293 cells were sustained on glass coverslips, damaged with 8Gys of ionizing radiation and then methanol fixed two hours after damage. Moving from left to right the right hand column represents staining with primary antibodies against both Rad51 and gamma H2AX (green) with the concentration of gamma H2AX directed primary decreasing as denoted to the left of each panel moving from top to bottom. The middle column is stained with DAPI against the nuclear compartment. The final column on the far left represents the merge of both the green channels and the blue. Microscope setting in this images remained constant throughout.

ATM, a large and abundant protein primarily responsible for the phosphorylation of gamma H2AX, we did not see these result (not shown).

From these studies we conclude that for certain proteins, when antibodies are mixed as cocktails, there is a clear danger in masking the signal of the one for which the epitope is in relatively lower abundance. While it is commonly assumed that the use of antibodies from different species avoids such concerns, we clearly demonstrate that it remains a problem for certain proteins. This is especially true in the DNA repair field in that many papers used such methods to conclude that nuclear Rad51 foci colocalize with gamma H2AX at the site of a DNA double strand break, with the extended conclusion that this represents active Rad51 nucleoprotein filaments that are engaged in DNA strand exchange as they repair the break. Given these results, we feel it is important to provide controls in published manuscripts validating the specificity of the antibody, and regardless of the species from which antibodies are derived, authors should also provide evidence that if a cocktail is used that each antibody behaves as when it is used individually. However, a sequential staining protocol is clearly preferable.

# DISCUSSION

At the beginning of this work it was apparent that one of the shortcomings in the DNA repair field was the lack of consistent and well-controlled immunofluorescent data for Rad51 and especially the Rad51 paralog proteins. The use of vectors expressing fluorescent fusion proteins proved to be problematic in controlling expression levels and I found that this led to artifactual development of Rad51 foci independent of DNA damage. Additionally, there was no unambiguous information available that described exactly what a protein focus was. In Chapters II through V the progression of understanding as to protein localization and focus development proceeded coincidentally with our ability to create and optimize effective reagents and protocols for immunostaining.

We have now provided the first demonstration using immunofluorescence methods that Rad51 has a significant presence in the cytoplasm. Most importantly, our studies reveal previously unavailable detail regarding the dynamic re-localization of Rad51, Rad51C and Xrcc3 in response to DNA damage (Chapter IV). In large part, this is due to our investigation of every caveat of our immunofluorescence methods from fixation, blocking buffers, varying radiation doses, best possible microscope and evaluation of its parameters, and even the type of glass we use to grow the cells on. Finally, from the work in this Chapter we are convinced that the numerous published images showing Rad51 as exclusively nuclear and perfectly colocalized with gamma H2AX appear to be an artifact of the methods used for antibody application. In fact, a recent study by Schroff *et al*. (2004) showed that gamma H2AX existed over a 50 kb area surrounding a DNA break and that little is found within 1 – 2 kb of the break.

Given the rigors of our protocol we now feel confident in addressing more complex questions regarding possible protein-protein interactions that occur both before and after DNA damage, and how trafficking of proteins involved in homologous recombinational DNA repair between different sub-cellular compartments is regulated in response to DNA damage. Work presented in the next Chapter (VI) represents our initial efforts to combine immunofluorescent and biochemical methods, e.g. Western blots of sub-cellular fractions, to study the time-dependent movement of repair proteins throughout the cell in response to DNA damage. In fact, we find that our biochemical experiments lend strong support to our published immunofluorescence work. There is clearly a significant amount of Rad51 in the cytoplasm both before and after DNA damage, and the DNA damage-induced changes we observe by immunofluorescence for Rad51 are now corroborated by Western blots of sub-cellular fractions (cytoplasm, nucleoplasm and chromatin-associated) as a function of time following DNA damage (see Chapter VI).

While much of the current data in the DNA repair field on protein localization lack proper controls, problems extend beyond antibody specificity and the method of application. In all the work presented herein I have available the "footprint" to each image, or, a record of all the microscope settings used when acquiring the data i.e. zoom factor, resolution, field dimension, PMT voltage, pinhole airy units etc., (not shown). At this time, no journal requires this information, nor have we been asked for it by reviewers or journals. Yet, dramatically different images can result from even the slightest adjustment to these settings. Therefore, in all cases where I present direct comparison of different proteins in the same or different images, all microscope settings are kept constant. If claims of protein colocalization are made, one must

consider and describe the method of data collection. As another example of a methodological issue that contributes to data misinterpretation, wide field microscopy is frequently used in studies claiming protein colocalization. However, wide field imaging captures all signal throughout the stained sample, thereby allowing us to easily colocalize anything we choose, as we are overlapping signal from different spatial plains within the cell. Confocal microscopy does not, in a single slice, confirm colocalization either. The average theoretical resolution of confocal microscopes is approximately 200 nm while the actual resolution is often between 300 – 400 nm or greater. At this resolution in a single plain you still have a large margin for error in claiming that overlapping signal from two fluorophores represents colocalization. What is required for the claim of colocalization are X, Y, and Z (X, Z, Y is also a good way to demonstrate this) scans at the best possible resolution, sequential scanning to reduce cross talk between fluorophores, and a Z stack that gives the optimal amount of steps needed to acquire the maximal special detail, and of course the same setting for each channel, zoom factor, etc. Only once these data are collected, processed and made into a 3 dimensional image that can be rotated can we begin to discuss the various signals that represent proteins sharing space. Implications that proteins may be interacting can also be corroborated using methods such as FRET, FLIM, or a new technology, 4Pi microscopy (I describe our initial use of 4Pi in Chapter VII).

In conclusion, I propose that journals consider the inclusion of more careful controls for all aspects of immunofluorescence work, from validation of antibody specificity, to the method of antibody staining, to the collection of microscope images as well as the processing of data.

## PREFACE TO CHAPTER VI

The work in Chapter VI continues our investigation of Rad51 focus formation and its dependency on the Rad51 paralogs, Rad51C and Xrcc3. In addition, we begin investigation of Brca2, a breast cancer related gene product. It has been shown that Brca2 is involved not only in transport of Rad51 to the nucleus following DNA damage but also Rad51 nuclear focal development. Our intention was to investigate if Rad51, though not able to form foci in the absence of a functional Brca2 protein, was in fact still able to gain access to the nucleus. This work also provides the first investigations into the potential relationship that Brca2 may have with Rad51C and Xrcc3. The work presented herein provides new data showing that increased amounts of nuclear of Rad51 in response to DNA damage are found in the absence of a functional Brca2 protein. Further, we show that although a non-functional Brca2 protein has a minimal affect on Rad51C localization and nuclear focus formation, there is a pronounced affect on the localization of Xrcc3 including blocking its ability to enter the nucleus.

My specific contributions to this work were the development of the immunofluorescent methods. Dr. Otto Gildemeister performed all Western blot analysis and sub-cellular fraction. Hypothesis development, experimental design, and interpretation of the data were shared between myself, Dr. Gildemeister and Dr. Knight.

# CHAPTER VI

## Translocation of Rad51 to the Nucleus in Response to DNA Damage in Capan-1 Cells

## ABSTRACT

The Rad51 paralog proteins Rad51C and Xrcc3 interact with the Rad51 recombinase and are required for formation of nuclear Rad51 foci in response to DNA damage, properties that are shared with the Brca2 tumor suppressor protein. Earlier studies have also shown that both Rad51C and Xrcc3 exist in nuclear foci both before and following exposure of cells to DNA damage. In this study we use the Brca2 defective pancreatic epithelial tumor cell line, Capan-1, to address possible effects that this defect may have on the localization of Rad51C and Xrcc3, as well as how this Brca2 mutant may affect nuclear entry of Rad51 in response to DNA damage. While our results agree with the previously reported defect in the DNA damage-induced formation of Rad51 nuclear foci, we also find that Capan-1 nuclei show no Xrcc3 nuclear foci as well as a significantly reduced level of nuclear Xrcc3protein. However, Rad51C shows nuclear foci similar to those in $Brca2^{+/+}$ cells although at a diminished level. Therefore, these data support the idea that there is a Brca2-independent pathway for nuclear entry of Rad51 in response to DNA damage, and unexpectedly that nuclear localization of Xrcc3 is dependent on Brca2.

# INTRODUCTION

The human Rad51 recombinase is the central catalytic component of homologous recombinational DNA repair. In cycling cells that have not been exposed to DNA damage, small amounts of nuclear Rad51 appear in foci that have been termed S-phase foci. These are thought to represent pools of Rad51 involved in recombinational repair of arrested or broken replication forks (Tashiro et al., 2000; Golub et al., 1998; Haaf et al., 1999). However, following exposure to DNA damage and induction of double strand breaks there is a significant increase in nuclear Rad51 foci. Formation of these damage-induced Rad51 foci fails to occur in cells defective for Brca2 (Yuan et al., 1999; Godthelp et al., 2002; Tarsounas et al., 2003). Given that Brca2 interacts directly with multiple subunits of Rad51, it has been suggested that Brca2 is responsible for nuclear transport of Rad51 in response to DNA damage (Davies et al., 2001; Pellegrini et al., 2002). Additionally, S-phase Rad51 foci persist in a Brca2 defective cell line thereby suggesting that a Brca2-independent mechanism must exist for nuclear transport of Rad51 and S-phase foci formation under non-DNA damage conditions (Tarsounas et al., 2003).

Our recent immunofluorescence studies show a distinct and reproducible shift in the cellular localization of Rad51 following exposure to DNA damage (Bennett and Knight, 2005) (see Chapter IV). We find that the increase in Rad51 nuclear foci beginning at 30 min following exposure to ionizing radiation is accompanied by a noticeable clustering of Rad51 near the perinuclear region early after DNA damage, and a return to pre-damage localization toward the latter stages of repair. These studies also showed the first localization patterns for the

endogenous Rad51 paralog proteins, Rad51C and Xrcc3. Each protein forms discrete nuclear foci in both the absence and presence of DNA damage, and also shows a significant presence in the cytoplasm. The images also revealed that Rad51C and Xrcc3 do not show the significant change in cellular distribution in response to DNA damage as observed for Rad51.

Earlier studies demonstrated that formation of DNA damage-induced nuclear Rad51 foci depends on each of the 5 Rad51 paralog proteins, Rad51B, Rad51C, Rad51D, Xrcc2 and Xrcc3 (Bishop et al., 1998; Takata et al., 2001; Yoshihara et al., 2004). Rad51C and Xrcc3 can exist as a stable heterodimeric complex (Kurumizaka et al., 2001; Masson et al., 2001a; Wiese et al., 2002) and both proteins are the only Rad51 paralogs that interact directly with Rad51 (Schild et al., 2000).

To further address questions regarding the occurrence, mechanism and regulation of DNA damage-induced re-distribution of Rad51 we have used sub-cellular fractionation and Western blot procedures together with immunofluorescence to study the cellular localization of Rad51, Rad51C and Xrcc3 in several human cell lines, including Capan-1 cells which carry a non-functional Brca2 protein. Our results suggest that the DNA damage-induced increase in nuclear Rad51 levels involves the translocation of existing pools of Rad51 as well as newly synthesized protein. Additionally, we show that some of the DNA damage-dependent movement of Rad51 into the nucleus occurs independent of Brca2.

# RESULTS

## DNA damage induces changes in sub-cellular localization of Rad51.

To compare the localization of endogenous Rad51 before and following exposure to ionizing radiation we examined 3 different human cell lines by sub-cellular fractionation. HEK293, HeLa and HCT116 cells were exposed to ionizing radiation (6 Gy) and harvested 2 hours later. Figure 6.1 shows that in all 3 cell types there is a significant amount of Rad51 present in the cytoplasmic fraction prior to DNA damage (IR -), with lesser amounts present in the nucleoplasm and chromatin-associated fractions. prior to the induction of double-strand breaks.

Following exposure to ionizing radiation there is a noticeable decrease in cytoplasmic Rad51 in HEK293 and HCT116 cells, but this is less obvious in HeLa cells. However, all 3 lines show a distinct increase in nuclear Rad51 as well as chromatin-associated protein. The chromatin fraction was verified by staining for histone H3 (not shown). While several groups have shown previously that Rad51 can be detected by Western blot analysis in the cytoplasmic fraction of various cell lines (Yoshikawa et al., 2000; Davies et al., 2001; Essers et al., 2002; Kraakman-van der Zwet et al., 2002; Tarsounas et al., 2003) this is the first examination of how Rad51 levels in sub-cellular compartments change in response to DNA damage. It is our hypothesis that the cytoplasmic decrease and nuclear increase in Rad51 levels represent active transport of Rad51 following exposure to a DNA damaging agent. We next sought to test whether this increase in nuclear and chromatin-associated Rad51 protein required newly synthesized protein.

FIGURE 6.1

**Re-distribution of cellular Rad51 in response to ionizing radiation**

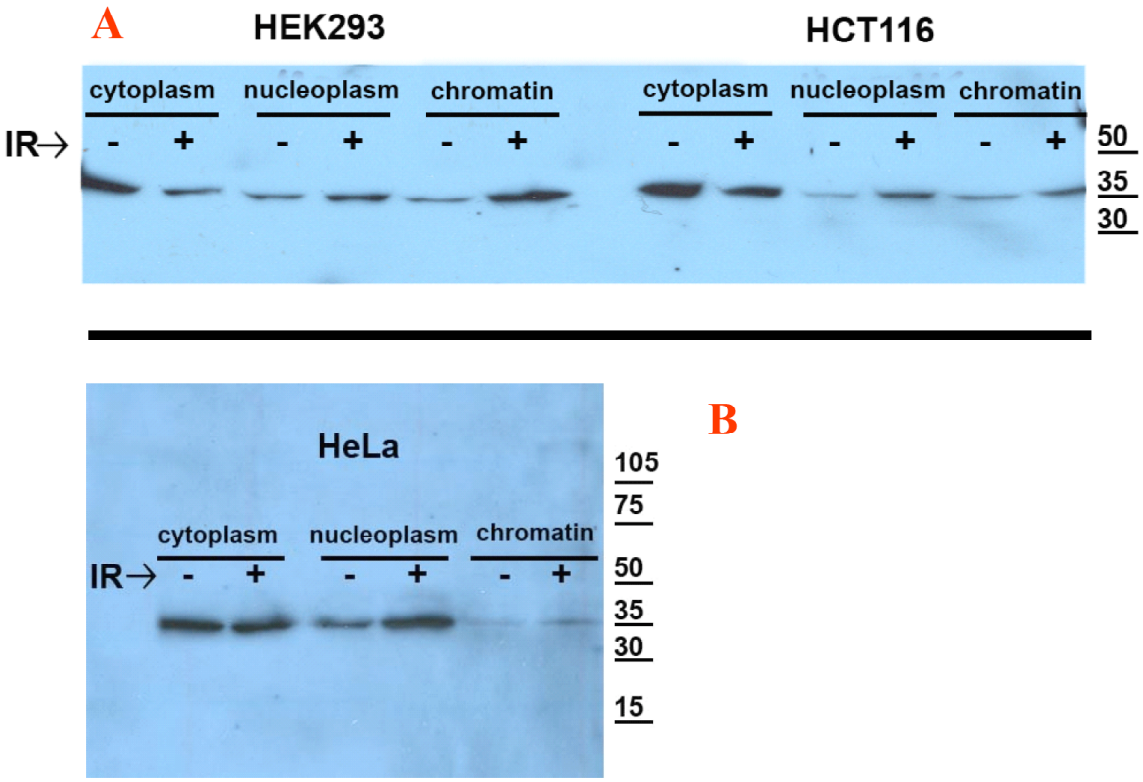

**Figure 6.1 – Re-distribution of sub-cellular HsRad51 in response to ionizing radiation.** Panels A and B, HEK293, HCT 116 cells and HeLa cells (respectively) were assayed by sub-cellular fractionation for endogenous Rad51 in the cytoplasmic, nuclear and chromatin associated fractions in the absence and presence of ionizing radiation.

**DNA damage-induced transport to the nucleus involves existing pools of Rad51 and newly synthesized protein.**

HeLa and HCT116 cells were exposed to ionizing radiation (6 Gy) and collected at 15, 30, 60 and 120 min following damage (a non damage control also collected). An additional set of samples were treated with cycloheximide (20 μM) 1 hr prior to exposure with ionizing radiation, and collected at the same time points. In the absence of cycloheximide, both HeLa and HCT116 cells show a relatively more Rad51 in the cytoplasm before DNA damage and at 15 and 30 min following damage. In HeLa cells there is a decrease in cytoplasmic Rad51 after 30 min following damage, while this decrease is lesso bvious in HCT116 cells (Fig. 6.2A). However, both cell lines show a dramatic increase in nuclear Rad51 60 min following damage. When cycloheximide is added to cells prior to ionizing radiation exposure there is an observable drop in cytoplasmic and nuclear Rad51 in both cell lines. However, we still observe an increase in nuclear Rad51 at the 60 min time point in HCT116 cells whereas this is most obvious at 120 min in HeLa cells. This difference in timing of the increase in nuclear Rad51 may simply be due to the different cell types used or the fact that asynchronous cultures were used in these experiments. Future work will include analysis of synchronized cultures and further, how Rad51 localization may be affected by DNA damage checkpoints. Our results indicate that the changes in sub-cellular localization of Rad51 following DNA damage (Figure 6.1) involve active transport of existing protein as well as newly synthesized protein.

It has been suggested that the tumor suppressor gene, Brca2, transports Rad51 into the nucleus following DNA damage and assists in loading Rad51 at the site of a DNA break (Davies et al., 2001; Tarsounas et al., 2003; Yu et al., 2003). The fact that nuclear Rad51 foci are observed

prior to DNA damage in both normal and Brca2 defective cells suggests a Brca2-independent pathway for nuclear entry by Rad51. Rad51 has been observed in the cytoplasmic fraction of $Brca2^{-/-}$ cells, and given that Brca2 is thought to be involved in DNA damage-induced nuclear entry of Rad51 we would expect to see no increase in nuclear Rad51 following exposure of $Brca2^{-/-}$ cells to DNA damage.

**Rad51 undergoes active transport to the nucleus following ionizing radiation in the absence of Brca2.**

To investigate the possible Brca2-independent active transport of Rad51 from the cytoplasmic compartment to the nucleus we made use of the $Brca2^{-/-}$ Capan-1 cell line. Employing the same experimental design as described in Figure 6.2A/B, we harvested Capan-1 cells that had not been exposed to damage, and at 30, 60, and 120 min following the exposure to ionizing radiation (6 Gy). In the absence of cycloheximide there appears to be a slight DNA damage-induced increase in cytoplasmic Rad51. This is especially apparent when comparing the 30, 60 and 120 min time points (in this experiment the faint Rad51 band in the far left hand lane, t=0 CHX -, reflects gel under-loading and should look similar to the band next to it, t=0, CHX +). Interestingly, the nuclear Rad51 fraction shows a steady increase in Rad51 from 0 – 60 min following DNA damage, with a slight decrease at 120 min. Overall, although the levels of nuclear Rad51 are less than observed in HeLa and HCT116 cells (Fig. 6.2), a similar DNA damage-induced increase

**FIGURE 6.2A and B**

**Re-Distribution of Existing Pools and Newly Synthesized HsRad51 Following Ionizing Radiation Induced DNA Damage**

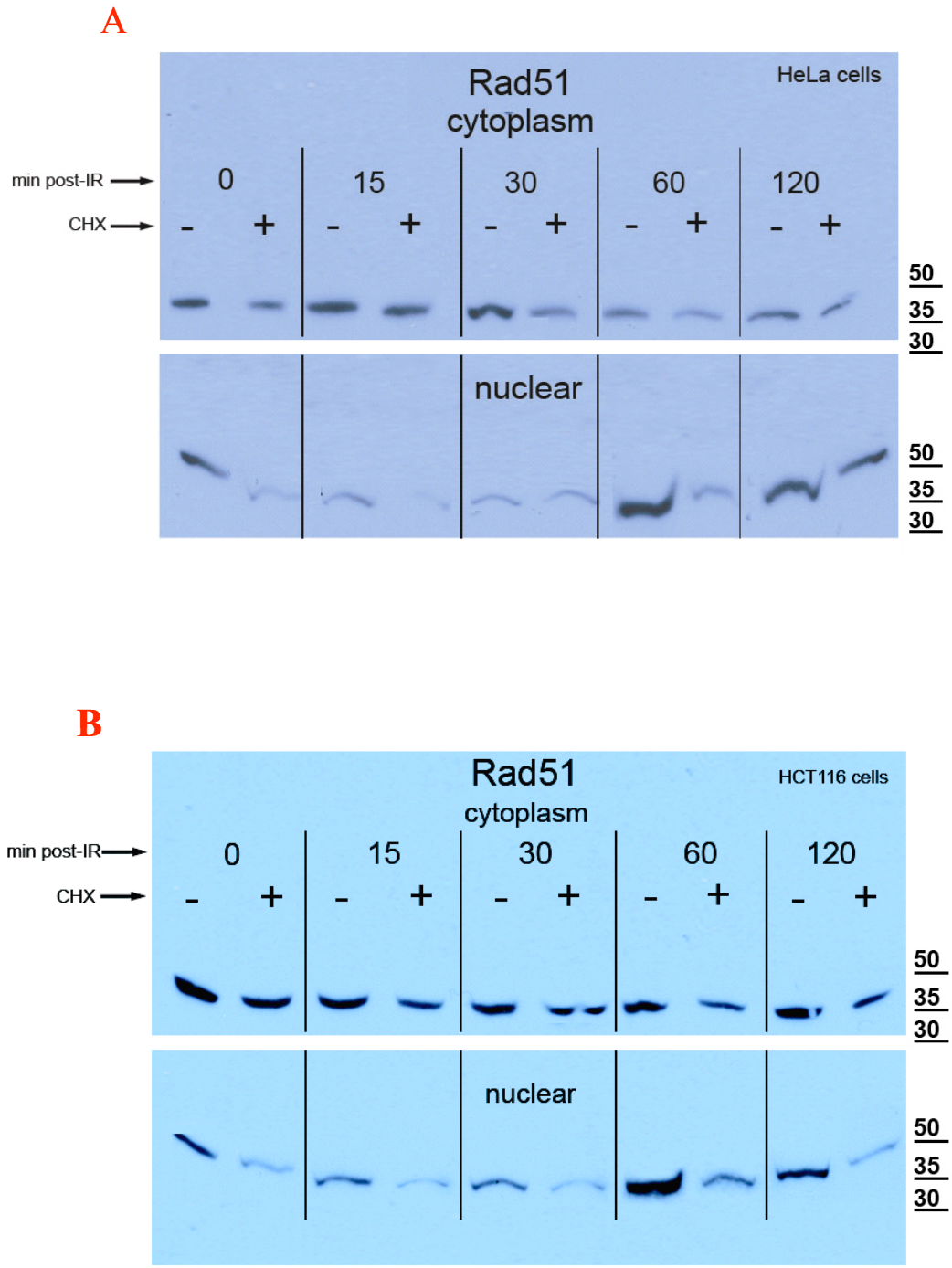

**Figure 6.2A/B – Re-distribution of existing pools and newly synthesized HsRad51 following ionizing radiation induced DNA damage.** Panels A and B demonstrate by sub-cellular fractionation that Rad51 in both HeLa and HCT116 cell lines is redistributed from the cytoplasmic fraction to the nuclear in the absence and presence of both ionizing radiation and treatment with cyclohexamide.

is still observed, particularly at 60 min post-damage. In the presence of cycloheximide cytoplasmic levels of Rad51 in Capan-1 cells following DNA damage do not change significantly until 120 min where a slight decrease is seen. Again, this is similar to HeLa and HCT116 cells treated with cycloheximide. These results demonstrate for the first time that levels of nuclear Rad51 can increase in response to DNA damage in a Brca2-independent manner. As in normal Brca2$^{+/+}$ cells, this increase appears to involve both existing pools of cytoplasmic Rad51 and newly synthesized protein.

It has been reported that Rad51 does not form DNA damage-induced nuclear foci in the absence of a functional Brca2 protein (Yuan et al., 1999; Godthelp et al., 2002; Tarsounas et al., 2003), and we needed to confirm this result to assure ourselves that our work with Capan-1 could reproduce reports in the literature. Additionally, given that we have been able to successfully image endogenous Rad51C and Xrcc3, we are now in a position to address how localization of these 2 proteins may be affected by the absence of a functional Brca2.

**Rad51 does not form damage induced foci in response to ionizing radiation in the Brca2 deficient cell line Capan-1.**

Capan-1 cells were sustained, damaged, fixed and stained using a sequential staining method previously described (Chapters IV and V). In agreement with previous reports (Tarsounas et al., 2003) we find that Rad51 forms distinct nuclear foci in Capan-1 cells prior to DNA damage, and that there is no increase in nuclear focus formation following exposure to ionizing radiaiton (Fig. 6.4A). Interestingly, we find significant amounts of nuclear gamma H2AX prior to exposing Capan-1 cells to ionizing radiation (Fig. 6.4A), which supports the idea that Brca2 deficiency

leads to genome instability and constitutive levels of DNA double strand breaks. Combined with the data in Figure 6.3, it is clear that while Brca2 is necessary for formation of DNA damage-induced nuclear Rad51 foci, it is not required for sustained nuclear Rad51 levels in the absence of DNA damage, and that an alternative pathway must exist for DNA damage-induced transport of Rad51 to the nucleus. As it has been reported previously that Rad51 also requires Xrcc3 and Rad51C for DNA damage-induced focus formation, we sought to test if the loss of Brca2 would affect the constitutive focus formation of Xrcc3 and Rad51C (Bennett and Knight, 2005). Because we had shown that focus formation by Xrcc3 and Rad51C does not require Rad51, it was our hypothesis that both Rad51C and Xrcc3 will not be affected by the loss of Brca2.

**Xrcc3 fails to form foci in the absence of Brca2.**

Capan-1 cells were sustained, damaged, fixed and stained sequentially for endogenous HsXrcc3 and gamma-H2AX as previously described (Chapter IV). In human cell lines in which Brca2 is normal, we have shown that Xrcc3 forms nuclear foci in either the absence of presence of DNA damage (Forget et al., 2004; Bennett and Knight, 2005). Additionally, we found significant Xrcc3 staining in the cytoplasm and in the perinuclear region. However, in Capan-1 cells we find that Xrcc3 fails to form nuclear foci under any condition (Fig. 6.4A). Moreover, we see nearly a complete absence of Xrcc3 staining in Capan-1 nuclei, and an increased tendency for the protein to aggregate in the cytoplasm and perinuclear region both before and after exposure to ionizing radiation.

FIGURE 6.3

# Re-Distribution of HsRad51 in the Brca2 Deficient Cell Line Capan 1

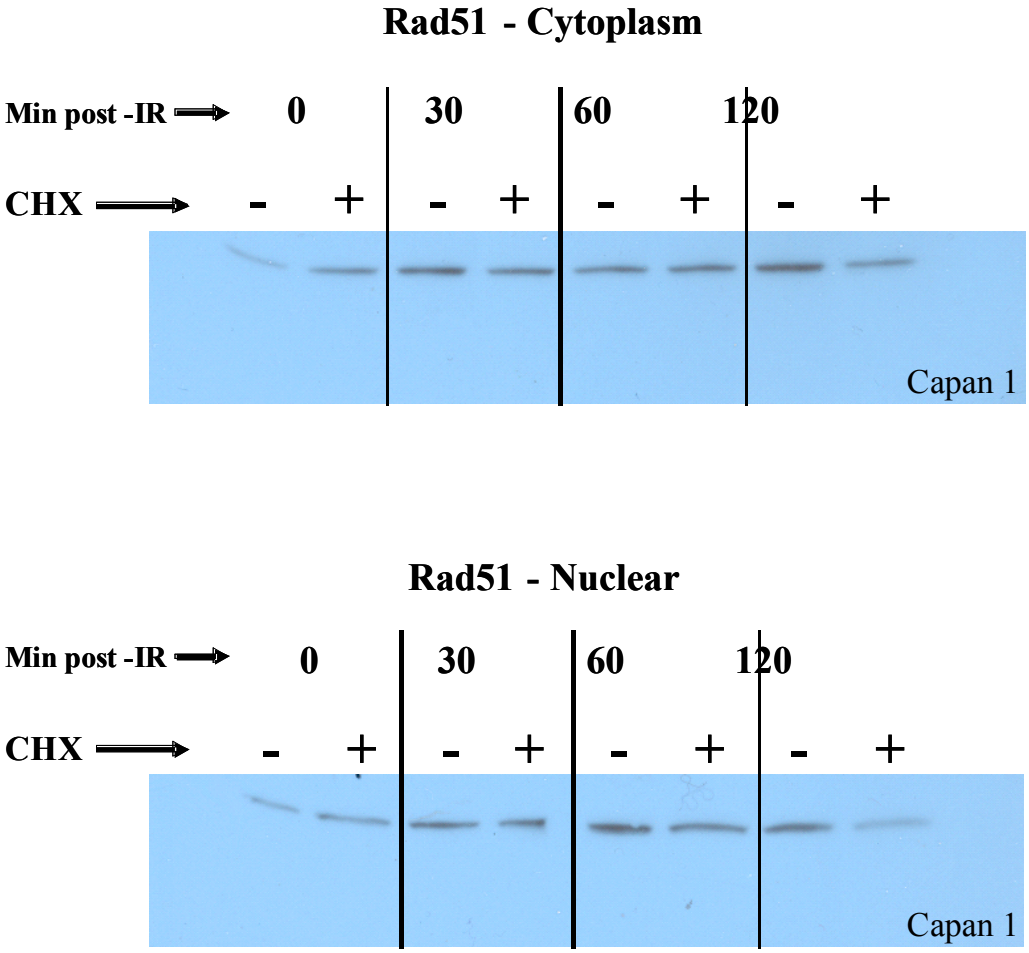

**Figure 6.3 – Re-distribution of HsRad51 in the Brca2 deficient cell line Capan-1.** Upper and lower panels demonstrate, by sub-cellular fractionation, total Rad51 in both the cytoplasmic and nuclear compartments. Cells were collected both prior to and following exposure to 6Gy ionizing radiation as well as plus and minus treatment with the protein synthesis inhibitor cycloheximide . Results in this figure demonstrate the translocation of the existing pool of Rad51 to the nucleus after induction of double strand breaks.

Reports in the literature support the idea that Rad51C and Xrcc3 can exist and function as a stable heterodimeric complex. However, genetic studies suggest independent functions for each protein. Additionally, we have recently shown that the DNA damage-dependent increase in ubiquitination and degradation of Rad51 occurs in cells depleted of Rad51C but not Xrcc3. Further, unlike Rad51 and Xrcc3, Rad51C possesses a functional nuclear localization signal, which could provide Rad51C nuclear entry independent of Brca2 or other repair proteins that contain nuclear localization signals. Together, this information suggested that the cellular localization of Rad51C should not be affected significantly by the absence of a non-functional Brca2 protein.

**Rad51C exhibits normal localization but diminished nuclear foci in Capan-1 cells.**

Sequential staining of Capan-1 cells for both endogenous HsRad51C and gamma-H2AX was performed as decribed (Chapter IV). We find that Rad51C is localized to both the cytoplasmic and nuclear compartments, and forms distinct nuclear foci both before and after exposure to ionizing radiation (Fig. 6.4C). While Rad51C, like Xrcc3, shows some of the same aggregation within the cytoplasm, this does not appear to be significantly greater than what we observe in HEK293 cells (Fig. 6.4D). Overall, in comparison to the staining pattern seen in HEK293 cells, the Rad51C staining pattern in Capan-1 cells is strikingly similar but with decreased fluorescent intensity. While the laser line and intensity, as well as the PMT voltage were similar in both the Capan-1 and HEK293 images, the zoom factor was different and this could account for the appearance of decreased intensity. More work will need to be done to quantify this apparent difference.

**FIGURE 6.4A**

**Immunostaining for HsRad51in Capan 1 Cells Following 8Gys IR**

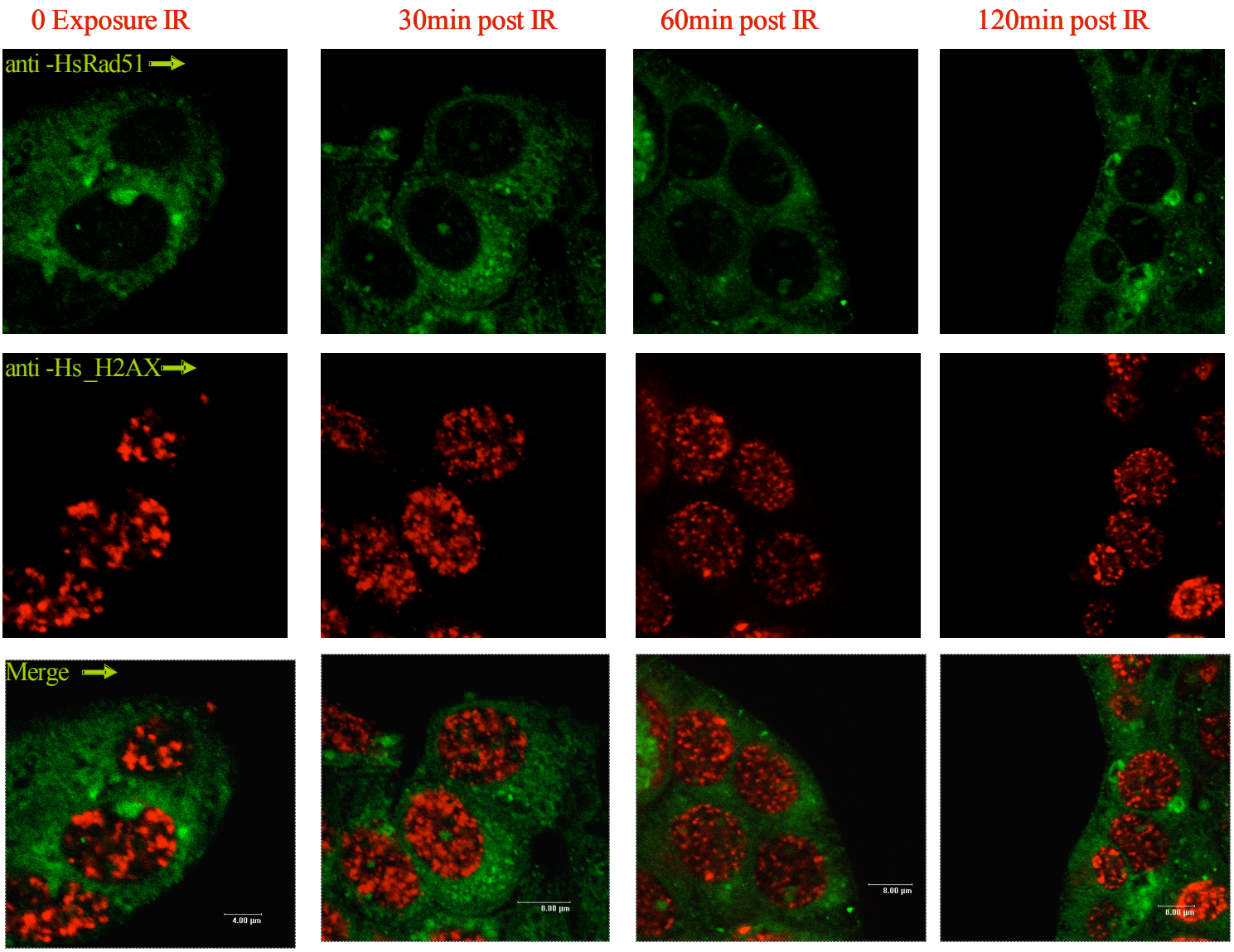

**Figure 6.4A – Immunostaining for HsRad51 in the Brca2 deficient cell line Capan-1 before and after exposure to ionizing radiation.** Capan -1 cells were grown on glass coverslips, exposed to ionizing radiation, and collected at time points of 30 minutes, 1 hour and 2 hours post damage. Additionally a zero time point (no exposure) was collected as well. Cells were immunostained in a sequential staining method (see methods and materials) for HsRad51 (green) and gamma-H2AX (red) and assayed for the ability of Rad51 to form foci in response to damage. The top row is that of Rad51, the middle is gamma-H2AX with the bottom being the merge of the two channels.

**FIGURE 6.4B**

**Immunostaining For HsXrcc3 in Capan 1 Cells Following 8Gys IR**

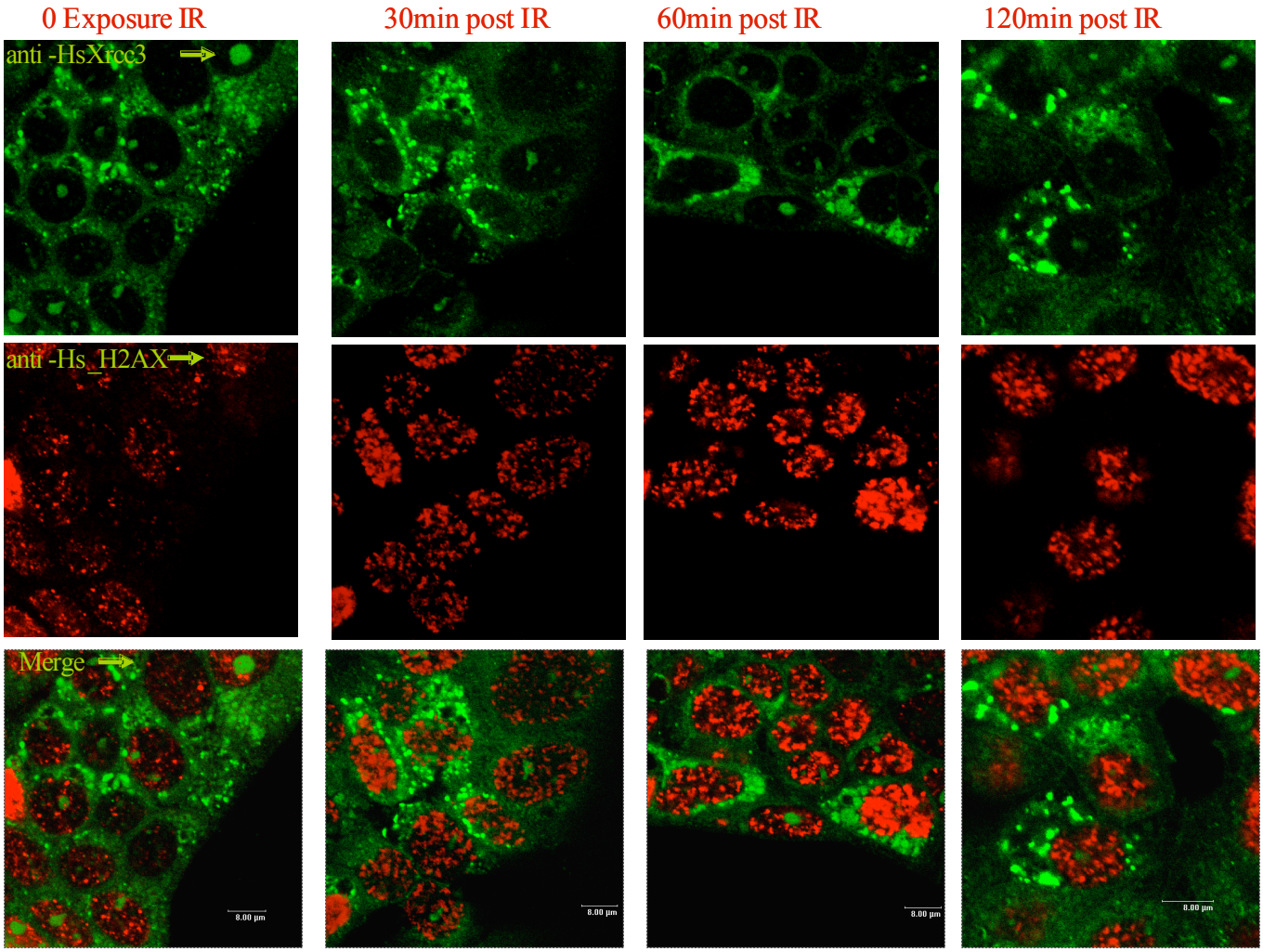

**Figure 6.4B – Immunostaining for HsXrcc3 in the Brca2 deficient cell line Capan-1 before and after exposure to ionizing radiation.** Capan-1 cells were grown on glass coverslips, exposed to ionizing radiation, and collected at 30 min, 1 hour and 2 hours post damage. Additionally a zero time point (no exposure) was collected as well. Cells were immunostained in a sequential staining method (see methods and materials) for Xrcc3 (green) and gamma-H2AX (red) and assayed for the ability of Xrcc3 to form foci in response to damage. The top row is that of Xrcc3, the middle is gamma-H2AX with the bottom being the merge of the two channels.

Based on this data, it appears that Rad51C is largely unaffected by the loss of Brca2. Further, the intensity of foci and overall protein levels seem lower than that HEK293 cells (Fig. 6.4D). Interestingly, we see what may be a related difference in comparing the sub-cellular fractionation of Rad51 in HeLa and HCT116 cells (Fig. 6.2A and B) relative to Capan-1 cell (Fig. 6.3).

Figure 6.4D provides a direction comparison between our results using HEK293 cells and Capan-1 cells 2 hr following DNA damage . In summary, we have reproduced the previous finding that functional Brca2 is required for formation of DNA damage-induced nuclear Rad51 foci. New results demonstrate that while Xrcc3 appears to depleted from the nucleus in Capan-1 cells, it has a tendancy to aggregate in the cytoplasm and perinuclear region. On the other hand, localization of Rad51C appears less dependent on Brca2 as it still exists as nuclear foci, although the numbers and intensity are diminished relative to HEK293 cells. Further studies including analysis of sub-cellular fractions for Xrcc3 and Rad51C are curreently in process.

**FIGURE 6.4C**

## Immunostaining for HsRad51C in Capan 1 cells following 8 Gy IR

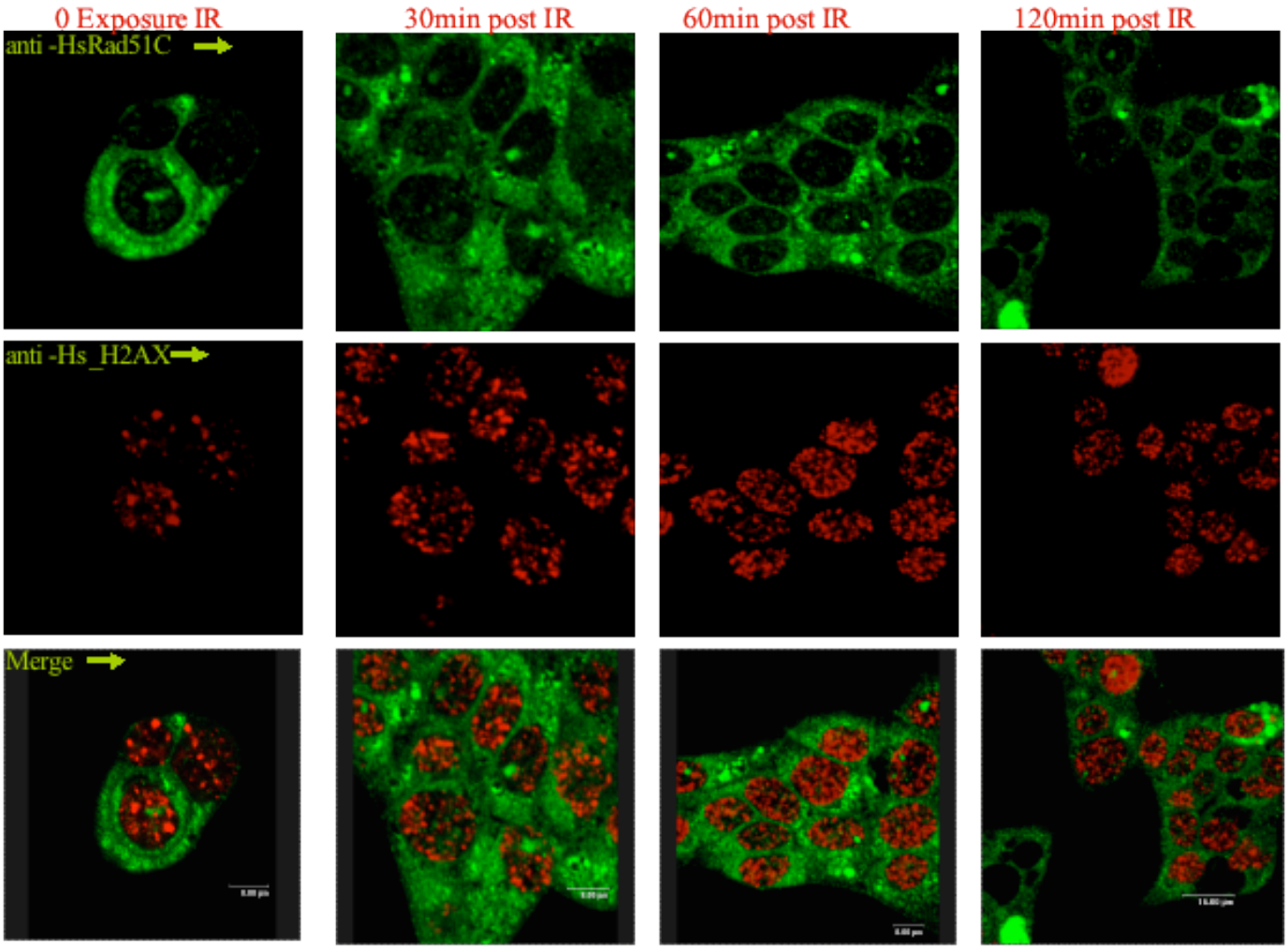

**Figure 6.4C – Immunostaining for HsRad51C in the Brca2 deficient cell line Capan-1 before and after exposure to ionizing radiation.** Capan -1 cells were grown on glass coverslips, exposed to ionizing radiation, and collected at time points of 30 minutes, 1 hour and 2 hours post damage. Additionally a zero time point (no exposure) was collected as well. Cells were immunostained in a sequential staining method (see methods and materials) for Rad51C (green) and gamma-H2AX (red) and assayed for the ability of Rad51C to form foci in response to damage. The top row is that of Rad51C, the middle is gamma-H2AX with the bottom being the merge of the two channels.

**FIGURE 6.4D**

## Comparison of immunostaining for HsRad51, HsRad51C and HsXrcc3 in HEK293 vs. Capan 1 cells, 2 hrs post 8 Gy IR

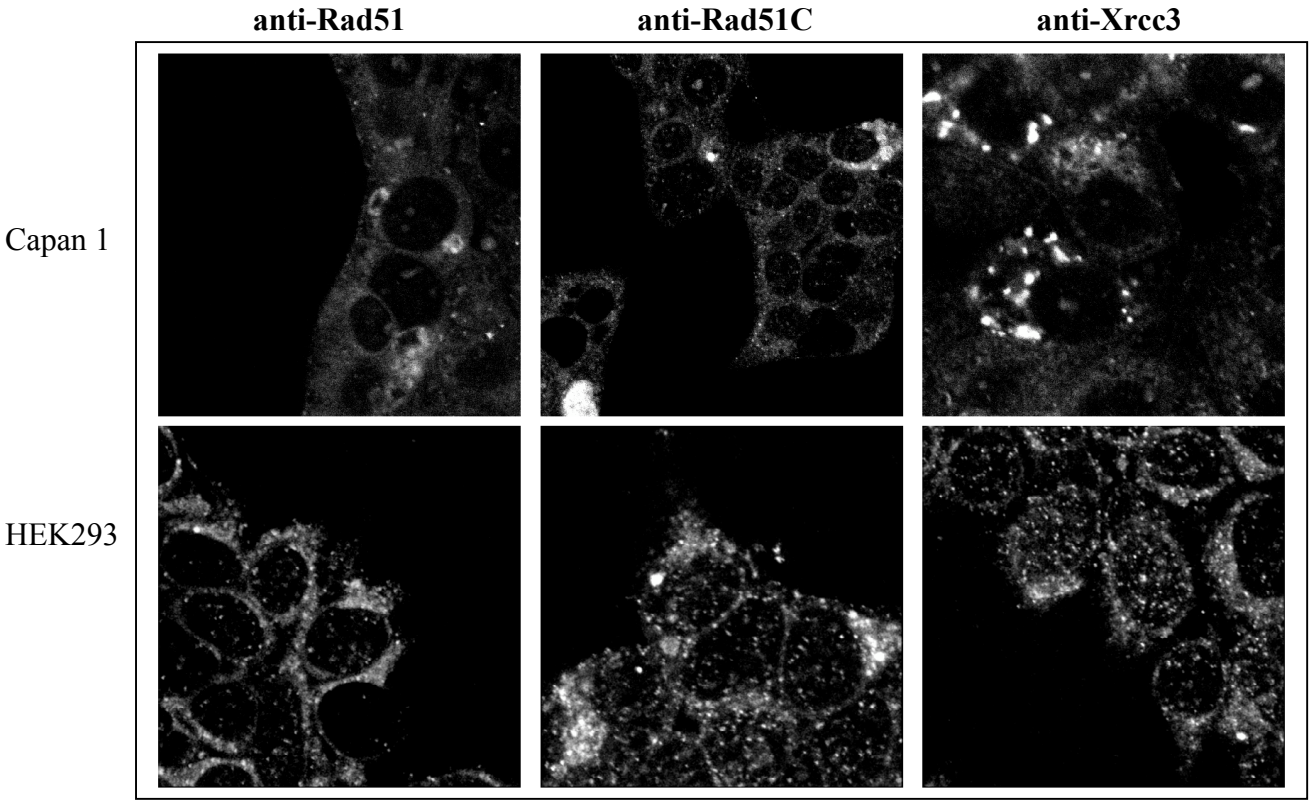

**Figure 6.4D – Comparison of immunostaining for Rad51, Rad51C and Xrcc3 in HEK293 and Capan 1 Cell Lines, 2 hours post 8Gys IR.** Capan-1 and HEK293 cells were grown on glass coverslips, exposed to ionizing radiation, and collected 2 hours post damage. Cells were immunostained in a sequential staining method (see methods and materials) for Rad51, Rad51C and Xrcc3 in both Capan-1 cells (top row) and HEK293 cells (bottom row). Comparisons were made of the ability of each protein to form foci in both a Brca2 deficient cell line (Capan-1) as well as cell containing a functional Brca2 protein.

## Discussion

Nuclear foci formed by the Rad51 recombinase are observed in small number during S-phase and in much greater numbers in response to exogenous DNA damage. Formation of DNA damage-dependent Rad51 foci requires many other proteins including upstream signaling components of the repair pathway (Thompson and Schild, 2002), all 5 Rad51 paralogs (Bishop et al., 1998; Takata et al., 2001; Yoshihara et al., 2004) as well as the Brca2 tumor suppressor protein (Yuan et al., 1999; Godthelp et al., 2002; Tarsounas et al., 2003). In contrast, Rad51 S-phase foci form independent of Brca2 (Tarsounas et al., 2003). Therefore, it appears that the DNA damage-induced recruitment of recombinational DNA repair proteins to nuclear foci is a complex and highly regulated process involving signaling and regulatory proteins as well as catalytically active repair proteins. To further our understanding of potential functional relationships among several of these proteins, we have studied the cellular localization of Rad51, Rad51C and Xrcc3 in both $Brca2^{+/+}$ and Brca2-defective cells. Although the increase in nuclear Rad51 in response to DNA damage has been ascribed specifically to Brca2, we find that a low level increase in nuclear Rad51 following DNA damage occurs independent of Brca2. Additionally, we find that Brca2 also affects the cellular localization of Xrcc3 quite dramatically, and less so for Rad51C.

In the absence of DNA damage Rad51 is localized to the cytoplasm and nucleus in both $Brca2^{+/+}$ and Brca2-defective cells, yet specific association with chromatin is observed exclusively during S-phase (Tarsounas et al., 2003). Using 3 different cell lines we show here that nuclear levels of

Rad51 increase dramatically between 60 and 120 min following exposure of cells to DNA damage with a corresponding decrease in cytoplasmic levels of Rad51. We also find an increase in chromatin-associated Rad51 following DNA damage. Although previous studies suggest that cellular Rad51 levels do not change following DNA damage (Yuan et al., 1999) we show here that DNA damage-induced nuclear transport of Rad51 involves both existing pools of protein and newly synthesized Rad51.

It has been suggested that Brca2 is responsible for nuclear transport of Rad51 following DNA damage (Davies et al., 2001; Tarsounas et al., 2003) and work presented clearly indicate an alternate pathway for nuclear entry by Rad51 in cells not exposed to DNA damage. However, our studies using Capan-1 cells now show that some level of Rad51 does move to the nucleus following DNA damage independent of Brca2. Capan-1 cells carry only one allele of Brca2 with a truncation that removes the C-terminal nuclear localization signals. Although some small amount of Brca2 may still localize to the nucleus and transport the Rad51 that we observe, it is more likely that a Brca2-independent pathway is operating. It has been suggested that because Rad51C has a functional nuclear localization signal that it may be involved in transport of DNA repair proteins with which it associates (French et al., 2003). Rad51C interacts specifically with Rad51, and this interaction has been shown to increase in the presence of Xrcc3 (Schild et al., 2000). Therefore, we propose that Rad51C functions to transport Rad51 into the nucleus in two different ways, under non-damage conditions allowing Rad51 to form S-phase foci, and as an alternative Brca2-independent pathway for Rad51 nuclear transport following DNA damage (see Discussion and Future Directions section). Although further work is clearly required, it may be that the major function of Brca2 is not in nuclear transport of Rad51, rather its direct role in

loading Rad51 onto the resected single-stranded end at a DNA break (Yang et al., 2002; Pellegrini et al., 2002; Pellegrini et al., 2002).

Although Rad51C and Xrcc3 can exist as a stable heteromdimer, and Xrcc3 is destabilized in the absence of Rad51C (Henry-Mowatt et al., 2003; Lio et al., 2004), genetic evidence supports the idea that these two proteins also function independent of one another (Takata et al., 2001; Yonetani et al., 2005). Our recent work showing that ubiquitin-mediated degradation of Rad51 is regulated by Rad51C but not Xrcc3 clearly shows independent function for these two paralogs. In the present study we find that while Rad51C foci are visible in the nuclei of Capan-1 cells, no Xrcc3 foci are apparent and the overall level of nuclear Xrcc3 is significantly less than in $Brca2^{+/+}$ cells. This establishes a functional role for Brca2 in regulating nuclear entry of Xrcc3 and perhaps also in formation of Xrcc3 nuclear foci. Preliminary Western blot analyses of sub-cellular fractions of Capan-1 cells before and after DNA damage supports the idea that Xrcc3 levels in the nucleus are down significantly, but this needs to repeated and verified, and is currently underway. However, this initial work suggests that nuclear entry by Xrcc3, but not Rad51C, may also depend on Brca2. No information is currently available to suggest that Xrcc3 and Brca2 interact, but one can easily imagine that such an interaction could be direct or indirect through Xrcc3's ability to bind to Rad51. Further studies are planned to provide additional detail. Additionally, a model for how Brca2, Rad51, Rad51C and Xrcc3 may interact to regulate nuclear entry of the various proteins and to assist in formation of both S-phase Rad51 nuclear foci and DNA damage-induced foci is presented in the Chpater VIII.

# MATERIALS AND METHODS

## Cell Lines

HEK293 and HeLa cells were obtained from ATCC and were maintained in DMEM supplemented with 10% fetal bovine serum and 1% Pen/Strep. Capan-1 cells were obtained from ATCC and were maintained in Iscoves's Modified Dulbecco's Medium with 20% fetal bovine serum. HCT116 cells were obtained from ATCC and were maintained in McCoy's 5A Medium Modified with 10% fetal bovine serum. All cell lines were plated within 10 cm culture dishes and incubated in the dark at 37 degrees Celsius with 5% (v/v) $CO_2$.

## Antibodies

Primary antibodies used in Western blots of sub-cellular fractions were either Rad51 polyclonal (Upstate Biotechnology) or Rad51 monoclonal (clone 3C10, Upstate Biotechnology), and both underwent protein A purification and were tested for specificity by RNAi (Bennett and Knight, 2005). Detection of HsRad51 was performed using goat anti-rabbit or goat anti-mouse HRP tagged secondary antibodies (Visualizer® system, Upstate Biotechnologies).

Primary antibodies used in immunofluorescence were rabbit anti-phospo-histone H2AX (Ser139) (Cell Signaling Technologies), mouse anti-HsRad51 (clone 3C10, Upstate Biotechnology), mouse anti-HsRad51C (clone 2H11/6, Novus Biologicals, Inc.), and mouse anti-HsXrcc3 (clone 10F1/6, Novus Biologicals, Inc.). Mouse anti-HsRad51, HsRad51C and HsXrcc3 all underwent a proprietary protein A purification methodology in our lab, and were tested for specificity by target specific siRNA both by western blot and immunofluorescence (Bennett and Knight, 2005).

Secondary antibody detection was performed using goat anti-mouse and goat anti-rabbit highly cross absorbed Alexa 488 (absorption 495 emission 519) and Alexa 647 (absorption 650 emission 655). Alexa 488 and Alexa 647 demonstrate no significant cross in excitation and/or emission spectra (http://probes.invitrogen.com/resources/spectraviewer/). DNA was counterstained with Vectashield Fluorescent Mounting Media containing DAPI (4', 6' – diamidino-2-phenylindole; Vector Laboratories).

**Damage-induced DNA double-strand breaks**

Cells were exposed to 6 Gy ionizing radiation for sub-cellular fractionation and 8 Gy for immunofluorescence, (higher irradiation doses are used in immunofluorescence to ensure focus formation) using a Gammacell 40 $^{137}$Cs source (MDS Nordion Ottawa, ON Canada). After exposure cells were allowed to recover fat 37 degrees Celsius (5% $CO_2$) for the indicated times. Cells were then methanol fixed and prepared for immunostaining as described (Bennett and Knight, 2005).

**Sub-cellular fractionation**

HEK293, HeLa, HCT116, and Capan-1 cells were plated on 10 cm culture dishes and incubated in the dark at 37 °C under an atmosphere of 5% (v/v) $CO_2$ in air. When cells reached approximately 90% confluency, cycloheximide (20 μM) was added to selected dishes. One hour later, a set of plates was irradiated with 8 Gy. Cells were harvested 30, 60, and 120 min following irradiation. Control cells were not irradiated.

For the preparation of samples, subcellular fractionation was performed on exponentially growing cells according to the procedure described by Liu and Lim (2005). Briefly, 5-8 X $10^6$ cells were removed by trypsinization from the plates, and pelleted by centrifugation in 15 ml sample tubes. Cells were transferred to fresh, 1.5 ml tubes and washed with PBS. Cells were then resuspended in Buffer A (10 mM HEPES-KOH, pH 7.1, 50 mM NaCl, 0.3 M sucrose, 0.5% Triton X-100, 0.1 mM EDTA, 1 mM DTT, and protease inhibitors). After 15 min incubation on ice, cells were pelleted at 1500 x *g* for 5 min. Supernatants (cytosolic fraction) were transferred into fresh tubes, and pellets were washed with Buffer B (10 mM HEPES-NaOH pH 7.1, 0.1 mM EDTA, 1 mM DTT, and protease inhibitors), after which they were resuspended in Buffer C (10 mM HEPES-KOH pH 7.1, 50 mM NaCl, 0.5% NP40, 0.1 mM EDTA, 1 mM DTT, and protease inhibitors) and incubated on ice with sporadic vortexing. After 15 min, samples were centrifuged for 10 min at 10000 x *g*, and supernatants (nuclear proteins) transferred to fresh tubes. Pellets were washed again with Buffer C and centrifuged briefly. Pellets were added 2x SDS-PAGE loading buffer, sonicated for 30 min in a sonicator bath, and boiled for 5 min. The supernatants after centrifugation contain the chromatin fraction.

Proteins were separated by electrophoresis on 10% SDS-PAGE gels, and transferred onto Immobilon-FL membranes (Millipore) at 20V for 30 min. Blots were rinsed for 5 min with blocking buffer and washed with 15% non-fat milk in blocking buffer for 1 hour with slow rocking. Blots were incubated for at least 1h at RT (or O/N at 4°C) after which they were washed with blocking buffer (3 x 5 min) and incubated for 1 hr with HRP conjugated secondary antibody. After thorough washing with blocking buffer (6 x 5 min), specific bands were detected

by chemiluminescence (Visualizer Western Blot Detection Kit, Upstate), and exposure to X-ray film (Denville Scientific)

**Immunostaining and confocal microscopy**

Cells were grown on coverslips in a 6 well dish. For fixation, media was aspirated off and cells washed once with PBS and immersed in 100% methanol at -20 °C for 8 minutes. Cells were blocked in a marine blocking agent overnight at 4 °C. Incubation with both primary and secondary antibodies was done by a sequential staining methodology. The first primary was added, followed by its appropriate secondary, this was then repeated until all antibodies were added. This was performed in 6 well dishes for 1 hr at 37 °C in a humid environment using a slide warmer (Fisher) . Cells were washed five times for five minutes each in PBS after incubation with both primary and secondary antibodies. Coverslips were mounted using Vectashield with DAPI and sealed with polyurethane (nail polish) then stored in the dark at 4 °C. Visualization of immunostains was performed by confocal microscopy using a Leica TCS DMIRE2 SP2 AOBS instrument, laser intensity settings, photomultiplier tube settings (PMT setting on Leica microscopes are tunable, whereas they are not on other commercial confocal microscopes, allowing us to eliminate any possible "crosstalk"), field size and zoom factors remained the same throughout a data set, with all image footprints being collected and stored. Image processing was performed using the accompanying Leica Confocal Software, all corrections were uniform for each image, and contrast was increased by a factor of 4.0, brightness decreased by a factor of 6.0 followed by a 4% gamma correction. In no way did this alter the data. Images represented within this manuscript were not edited by any non-Leica software and were placed within the manuscript void of any manipulation.

## PREFACE TO CHAPTER VII

The work presented here represents a significant technological breakthrough in which we describe the first successful use of 4Pi microscopy to visualize endogenous nuclear proteins. Although this technology has been available since the early 1990s, it was only through the optimization of fixation conditions, use of highly purified antibodies, and other methodological considerations, that we were able to develop an appropriate imaging protocol. The important biological outcome of this work is our identification chromatin structures (clusters) containing the histone variant H2AX whose size and distribution support a model in which they serve as platforms for the robust nuclear response that has been observed by many groups following exposure of cells to DNA damage. Additionally, our quantification of H2AX cluster size and distribution provides a mechanism to explain the limited expansion of H2AX phosphorylation at 1-2 Mb from the site of a DNA break. A detailed explanation of 4Pi microscopy and novel quantitative methods are provided in the Supplementary Information following the text of Chapter VII. As of this writing, this work has been submitted for publication.

I am solely responsible for development of the cell fixation and immunostaining protocols. Having been trained in Stefan Hell's group and involved with the creation of 4Pi technology, Dr. Bewersdorf's contribution involved technical aspects of the operation of the 4Pi microscope as well as development of the quantitative methods used to measure cluster size and distribution. Hypothesis development, data interpretation and writing were a collaborative effort between myself and Drs. Bewersdorf and Knight.

# CHAPTER VII

## Novel H2AX Chromatin Structures Revealed by 4Pi Microscopy


## ABSTRACT

DNA double-strand breaks (DSBs) caused by cellular exposure to genotoxic agents or produced by inherent metabolic processes initiate a rapid and highly coordinated series of molecular events resulting in DNA damage signaling and repair. Phosphorylation of histone H2AX to form γ-H2AX is one of the earliest of these events and is important for coordination of signaling and repair activities. An intriguing aspect of H2AX phosphorylation is that γ–H2AX spreads a limited distance up to 1–2 Mbp from the site of a DNA break in mammalian cells. However, the mechanism that defines the boundary of γ–H2AX spreading and the distribution of H2AX throughout the genome has not yet been described. Here we report the identification of novel H2AX chromatin structures using the first successful application of 4Pi microscopy to visualize endogenous nuclear proteins. We find that H2AX is not distributed randomly throughout bulk chromatin, rather it exists in distinct clusters that themselves are uniformly distributed within the nuclear volume. Our data support a model in which the size and distribution of H2AX clusters define the boundaries of γ-H2AX spreading, and also provide a platform for the immediate and robust response observed following DNA damage.

## INTRODUCTION

Maintenance of genome integrity is critical for organism development and survival, and higher organisms have evolved sophisticated mechanisms for detection and repair of chromosome breaks. DNA damage results in the rapid and coordinated action of various pathways including activation of cell cycle checkpoints (O'Driscoll and Jeggo, 2006; Stucki and Jackson, 2006) and histone modification near the site of the break (Rogakou et al., 1998; Thiriet and Hayes, 2005), as well as recruitment of chromatin remodeling enzymes (Thiriet and Hayes, 2005; Peterson and Cote, 2004; Nussenzweig and Paull, 2006), cohesins (Kim et al., 2002; Strom et al., 2004; Unal et al., 2004) and DNA repair proteins (O'Driscoll and Jeggo, 2006; Stucki and Jackson, 2006; Nelms et al., 1998). The significance of these molecular processes is highlighted by the fact that defects in many are associated with an increased risk of cancer as well as developmental and immunologic abnormalities (O'Driscoll and Jeggo, 2006). Important insights into the positioning of nuclear signaling and repair proteins, and their response to various types and levels of genomic insults has been achieved using immunofluorescence methods (Nelms et al., 1998; Bennett and Knight, 2005; Bekker-Jensen et al., 2005). However, it has been impossible to distinguish fluorescent signals in a three-dimensional (3D) environment that are closer together than 500-800 nm in distance given the depth resolution limits of current light microscopes. With ~100 nm resolution along the optic axis (*z*-axis), 4Pi microscopy (Hell and Stelzer, 1992; Gugel et al., 2004) provides a significant increase in resolution and has allowed more defined images of cellular structures such as microtubules, mitochondria or the Golgi apparatus (Egner et al., 2004). However, until now imaging of endogenous nuclear proteins had not been achieved (a comparison of 4Pi *vs*. confocal is described below in **Materials and Methods**). In this study we describe the first successful use of 4Pi microscopy to visualize

endogenous nuclear proteins. By applying novel quantitative methods to the analysis of both confocal and 4Pi data we have determined the local, global and relative 3D distribution of H2AX and γ–H2AX fluorescent signals in response to DNA damage and repair.

## RESULTS

**Imaging of H2AX and γ-H2AX using 4Pi Microscopy.** HeLa cells were fixed and stained for γ–H2AX and H2AX at 15, 45, 90, 180, 360 and 720 min following exposure to 3 Gy ionizing radiation (IR). Figure 7.1 shows the 3D distribution of H2AX (green) and γ–H2AX (red) throughout HeLa nuclei at 15, 45 and 180 min after IR treatment. Several important observations come from visual inspection of the data. First, we find that H2AX appears in distinct clusters rather than being distributed throughout the nucleus in more homogenous fashion. Second, while the size of H2AX clusters remains relatively constant before and following IR exposure, γ–H2AX clusters grow in size up to approximately 90 min post-IR. Third, H2AX and γ–H2AX clusters are dispersed throughout the entire nuclear volume. Finally, within the enhanced resolution limit of 4Pi microscopy, interestingly we find very little to no coincident staining of H2AX and γ–H2AX at all time points before and after IR exposure.

**FIGURE 7.1**

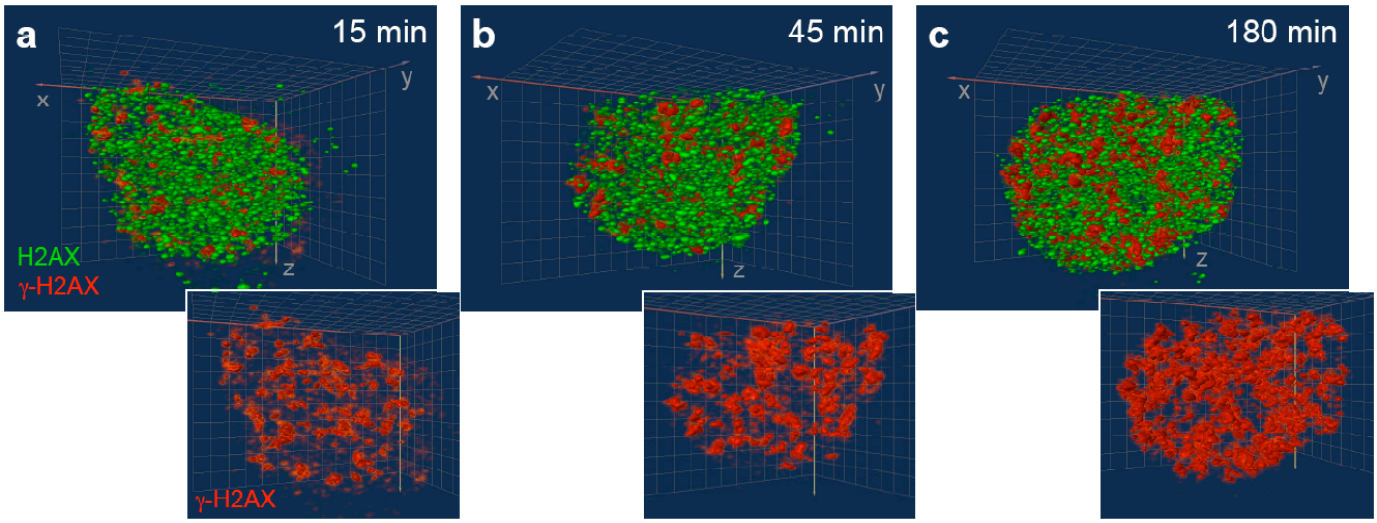

**Figure 7.1 - 4Pi images of H2AX and γ-H2AX clusters during a time course of DNA damage and repair**. HeLa cells exposed to 3 Gy IR were fixed 15, 45 and 180 min after irradiation and immuno-labeled with γ-H2AX (red) and H2AX (green) antibodies. Images were obtained using a 4Pi microscope and deconvolved. 3D rendered 4Pi data for the 15, 45 and 180 min post-IR time points are displayed in **a**, **b** and **c**, respectively. Insets show γ-H2AX data alone.

**Determination of H2AX and γ−H2AX Cluster Sizes.** To clarify our observation regarding the cluster sizes for H2AX *vs*. γ−H2AX, 4Pi data were quantified using an autocorrelation algorithm (see **Methods**). The average diameter of H2AX clusters remained close to the technical resolution limit (< 120 nm) throughout the entire time course (Fig. 7.2; Fig. 7.6). In contrast, the characteristic size of γ−H2AX clusters increased rapidly during the initial 90 min post-IR, reaching a plateau of approximately 600 nm diameter from 6 to 12 hr post-IR. In mammalian cells, phosphorylation of H2AX is observed within the first minute following exposure to DNA damaging agents and a $t_{1/2}$ has been estimated to be approximately 1 min with maximum levels reached at 10–20 min (Rogakou et al., 1998; Rogakou et al., 1999). Increases in γ−H2AX cluster size beyond this time (Fig. 7.2; Fig. 7.6) can most reasonably be interpreted as resulting from localized chromatin expansion near the sites of breaks (Kruhlak et al., 2006). The fact that we observe little to no change in the size of H2AX clusters or in their distribution throughout the 12 hr time course (Figs. 7.1 and 7.2, and see below) argues against the idea that DNA damage induces large scale chromatin movement (Kruhlak et al., 2006) or accumulation of multiple breaks at a common site (Lisby et al., 2003).

**3D Nuclear Distribution of H2AX and γ−H2AX Clusters.** The 3D distribution throughout the nucleus of both H2AX and γ−H2AX clusters was quantified by measuring their fluorescence intensity recorded by a confocal microscope within a series of 3D shells of 400 nm thickness characterized by their distance to the nuclear periphery (Fig. 7.3; Fig. 7.7). Examples of the raw confocal data used for the calculations are displayed in Fig. 7.3 (Fig. 7.3a-d; DAPI, H2AX, γ-H2AX and overlay, respectively). The nuclear dimensions were determined using smoothed DAPI data (Fig. 7.3e) and non-overlapping 3D shells of 400 nm thickness, differing by their

**FIGURE 7.2**

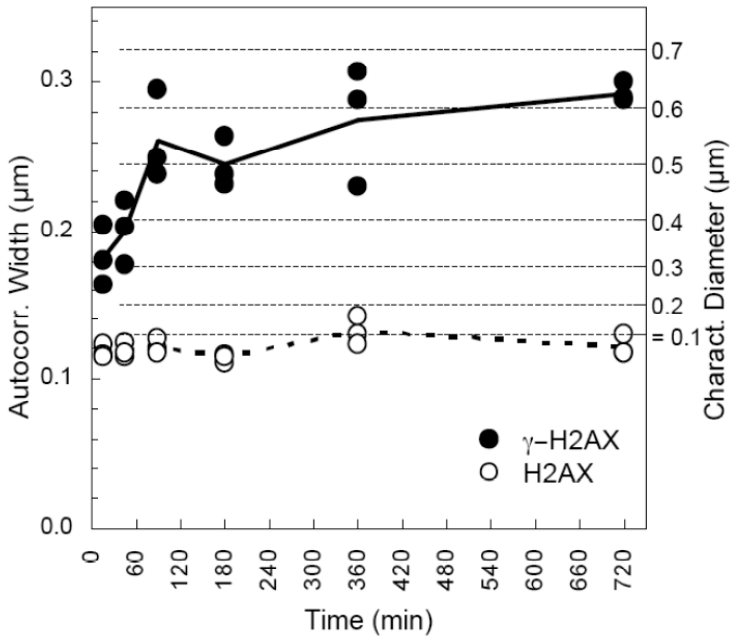
Autocorr. Width (µm)
Charact. Diameter (µm)
Time (min)
0.0
0.1
0.2
0.3
0.7
0.6
0.5
0.4
0.3
0.2
= 0.1
0
60
120
180
240
300
360
420
480
540
600
660
720
γ–H2AX
H2AX

**Figure 7.2 - Cluster size as a function of time after DNA damage.** The characteristic size of both H2AX and γ–H2AX clusters were determined for each time point during DNA repair using the autocorrelation function of the deconvolved 4Pi data (see **Methods**). While the H2AX clusters remain at sub-resolution size during the whole time course, the characteristic size of γ-H2AX clusters increases 2-fold reaching a plateau after approximately 90 min.

distance to the nuclear border (multiples of 400 nm), were derived (Fig. 7.3f). For all individual points in the time course we find that the H2AX and γ-H2AX levels remain on average constant throughout the entire nuclear volume (Fig. 7.3g-i; Fig. 7.7a-g). This supports a model in which DSBs can occur in any region of the nucleus and are likely processed and repaired in the area where they arise. It has been proposed that in yeast multiple DSBs may accumulate at repair centers (Lisby et al., 2003). However, in accord with recently published work (Kruhlak et al., 2006), the fact that we find γ–H2AX clusters appearing throughout the entire nuclear volume argues against the ideas that specific repair centers exist in mammalian nuclei, or that DNA repair takes place preferentially near the nuclear periphery, center or any other particular location. This suggests that γ–H2AX simply serves as a mark for both the recruitment and retention of signaling and repair factors required to mount an appropriate response to DNA damage (Stucki and Jackson, 2006; Fernandez-Capetillo et al., 2003), irrespective of its nuclear location. Consistent with a general increase in the amount of γ–H2AX immediately following exposure to IR, we find that the γ–H2AX/H2AX ratio increases on average five-fold within the first 15 min following exposure to IR (Fig. 7.3g, h). We also observe an overall decrease in the level of γ-H2AX fluorescence at 360 and 720 min post-IR (Fig. 7.3i; Fig. 7.7f, g). Related approaches have been used to provide information regarding the radial distribution of proteins within the nucleus (Irinopoulou et al., 1997; Knowles et al., 2006), but the new algorithm used for our analysis provides novel insight into the steady-state localization in 3D as well as stress-induced changes in the distribution of γ–H2AX throughout the nuclear volume.

**FIGURE 7.3**

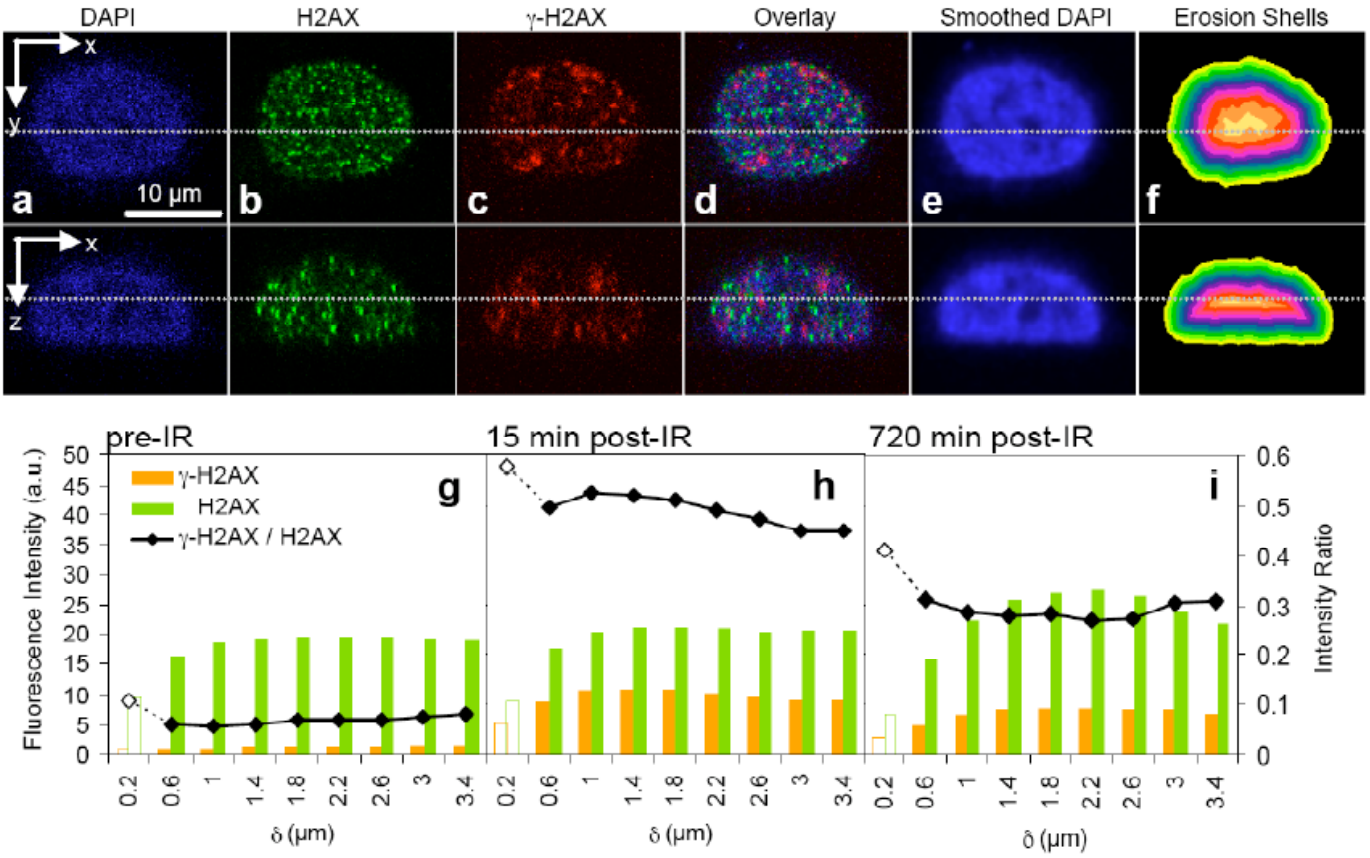
DAPI
H2AX
γ-H2AX
Overlay
Smoothed DAPI
Erosion Shells
x
y
z
10 μm
a
b
c
d
e
f
pre-IR
15 min post-IR
720 min post-IR
γ-H2AX
H2AX
γ-H2AX / H2AX
g
h
i
Fluorescence Intensity (a.u.)
Intensity Ratio
δ (μm)
0.2
0.6
1
1.4
1.8
2.2
2.6
3
3.4

**Figure 7.3 - 3D distribution of H2AX and γ−H2AX clusters in the nuclear volume**. Fluorescence intensities of both the γ−H2AX) (red) and H2AX (green) channels were analyzed in 3D. Examples of *xy* and *xz*-sections of 3D data sets showing the DAPI (**a**), H2AX (**b**), γ-H2AX (**c**) and overlay (**d**) signals used for the calculations are shown. Nuclear dimensions were determined by creating a series of shells shown in different colors (**f**) based on eroding smoothed DAPI stain images (**e**) in 400 nm steps (see **Methods**). Histograms for t = 0 (**g**), 15 (**h**) and 720 (**i**) min post-IR averaged over 10-11 cells are displayed, and show a time-dependent change in fluorescence intensity for γ−H2AX signal (red) and little change in the intensity of H2AX signal. Both intensities show little to no dependence on the distance from the nuclear periphery (δ). Due to an inaccuracy in the identification of the nuclear boundary, defined by a smoothed DAPI signal threshold, a continuous rise in the signal for the first two shells instead of a step-like rise is observed (**g-i**). For the ratios shown between γ−H2AX and H2AX this cancels out.

**Lack of Coincident Staining of H2AX and γ−H2AX.** We observe no significant coincident staining for H2AX and γ−H2AX at any time following exposure to IR (representative cuts through a deconvolved 4Pi 3D data set are shown in Fig. 7.4a). This was confirmed and quantified by analyzing the cross-correlation of the voxel values of both channels in the 3D 4Pi data sets. The results are displayed using a 2-dimensional cytofluorogram (Fig. 7.4b) in which the horizontal axis corresponds to the signal level of the H2AX channel (green) and the vertical axis to the γ−H2AX channel (red). The entire dynamic range of the cytofluorogram could be visualized using a logarithmic color table. The cytofluorogram consists mainly of two lobes oriented in horizontal and vertical directions and shows very little signal in the region between the lobes, thus ruling out significant co-localization. To investigate possible co-localization in more detail, the cytofluorogram counts in the area between the two lobes were analyzed further by comparing profiles parallel to the vertical lobe at different horizontal positions (dotted lines in Fig. 7.4b and profiles in inset). Apart from an expected scaling factor in the amplitude of the profiles, all profiles show the same shape. The same behavior can be observed for profiles along the other direction. Since even minor amounts of systematic co-localization would result in a peak or shoulder with varying positions in the different profiles, this indicates that no significant co-localization occurs. The small number of counts observed in the area between the lobes (~5% of total voxels representing H2AX and/or γ−H2AX clusters) is consistent with the purely coincidental occurrence of separate H2AX and γ−H2AX clusters in a distance closer than or at the resolution limit of the microscope (in each channel, 2-6% of the nuclear voxels in this area of the cytofluorogram represent clusters). The fact that we observe no mixed populations of H2AX and γ-H2AX signals means that phosphorylation of virtually all the H2AX within a given cluster

FIGURE 7.4

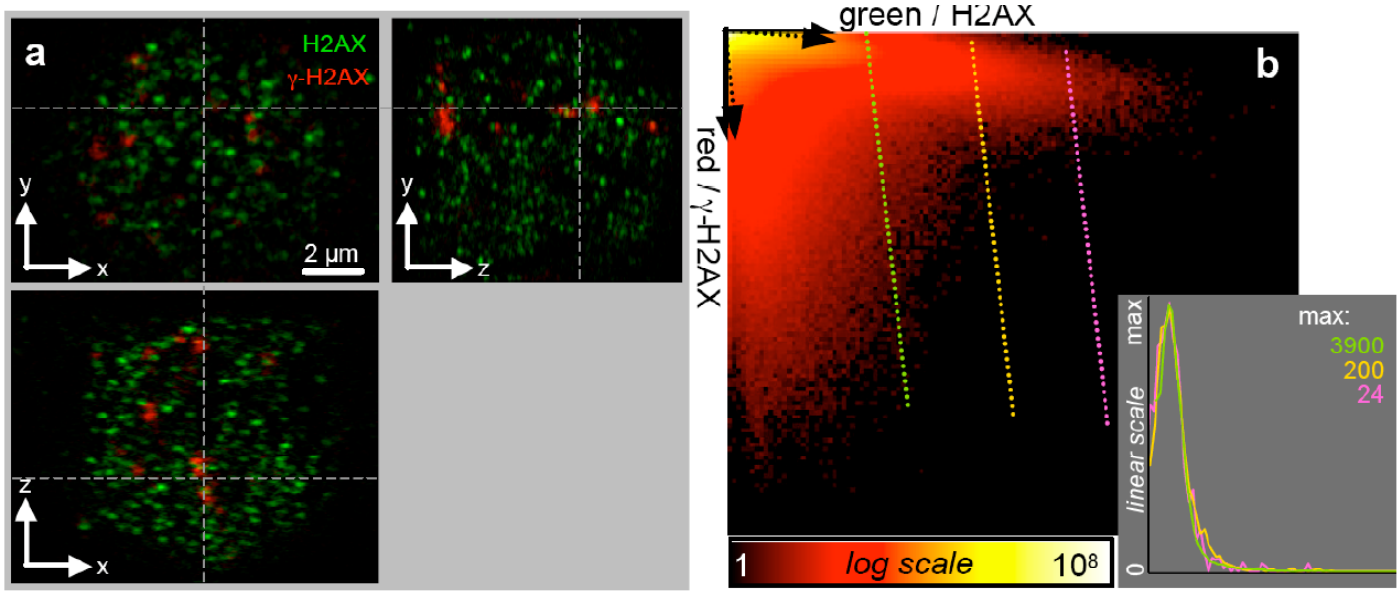
a
H2AX
γ-H2AX
y
x
2 µm
y
z
z
x
green / H2AX
red / γ-H2AX
b
1
log scale
10⁸
max
linear scale
0
max:
3900
200
24

**Figure 7.4 - Lack of co-localization of H2AX and γ−H2AX staining throughout the nuclear volume.** Sections in all directions through a typical 3D 4Pi data set (**a**) show no significant overlap between the red (γ-H2AX) and green (H2AX) signals (dashed lines represent positions of different sections). Analysis of all data sets by cytofluorograms (example shown in **b**) reveals a minimal signal overlap (note the logarithmic color scale). Profiles in the inset in **b** represent the cytofluorogram data along the dotted lines (**b**). The fact that they are the same shape agrees with an occasional coincidental overlap of the resolution-limited signals. The profiles were normalized according to the numbers displayed in the inset. The dotted arrows (upper left in **b**) indicate the directions for the cross-talk corrected signal.

spreads very rapidly following DNA damage, and is essentially complete before 15 min. This agrees with previous biochemical studies showing that H2AX phosphorylation is complete within 10-20 min following DNA damage (Rogakou et al., 1998). To eliminate the possibility that staining with the first antibody combination may sterically hinder access of the second we found that the appearance of H2AX and γ–H2AX clusters was identical regardless of which was stained first (not shown). Additional controls in which the secondary antibody fluorescent conjugates were switched such that H2AX appears red and γ–H2AX green (Fig. 7.8), demonstrate the specificity of cluster appearance and rule out any instrumental or preparative artifacts.

The absence of coincident staining of H2AX and γ–H2AX at later times in the repair process, e.g. 360 and 720 min, is consistent with the idea that dephosphorylation of γ–H2AX occurs only following its removal from nucleosomes, and that it is not simply swapped for another molecule of unphosphorylated H2AX. In fact, recent studies show that *S. cerevisiae* Pph3 phosphatase targets γ–H2AX after its displacement from DNA (Keogh et al., 2006). This idea is also supported by our observation that the characteristic γ–H2AX cluster size remains fairly constant from 6 to 12 hr post-IR (Fig. 7.2), yet the overall fluorescence intensity appears to decrease at these later times (Fig. 7.7f, g). The latter observation also suggests that loss of the γ–H2AX signal, whether by phosphatase action or by direct removal of γ–H2AX from nucleosomes (Keogh et al., 2006; Chowdhury et al., 2005; Bouquet et al., 2006), occurs randomly within a given cluster. This is different than the model for directional spreading of the DNA damage-induced phosphorylation of H2AX, which is best shown by chromatin immunoprecipitation

(Schroff et al., 2004) and supported by immunofluorescence data (Kruhlak et al., 2006; Aten et al., 2004).

## DISCUSSION

Recent studies suggest that DSB processing causes a local expansion of chromatin in the region of the break. While γ-H2AX is not required for the initial ATP-dependent expansion, it was speculated that it is essential to sustain chromatin decondensation as DNA repair progresses, thereby providing a link between the expanded chromatin region and the localized spread of γ-H2AX (Kruhlak et al., 2006). Our data now strongly suggest that the size of H2AX clusters and distance we observe between them serves to limit spreading of γ–H2AX and associated chromatin expansion. The average number of H2AX clusters observed in our images approximates 5,000 (see **Methods**) and in a diploid nucleus 6 x $10^9$ bp DNA would be accommodated by approximately 30 million nucleosomes. Assuming that H2AX is distributed randomly throughout the genome and that this number of nucleosomes is accounted for by the 5,000 clusters we observe, we estimate that 6,000 nucleosomes should be related to each cluster. This number of nucleosomes corresponds to about 1.2 Mbp of DNA, and we note that this closely matches estimates of the amount of DNA in which H2AX phosphorylation spreads from a break in mammalian cells (Rogakou et al., 1998; Rogakou et al., 1999). However, our analysis shows that H2AX clusters have a diameter below the resolution limit (~100 nm) of 4Pi microscopy. Assuming a cylindrical shape of 6 nm height and 5.5 nm radius for a nucleosome (570 $nm^3$ volume), a maximum number of 900 closely packed nucleosomes could fit into a sphere of 100 nm diameter. Therefore, only up to 15% of total nucleosomes can be located in the clusters. This strongly suggests that nucleosomes containing H2AX are not distributed

uniformly throughout bulk chromatin. Instead they are concentrated within the 100 nm diameter clusters. Thus, although H2AX represents 2.4% of the total H2A in HeLa cells (Rogakou et al., 1998), the fractional amount of H2AX within a cluster must be significantly higher. These observations could be accommodated by higher order chromatin structures proposed to contain on the order of 1-2 Mbp DNA in which chromatin loops emanate from a central region (Munkel et al., 1999; Huebert and Bernstein, 2005) where H2AX would be concentrated. We propose that the H2AX clusters observed here using 4Pi microscopy correspond to these higher order structures. Therefore, our data support a model in which spreading of H2AX phosphorylation in response to DNA damage is constrained within structures defined by these H2AX clusters. The subsequent increase in size of the γ-H2AX clusters between 20-100 min following DNA damage may result from localized chromatin expansion (Thiriet and Hayes, 2005; Peterson and Cote, 2004; Nussenzweig and Paull, 2006; Kruhlak et al., 2006) and increased flexibility due to resection of one DNA strand without concomitant loss of nucleosomes (Schroff et al., 2004). While a localized aggregation of proximal DSBs may contribute in part to this (Aten et al., 2004), our data suggests that this does not involve large scale chromatin movement. Additionally, the local concentration of H2AX within these clusters, which themselves are uniformly distributed throughout the nuclear volume, may contribute to the immediate and robust response of signaling and repair proteins following DNA damage.

This study represents a significant advance in our ability to visualize and quantify endogenous nuclear proteins in 3D. Combined, these methods have allowed us to visualize a chromatin structure at the 100 nm resolution level, and to quantify the size and distribution of both H2AX and γ-H2AX clusters in response to DNA damage. The general application of these methods

will provide unprecedented insights into cellular molecular events, and now specifically events related to the maintenance of genome integrity as well as most aspects of nuclear metabolism.

## MATERIALS AND METHODS

**Antibodies**. Primary antibodies were mouse monoclonal anti-γ-H2AX (phospho-Ser139) (clone JBW301, Upstate Biotechnology, catalog# 06-636) and rabbit polyclonal anti-H2AX (Upstate Biotechnology, catalog# 07-627). Rabbit polyclonal anti-H2AX was protein-A purified by us, whereas monoclonal anti-γ-H2AX was purified by Upstate Biotechnologies as described on the product sheet, and purification was verified by Coomassie stained protein gel. Immunofluorescence detection was achieved using Alexa Fluor 488 goat anti-mouse IgG (H+L; Invitrogen, #A-11029), Alexa Fluor 488 goat anti-rabbit IgG (H+L; Invitrogen, #A-11034), Alexa Fluor 647 goat anti-mouse IgG (H+L; Invitrogen, #A-21236),. Rhodamine Red-X goat anti-rabbit IgG (H+L; Invitrogen, #R-6394) or Rhodamine Red-X goat anti-mouse IgG (H+L; Invitrogen, #R-6393) all of which are highly cross-absorbed. All primary and secondary antibodies were applied at a 1:500 dilution in blocking buffer containing 20% marine blocking agent in PBS. For conventional confocal microscopy, cells were mounted in Vectashield Fluorescent Mounting Media containing DAPI (4′, 6′- diamidino-2-phenylindole; Vector Laboratories). For 4Pi microscopy, cells were mounted in a solution of 87% glycerol in 130 mM Tris-HCl (pH 7.4).

**Cells and damage-induced DNA double strand breaks.** HeLa cells from ATCC were maintained in DMEM with 10% fetal bovine serum (FBS) and 1% Pen/Strep. Cells were grown to approximately 80% confluency, in an atmosphere containing 5% $CO_2$ at 37 °C. Cells were

exposed to 3 Gy IR ($^{137}$Cs) using a Gammacell 40 (MDS Nordion) and were incubated at 37 °C (5% $CO_2$) for the indicated times.

**4Pi *vs.* confocal imaging of histones H2AX and γ−H2AX**. Type C 4Pi microscopy covers twice the solid angle of standard (confocal) microscopy (2.7π with the objectives used) for both excitation and detection by combining the wavefronts of two high numerical aperture (NA) objective lenses coherently (Hell and Stelzer, 1992; Gugel et al., 2004; Hell, 1990). For constructive interference, the favorable opposing lens arrangement realized results in a focal volume or point-spread function (PSF) with a central peak of ~100 nm width (full-width-half-maximum, FWHM), 5 to 7-fold improved in comparison to regular confocal PSFs (Fig. 7.5a and b, insets). Imaging nuclear structures with interference microscopy techniques such as 4Pi microscopy is potentially difficult: wavefront distortions in the vicinity of cell nuclei that degrade the 4Pi PSF have been reported (Egner et al., 2004). However, by matching the cytosolic and nuclear refractive indices by glycerol-embedding the sample and using 1.35NA glycerol immersion lenses (Martini et al., 2002) with the embedding medium for immersion, we found that refractive indices could be matched for HeLa cells. In fact, the high quality of the PSFs enabled removal of the ghost-images produced by the axially shifted side-maxima in the 4Pi PSF by simple linear 5-point deconvolution (R. Medda, S. Jakobs, S. W. Hell, J.B., personal communication). The improved resolution achieved by 4Pi microscopy compared to standard confocal microscopy of the same sample is shown in Fig. 7.5 with the lower insets comparing the PSFs of confocal (Fig. 7.5a) *vs*. 4Pi (Fig. 7.5b) microscopes.

**FIGURE 7.5**

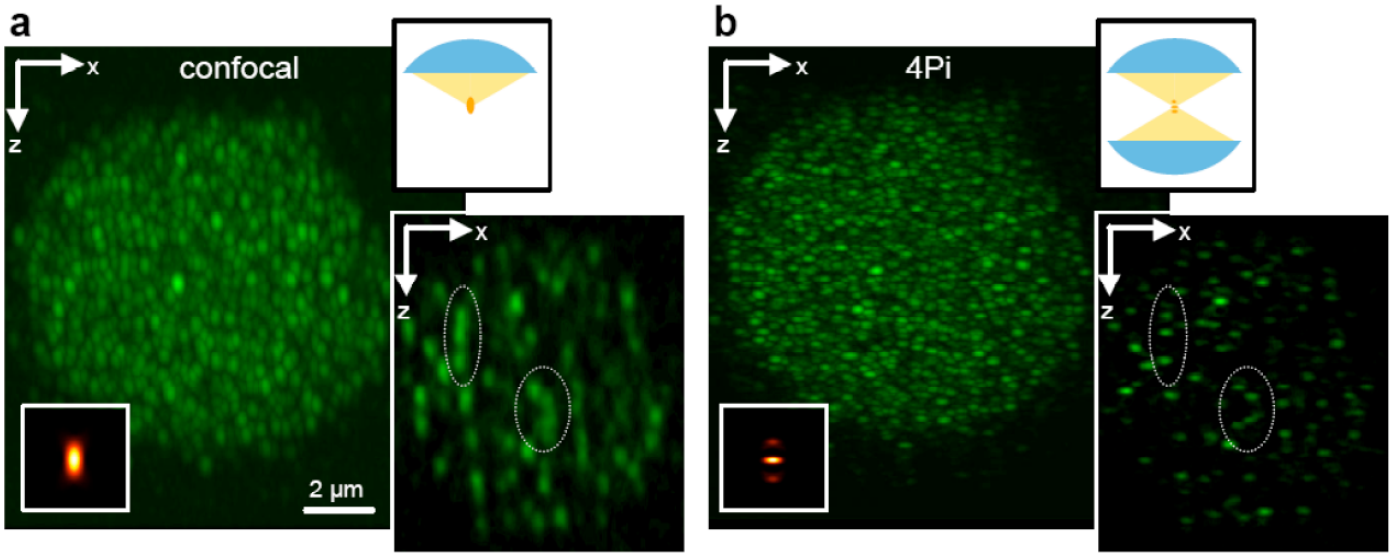

**Figure 7.5 - Comparison of confocal *vs*. 4Pi microscopy for endogenous human histone H2AX.** The data shown in panels **a** and **b** represent the H2AX staining in a HeLa cell nucleus as seen with confocal and 4Pi microscopy, respectively. The two opposing objectives used coherently in 4Pi microscopy (**b**, upper inset) focus into the same spot producing a sharp spot of about 100 nm axial width (**b**, lower left inset) in contrast to the 500-800 nm axial resolution of a regular confocal microscope (**a**, lower left inset). The optical side lobes that accompany the central spot in 4Pi microscopy are removed by mathematical deconvolution, resulting in much sharper images than in regular confocal microscopy. Panels **a** and **b** show the same nucleus in a maximum projection in *y*-direction, indicating the much increased axial resolution. The insets in the lower right corners of **a** and **b** show the same single *xz*-section recorded with confocal and 4Pi microscopy, respectively. The dotted ellipses in the insets mark areas where the resolution enhancement can be seen best.

**Confocal Microscopy.** Cells were grown on poly-D-lysine treated glass coverslips in a 6 well dish to approximately 80% confluency before exposure to IR. Following exposure cells were removed from the incubator at appropriate times for fixation. Growth medium was aspirated from the wells, cells were quickly rinsed in room temperature PBS and then immediately immersed in 100% methanol at -20 °C for 7 min. Cells were blocked in a marine blocking agent overnight at 4 °C and washed once in PBS (5 min, room temp). Incubation with primary and secondary antibodies was performed in 6 well dishes in a humid environment (Fisher slide warmer, 37 °C, 90 min each). Cells were washed 3 times in PBS (10 min each) following incubation with each primary antibody and 5 times in PBS (10 min each) following incubation with each secondary antibody. For all double-staining procedures, cells were stained in a sequential manner as opposed to using antibody cocktails. For example, cells were first incubated with anti-γ-H2AX followed by incubation with the secondary Alexa 647. Subsequently, cells were incubated with anti-H2AX followed by its appropriate secondary, Alexa 488. The choice of Alexa 488 and Alexa 647 was purposeful, in that there is little to no cross talk in the emission and excitation of this fluorophore pair, all but eliminating the possibility of artificial co-localization patterns. Coverslips were mounted using Vectashield with DAPI and sealed with polyurethane (nail polish). Samples were then stored in the dark at 4 °C. 3-dimensional data sets were recorded using a Leica TCS SP2 AOBS confocal microscope (Leica Microsystems Inc.). Data were recorded with a 63x glycerol immersion objective (Leica HCX PL APL 63x/1.30NA GLYC CORR) at a pinhole diameter of 1 “Airy unit”. The glycerol components of the Vectashield containing DAPI were duplicated and used as the objective immersion media to maintain matching refractive indexes. Before imaging, the correction collar

was adjusted to optimize imaging conditions by examination of the sample intensity and profile in an *xz*-scan. DAPI, Alexa 488 and Alexa 647 dyes were excited by laser lines 405 nm, 488 nm and 633 nm, respectively. The Leica TCS SP2 AOBS is equipped with tunable spectral detection windows for its photo-multiplier tubes (PMT) and the detection ranges were set as follows: DAPI was detected at a range of 414–478 nm; Alexa 488 at a range of 504–582 nm, and the Alexa 647 at a range of 648–736 nm. To avoid any chance of cross talk between the DAPI and Alexa 488 signals, the "sequential scan" feature of the microscope was used. The DAPI and Alexa 647 channels were collected together while the Alexa 488 was collected separately, noting there was no observed cross-talk between the DAPI and Alexa 647 channels. Samples were imaged at a zoom factor of 2, resulting in a field size of 119 μm x 119 μm. With 1024 x 1024 pixels, the resulting pixel size in the *xy*-plane was 116 nm x 116 nm. The distance between neighboring *xy*-images was set to 122 nm, allowing nearly cubic voxels to be generated, thereby simplifying the subsequent data processing (see **Methods**). For each data stack, 100-200 frames were recorded, resulting in image stacks with a depth between 12 μm and 24 μm. The recording *z*-range was chosen to be significantly larger than the thickness of the cells in the field of view to avoid artifacts in the data analysis.

Data was collected at 400 Hz line speed in a bi-directional scanning mode. The resulting mismatch between subsequent lines of forward and backward scan direction was easily corrected by adjustments of the phase as well as in automated post-processing of the data. Due to the low laser powers applied, no bleaching could be observed in controls, where the same data stack was recorded a second time. Signal overflow was avoided and linearity of the signal response to the fluorescence level was achieved by careful adjustment of the photomultiplier voltages.

**4Pi Microscopy.** 4Pi samples were prepared between two opposing quartz coverglasses that are matched in width at 220 μm (± 5 μm). The upper coverslip, on which the cells were grown, was acid etched (70% ethanol/1% hydrochloric acid in PBS) for 5 min, washed 3 times in PBS (room temp) and bathed in DMEM with poly-D-lysine (1 mg/ml) for 1 hr at room temperature. Slips were then washed once in DMEM followed by two washes in DMEM containing 10% FBS and 1% Pen/Strep and seeded with cells. The lower coverslip which contains a transparent center surrounded by a mirror reflective surface was not treated by acid etching or poly-D-lysine. The lower coverslip mirror can be utilized in adjusting the two wavefronts in the reflective mode of the 4Pi system. Cells were fixed and stained as described above for confocal imaging, except that a Rhodamine Red-X secondary antibody was used to stain the γ-H2AX. Mounting of 4Pi coverslips is achieved by placing the lower slip, (mirrored surface) into the 4Pi sample holder, a round metal ring with an indentation to match the quartz coverslip. The lower slip is adhered to the sample holder using polyurethane (nail polish). Once dried, 40 μl of an 87% glycerol in 130 mM Tris-HCl, (pH 7.4) embedding media was added to the lower slip. The upper slip was removed from the PBS of the last wash, allowed to air dry briefly and added to the lower coverslip, sandwiching the cells between the two opposing quartz slips. Samples were sealed with nail polish and stored in the dark at 4 °C.

High resolution data was collected using the Leica TCS 4Pi microscope equipped with a pair of 100x/1.35NA glycerol objectives. To permit the Leica TCS 4Pi to operate in Type C mode (Leica Microsystems Inc. manufactures the TCS 4Pi in type A mode), achieving an enhanced axial resolution of 100 nm with lower side maxima, a pair of glass wedges and an optical flat

were added to the microscope, as previously described (Gugel et al., 2004). The Alexa 488 and Rhodamine Red-X fluorescence was recorded simultaneously by using 2-photon excitation at 780 nm wavelength (Chameleon MP laser, Coherent Laser Group) with beam expander 3 of the microscope and the photon counting avalanche photodiodes of the system (short pass SP700, band passes 525/50 and 620/60, reflection short pass 560, all Chroma Technology Corp.). The pinhole was set to 1 "Airy unit". The objective correction collars, focus alignment and the interference phase of the microscope were adjusted for each individual sample put in the system. The embedding media, in this case 87% glycerol in 130 mM Tris-HCl, pH 7.4, was also used as the immersion media to ensure continuity in the refractive index from objective to objective.

Stacks of *xz*-images were recorded with a *y*-distance of 31 nm between neighboring slices. With a pixel size in each *xz*-image of 31 nm x 31 nm the resulting voxels were cubic. A line scan frequency of 400 Hz with 512 pixels per line was selected. The number of lines and frames was chosen to include the whole nucleus of a single cell in each data stack. Typically, stack dimensions were 10 to 15 μm in each direction, resulting in 300 to 450 image slices. Each line was averaged 4 times in bidirectional scan mode and two frames were accumulated for each image slice to increase the signal to noise ratio.

**Deconvolution.** Raw data from the 4Pi microscope were imported into the image processing software Imspector (Garching Innovation, http://www.garching-innovation.de/en/technoang/software.html). Subsequently, each stack was smoothed in all 3 dimensions with a Gaussian-shaped filter of sub-resolution size, linearly deconvolved using a 5-

point deconvolution (R. Medda, S. Jakobs, S. W. Hell, J. Bewersdorf, unpublished), background-corrected by the average background value and the voxels with negative values set to zero.

**Determination of the number of H2AX clusters.** Deconvolved 4Pi data sets as well as the simulated 4Pi data set of a reference cluster were loaded into a user-written algorithm programmed in "C". The deconvolved data were smoothed with a normalized Gaussian-shaped filter of sub-resolution size and the voxel with the largest value in the smoothed data set was identified. The amplitude of the reference cluster data set was rescaled to match the determined maximum voxel value, the reference data set was shifted to the same position as the maximum and subtracted from the smoothed data set. With the remaining data set, the procedure was repeated starting with the search for the maximum voxel value until the maximum fell below a threshold value that could not be assigned visually to H2AX clusters in the data set anymore. The number of H2AX clusters determined is equal to the number of maxima found. This procedure was repeated for 18 4Pi data sets at different fixation time points after IR. The results varied by about a factor of 2, with typical results yielding about 5,000 clusters. No temporal dependence could be detected.

**Colocalization Analysis.** Deconvolved 4Pi data sets were loaded separately into a user-written algorithm programmed in "C" that created a quantitative cytofluorogram, a 2-dimensional histogram showing the cross-correlation between the signal levels in the two detection channels for all voxels in a 3D data set. The *x*-axis corresponds to the signal level of the H2AX channel and the *y*-axis matches the signal level of the γ-H2AX channel (Fig. 7.4b). To increase the visibility of low counts in the cytofluorogram, a logarithmic color table was used. The

cytofluorogram features two elongated lobes of high counts oriented along the *x*- and the *y*-axes. Due to very small cross-talk, these areas are slightly tilted relative to the coordinate axes (dotted arrows in Fig. 7.4b), a fact which we accounted for in the analysis.

**Cluster Size Determination.** To determine the average size of H2AX and γ-H2AX clusters, the deconvolved 4Pi data was loaded into a user-written computer algorithm programmed in "C". The algorithm calculated the autocorrelation of each data set along the *x*, *y*, and *z*-axes in real space by shifting a copy of the data set and summing the product of the voxel values of the two data sets at every position. To exclude background from the analysis as far as possible, only voxels related to H2AX or γ-H2AX clusters, defined by a mask, were regarded in the calculation of the auto-correlation profiles. The mask was generated by thresholding the smoothed data sets at a level slightly above the background. To assure that no artifacts were created by the edges of the mask, the mask was dilated (see **Spatial Distribution Analysis** below) with a radius of 200 nm to include all voxels near bright structures within the resolution range of the 4Pi microscope. This way we assured that all signal related to clusters is included. The program stores the auto-correlation profiles along the *x*, *y*, and *z*-axes. For the analysis, the minimum of the auto-correlation profiles within a 2 μm shift range was subtracted from the profiles, the maxima of the profiles were normalized to 1, and the autocorrelation width, which we define as the shift corresponding to the 50% value of the normalized profiles, was determined (see Fig. 7.6a, b for examples). Summaries of all autocorrelation widths determined that way are presented in Figure 7.6c and d. By calibrating the autocorrelation width with simulated solid spheres of known diameter that were convolved with Gaussian-shaped functions of 4Pi resolution, the "characteristic diameter" was determined (see right axis in Fig. 7.2). The characteristic

**FIGURE 7.6**

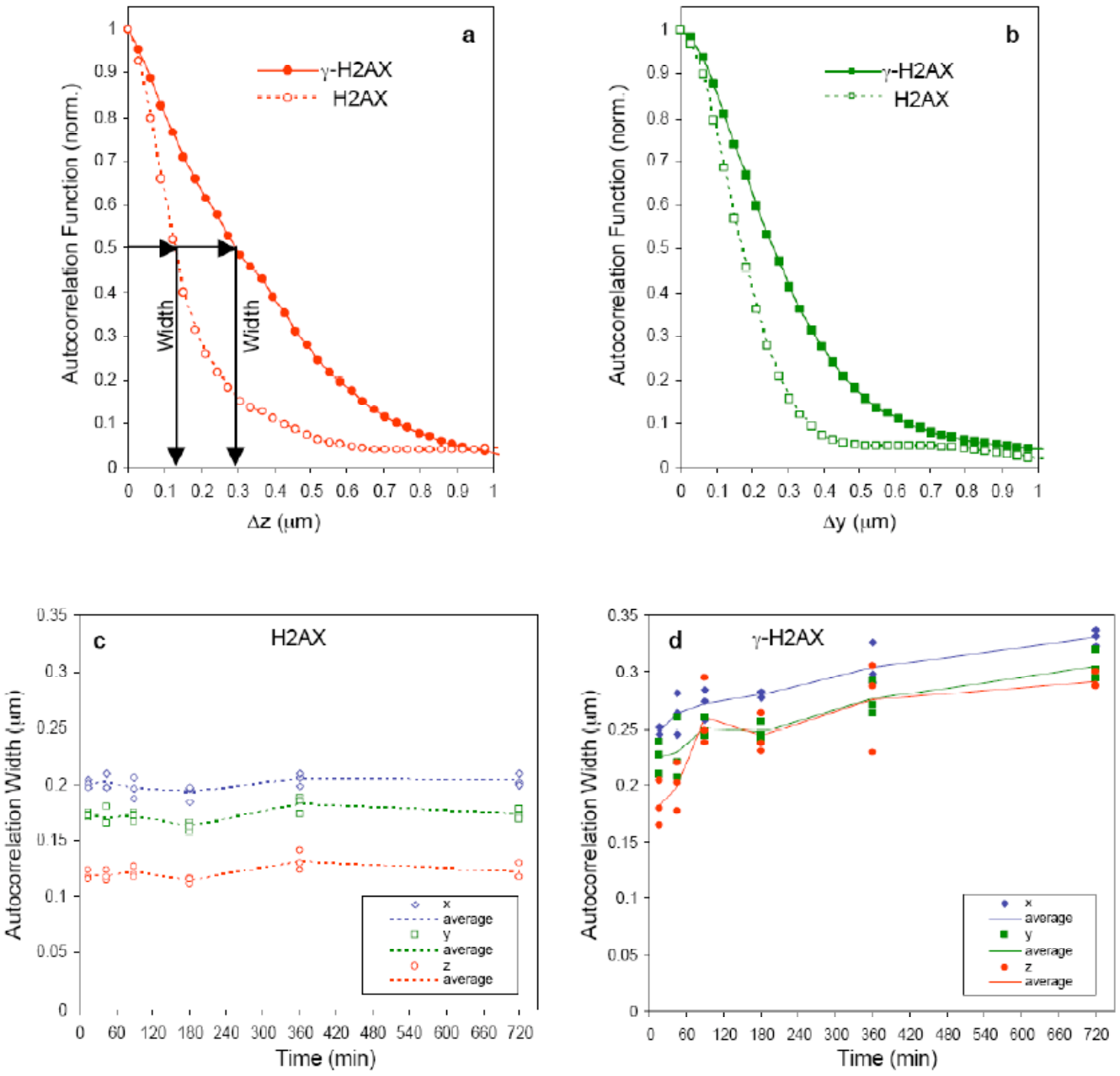
a
γ-H2AX
H2AX
Width
Width
Autocorrelation Function (norm.)
Δz (μm)
b
γ-H2AX
H2AX
Autocorrelation Function (norm.)
Δy (μm)
c
H2AX
Autocorrelation Width (μm)
x
average
y
average
z
average
Time (min)
d
γ-H2AX
Autocorrelation Width (μm)
x
average
y
average
z
average
Time (min)

**Figure 7.6 - Autocorrelation function and cluster size determination.** Panels **a** and **b** show the autocorrelation function for the deconvolved H2AX and γ-H2AX 4Pi signal of a single cell for the *z* and the *y*-direction, respectively. The much broader curve for γ-H2AX (filled markers) compared to H2AX (open markers) in both panels represents the larger correlation range in this channel indicating the larger size of γ-H2AX clusters. Due to the higher resolution in the *z*-direction, this effect can be seen more clearly in this direction (**a**) than for the *y*-direction (**b**). The shift values Δx, Δy and Δz for which the normalized autocorrelation function has dropped to 0.5 ("autocorrelation width"), as indicated by the arrows in **a**, are extracted for each recorded cell and displayed as data points in panel **c** and **d** for H2AX and γ-H2AX, respectively. The lines in **c** and **d** represent the average over the three cells measured at each time point. The data in **c** and **d** clearly shows that while H2AX clusters do not change in size on average after IR, γ-H2AX cluster sizes increase, reaching a plateau after approximately 90 min. This effect is most pronounced when looking at the *z*-direction, where the increased resolution of 4Pi microscopy can be exploited.

diameter connects the autocorrelation width to the real size of sphere-like solid objects.

**Spatial Distribution Analysis.** The three channels of confocal 3D raw data were loaded into the program Imspector. Single non-dividing cells that did not show obvious staining artifacts were manually cut out of the data set and saved separately (see Fig. 7.3a-c as examples). A user-written algorithm programmed in "C" was applied that processed the data according to the following steps:

1. The shift between adjacent *x*-lines in the data sets due to improper adjustment between the forward and backward scan of the bidirectional recording mode was corrected automatically. To achieve this, the cross-correlation between the voxel values with an even *y*-voxel coordinate and an odd one was calculated along the *x*-direction for the H2AX channel. Since the physical distance between adjacent *x*-lines is below the lateral resolution limit of the microscope and the H2AX signal featured large numbers of small structures, the voxel shift position of the maximum in the cross-correlation curve is a good measure for the shift between the data of the two scan directions. By shifting the data in every *x*-line with an odd *y*-voxel position for all channels by this value, this mismatch could be corrected to sub-voxel accuracy.
2. The DAPI channel was smoothed in all three dimensions with a normalized Gaussian-shaped filter ($N \times \exp(-x^2/2\,\sigma^2)$ with $\sigma = 2$ voxel lengths) and the first mask delimiting the 3D volume of the nucleus was created by thresholding the smoothed DAPI signal at 35% of its maximum (mask value = 1 for signals > 35%, else 0).
3. In order to close holes in the mask, for example for nucleoli that feature lower DAPI signals, the mask was dilated twice. In each dilation iteration, for each voxel in the mask with value "1"

all voxels closer than 400 nm were also set to "1". This was followed by two erosion iterations, where around each voxel with a value equal to zero, all voxels within 400 nm radius where also set to zero. This way, the outer shape of the original mask was largely conserved, but holes in the mask smaller than 1600 nm diameter disappeared.

4. Starting from this mask ("mask 0"), the mask was iteratively eroded in 400 nm steps until it disappeared completely. The total signal in the H2AX and γ-H2AX channels within the mask of each of the intermediate steps and for voxel values above 20 counts (equivalent to about 10% of the maximum counts) was stored, as well as the number of voxels in each mask.

The results of the cells of each time point were compiled in Microsoft Excel. Signal densities or average intensities were calculated by dividing the signal within each mask by the mask's volume. The signal densities were background-corrected by subtracting $(S_{tot}\text{-}S_0)/(V_{tot}\text{-}V_0)$, where $S_{tot}$ and $S_0$ are the total signals of the whole data set and in "mask 0", respectively, and $V_{tot}$ and $V_0$ are the corresponding volumes. Figures 7.3 and 7.7 display these values for each mask averaged over all cells of one population as well as the ratio between the γ-H2AX and the H2AX signal density.

**FIGURE 7.7**

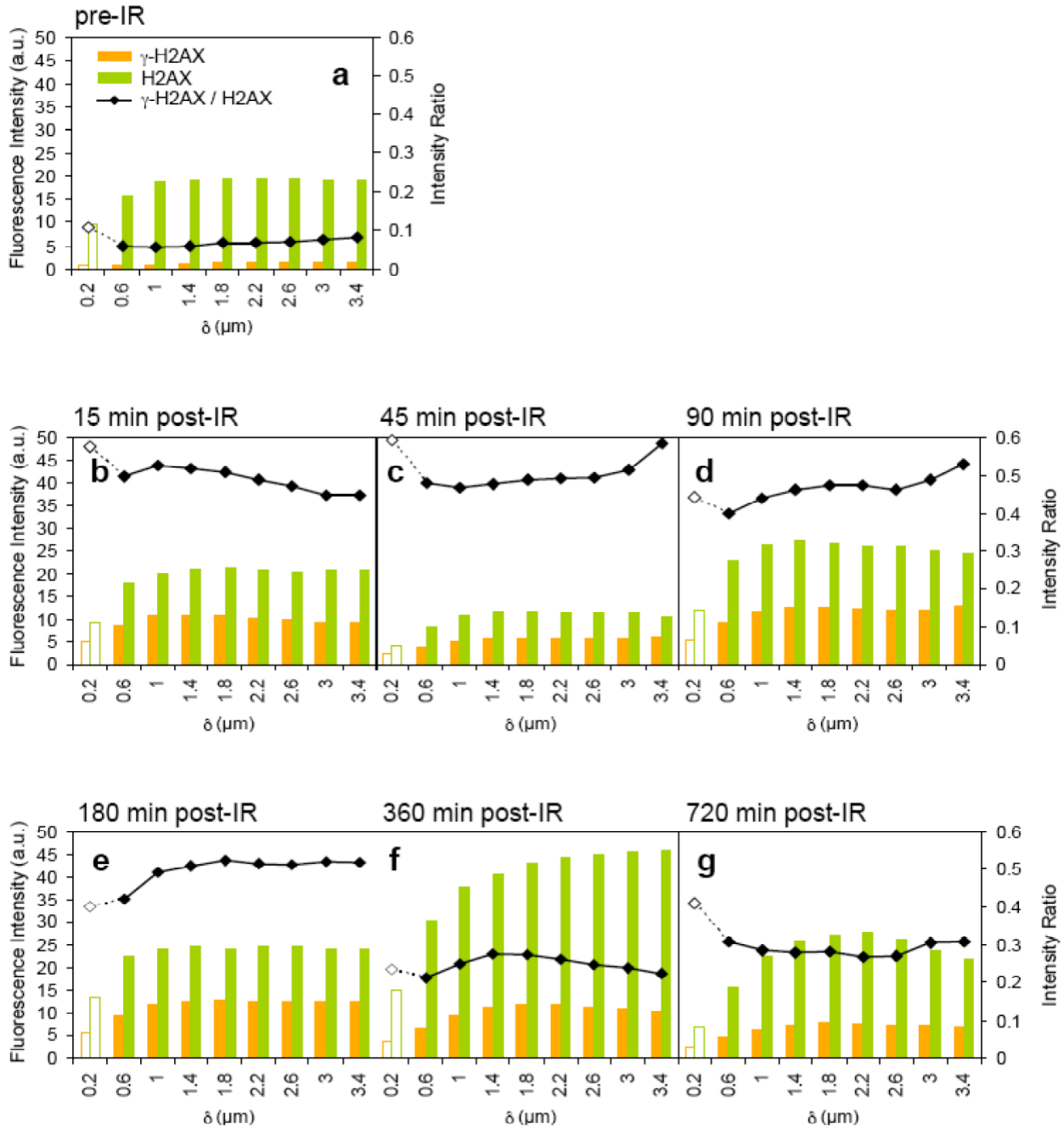
pre-IR
γ-H2AX
H2AX
γ-H2AX / H2AX
a
Fluorescence Intensity (a.u.)
Intensity Ratio
δ (μm)
15 min post-IR
45 min post-IR
90 min post-IR
b
c
d
180 min post-IR
360 min post-IR
720 min post-IR
e
f
g

**Figure 7.7 - Complete set of spatial distribution analyses for cells at all time points following IR treatment.** As in Fig. 7.3 (**g-i**), each histogram displays the fluorescence intensity for the H2AX (green) and γ-H2AX (red) channels, and the γ-H2AX/H2AX intensity ratio within each 400 nm thick shell-like mask as a function of distance (δ) from the nuclear periphery. An inherent ambiguity in precisely identifying the nuclear boundary using the smoothed DAPI threshold gives rise to some uncertainty in fluorescence intensity localization within the first 400 nm shell, indicated by the open histogram bars and intensity ratio at 0.2 μm.

**FIGURE 7.8**

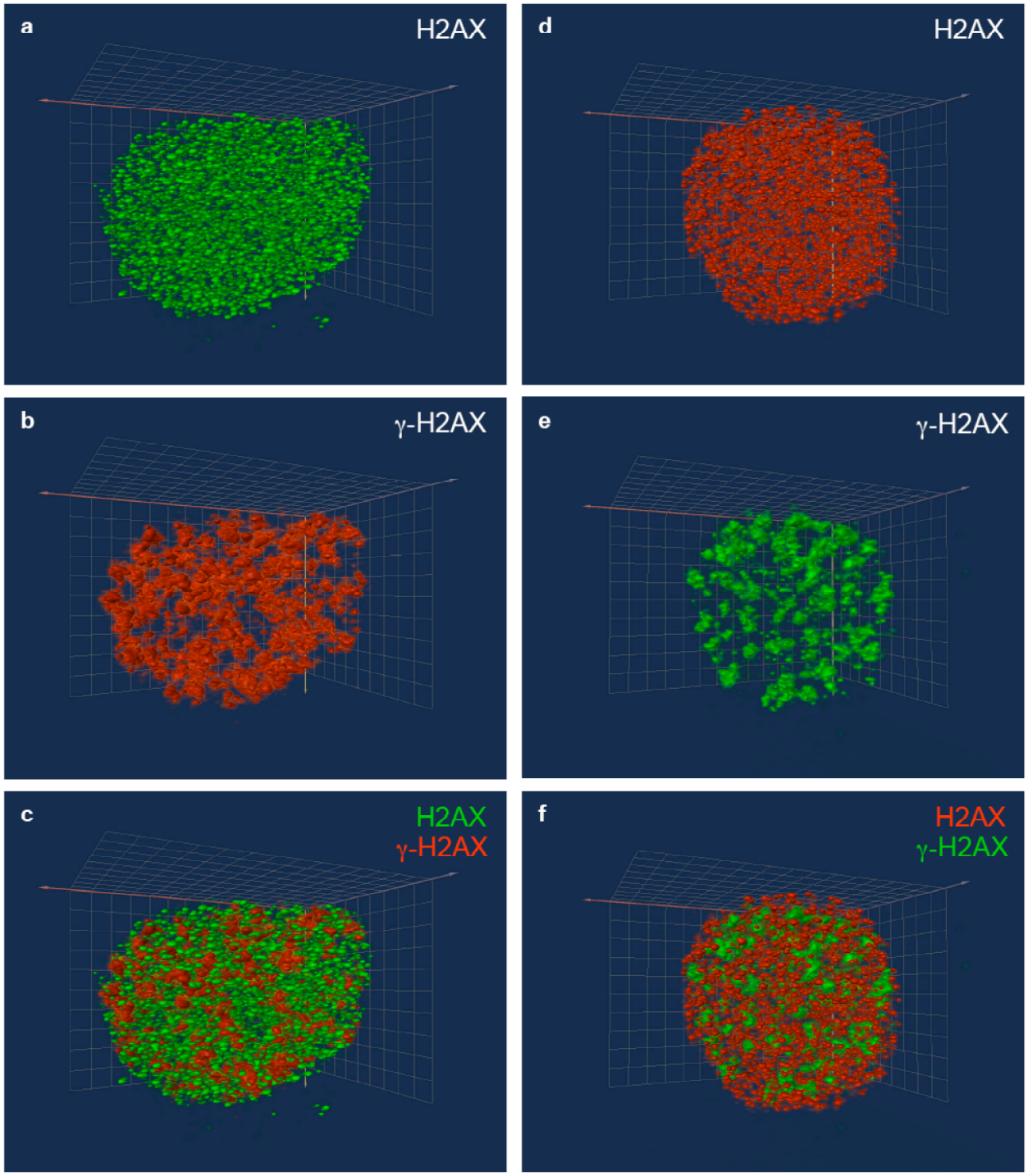

**Figure 7.8 - Authenticity of the appearance for H2AX and γ-H2AX clusters.** To eliminate the small possibility that our choice of secondary antibody-conjugated fluorophores may influence the appearance of the staining patterns observed, we switched the secondary antibodies used to visualize both H2AX and γ-H2AX clusters. Cells were exposed to 3 Gy IR and grown for 180 min before fixation. (**a-c**) Nucleus in which γ-H2AX was stained using a mouse monoclonal antibody and Rhodamine Red-X goat anti-mouse secondary antibody and H2AX was stained using a rabbit polyclonal antibody and an Alexa Fluor 488 goat anti-rabbit secondary antibody. (**d-f**) Nucleus in which γ-H2AX was stained using a mouse monoclonal antibody and Alexa Fluor 488 goat anti-mouse secondary. Subsequently, H2AX was stained using a rabbit polyclonal antibody and Rhodamine Red-X goat anti-rabbit secondary antibody. Thus, the cluster sizes and distribution are unaffected by the use of different secondary antibody conjugates.

# Chapter VIII

## FINAL DISCUSSION and FUTURE DIRECTIONS

The work presented in this thesis provides new and in some cases provocative information about the cellular localization of Rad51, Rad51C and Xrcc3 in human cells. It also addresses the dynamics of the cellular re-distribution of these proteins in response to DNA damage, and importantly we have discovered an unexpected function for Rad51C. The cellular imaging work was inspired in part by a re-evaluation of the immunofluorescence images and methods that appeared in the DNA repair literature. During the course of this research I came to appreciate that strict control of experimental parameters and verification of reagent specificity is especially important in a field of study in which the observations can easily be misinterpreted by virtue of the extreme sensitivity of the methods and technology employed. In review of what has been accomplished thus far we have found the following.

In Chapter II, we reported for the first time using immunofluorescence that endogenous Xrcc3 forms distinct nuclear foci both before and after DNA damage. While we also saw the protein to be equally cytoplasmic, we were not prepared at that time to discuss the relevance of this observation as Rad51 and its paralogs had been reported to be exclusively nuclear. We also reported that the RNAi-mediated knockdown of Rad51 had no affect on the localization of Xrcc3. Finally, although we reported that some Xrcc3 foci colocalize to gamma H2AX within 10 minutes of induction of DNA damage, I would offer now that we know that neither Rad51, Rad51C nor Xrcc3 colocalize or show coincidence to gamma H2AX (Chapter V, and see below).

In Chapter III, I show how problems with immunofluorescence data that arise from the use of non-specific antibodies were resolved. The data describe an effective antibody purification scheme and how this eliminated non-specific bands seen in Western blots as well as removal of background or non-specific staining by immunofluorescence. This was an important step in our approach to data collection in Chapter IV.

In Chapter IV, not only do we identify for the first time a specific biological function for a Rad51 paralog protein, Rad51C, we also employed our strategy of antibody purification and specificity controls. This was the first paper in our field to unequivocally demonstrate antibody specificity showing target-specific RNAi depletion of protein signal by both Western blot and immunofluorescence. A surprising and novel biological outcome was also realized in that experiments designed to test the interdependency of Rad51, Rad51C and Xrcc3 localization revealed that Rad51C regulates ubiquitin–mediated proteolysis of Rad51.

In Chapter V, we further explored the question of colocalization (more properly referred to as coincidence) of HR proteins to gamma H2AX. We demonstrate that the method of application of antibodies to fixed cells can have a significant impact on the staining patterns observed. For example, the data strongly support the idea that Rad51 does not colocalize with gamma H2AX, and that many published accounts of their coincidence result simply from using an inappropriate method of antibody application.

In Chapter VI we use sub-cellular fractionation and Western blots to corroborate our immunofluorescence data showing distinct and reproducible patterns of protein re-localization in

response to DNA damage in various human cell lines. We also show initial studies of the Brca2 protein and its affect on the cellular localization patterns of Rad51, Rad51C and Xrcc3.

Chapter VII describes the first successful use of 4Pi microscopy to visualize endogenous nuclear proteins. Imaging of histones H2AX and γ-H2AX revealed novel chromatin structures (clusters) that support a model in which these clusters serve to limit the 1-2 Mbp spreading γ-H2AX away from the site of a DNA break, and serve as pre-existing platforms to generate a rapid and response observed immediately following DNA damage.

Below, I present a model that summarizes some of the findings of my work, focusing on potential interactions among the Rad51, Rad51C, Xrcc3 and Brca2, and how disruption of any of these may lead to deleterious alterations in cellular localization and function.

**FIGURE 8.1**

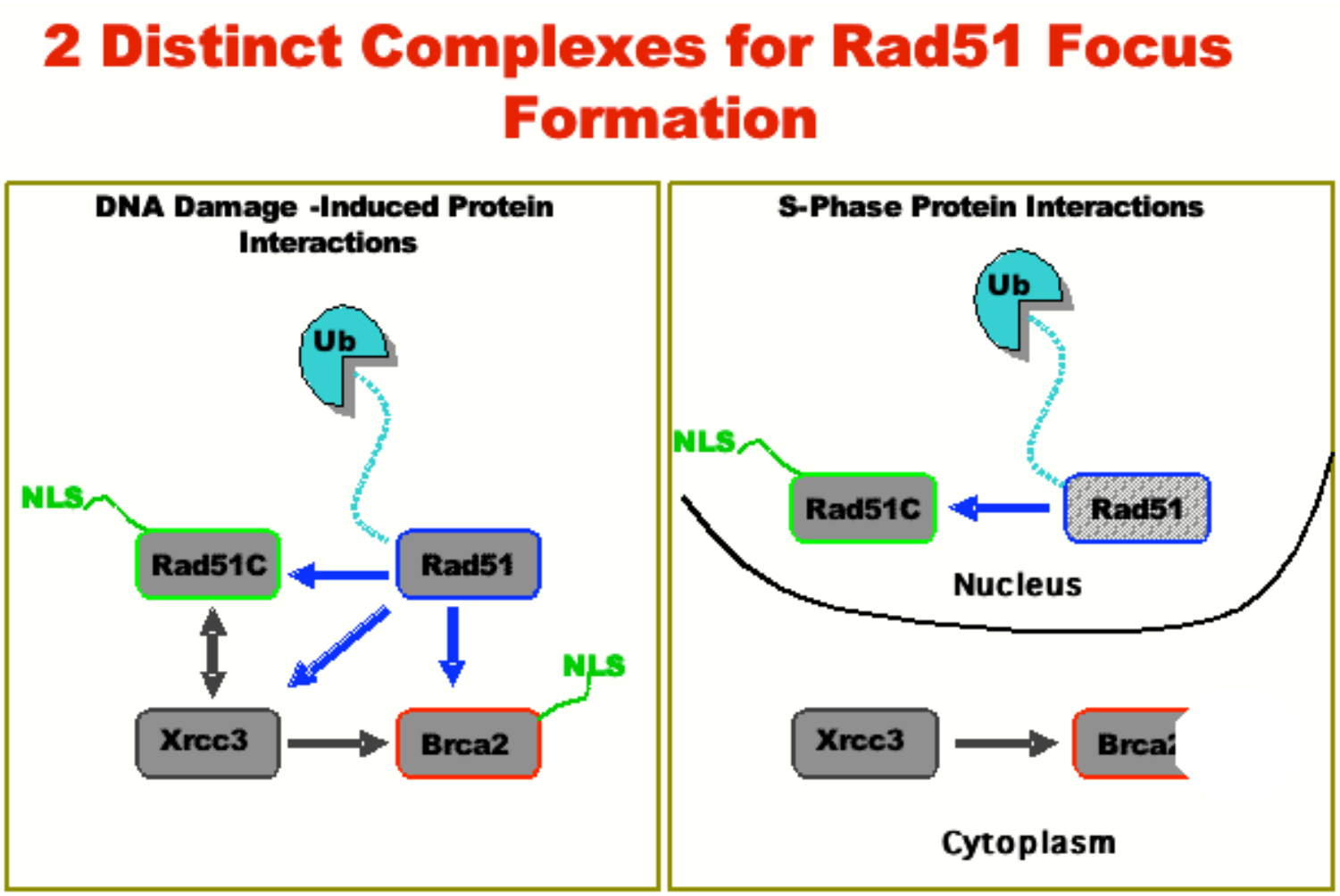
2 Distinct Complexes for Rad51 Focus Formation
DNA Damage -Induced Protein Interactions
Ub
NLS
Rad51C
Rad51
Xrcc3
Brca2
NLS
S-Phase Protein Interactions
Ub
NLS
Rad51C
Rad51
Nucleus
Xrcc3
Brca2
Cytoplasm

**Figure 8.1 - Rad51 uses different complex associations for basal nuclear entry vs. DNA damage-induced nuclear entry.** Interaction of Rad51 with Brca2 is important for nuclear entry following DNA damage (left), while Rad51C's interaction with Rad51 may serve to transport Rad51 into the nucleus under non-damage conditions, thus promoting formation of S-phase Rad51 nuclear foci (right). The latter pathway can occur in the absence of Xrcc3 and without a functional Brca2.

**DNA damage-induced protein interactions**

The model in Figure 8.1 demonstrates the dependence of Rad51 on Brca2 in DNA damage induced foci formation. Further demonstrated is Rad51's dependence on Xrcc3 and Rad51C for focus formation and the necessity for Rad51C to inhibit ubiquitin-mediated proteolysis of Rad51. Additionally, we speculate that Xrcc3's interaction with Brca2 is necessary for both pre- and post-damage Xrcc3 focus formation. Although is has been reported that Xrcc3 and Rad51C exist in the cell as a stable heterodimer, our results in Chapter IV clearly demonstrate separate functions for the two proteins. Additionally, our immunofluorescence data (Chapters II, IV and VI) support the idea that each protein can exist independently within in the cell. Thus, the double ended arrow indicates that their interaction may be more of a transient association than currently appreciated.

**Rad51 forms S-Phase foci by an alternative sub-complex in the absence of Brca2**

The model in Figure 8.1 also shows that in a Brca2 deficient cell line, e.g. Capan-1 pancreatic cancer cells, Rad51 still possesses the capacity to form S-phase foci. Given the absence of the nuclear localization sequences in the truncated Brca2 protein present in Capan-1 cells, Rad51 loses the ability to form DNA damage induced foci. This suggests an alternate mechanism for Rad51 nuclear entry and focus development. While the absence of Brca2 negatively effects Xrcc3's ability to localize to the nucleus (Xrcc3 demonstrates predominantly cytoplasmic staining, see Chapter VI), it has little to no affect on nuclear localization of Rad51C. Further, Rad51C forms both pre- and post-damage foci in the absence of Brca2 suggesting that Rad51C, through its direct interaction with Rad51, provides an alternate mechanism for Rad51 nuclear

entry. Additionally, persistence of the stable association of Rad51C with Rad51 in the absence of a functional Brca2 protein prevents ubiquitin-mediated proteolysis of Rad51.

In the remaining pages of this thesis, I will take the opportunity to outline 2 future directions of research, which have already begun. I offer new data that supports some of our recent findings, describe how the work may impact immunofluorescence methods in general, and how it will contribute to a developing model of the regulation and function of homologous recombinational repair proteins in human cells.

**Future Direction 1 – The Reality and Relevance of Coincident Staining of Proteins Involved in DNA Repair.** While our data show that Rad51 does not show a significant level of coincidence with gamma H2AX following DNA damage (preliminary work suggests the same for Rad51C and Xrcc3), it is our hypothesis that these 3 DNA repair proteins participate in highly dynamic and transient interactions in both the cytoplasm and nucleus. Therefore, we have initiated studies to look at possible coincident staining of the Rad51 and Rad51C, as well as Rad51 and Xrcc3 before and during a time course of DNA repair. Included in this analysis will be a more quantitative measure of protein coincidence than we have used previously. This is demonstrated in Figure 8.2. Two hr following exposure to ionizing radiation HEK293 cells were stained sequentially (row A) with a purified polyclonal against HsRad51 then an anti rabbit Alexa 488 conjugate (green), followed by application of a monoclonal antibody directed against gamma H2AX, then an anti mouse Alexa 647 conjugate (red). The 3$^{rd}$ panel is a merge of the 2 channels while the final panel shows a quantitative measure of the localization and intensity of each signal (cytofluorogram). The cytofluorogram signal along the Y axis is that of gamma

**FIGURE 8.2**

**Quantification of coincident staining for HsRad51 and γH2AX by cytofluorogram**

**2 hrs post 8 Gy IR**

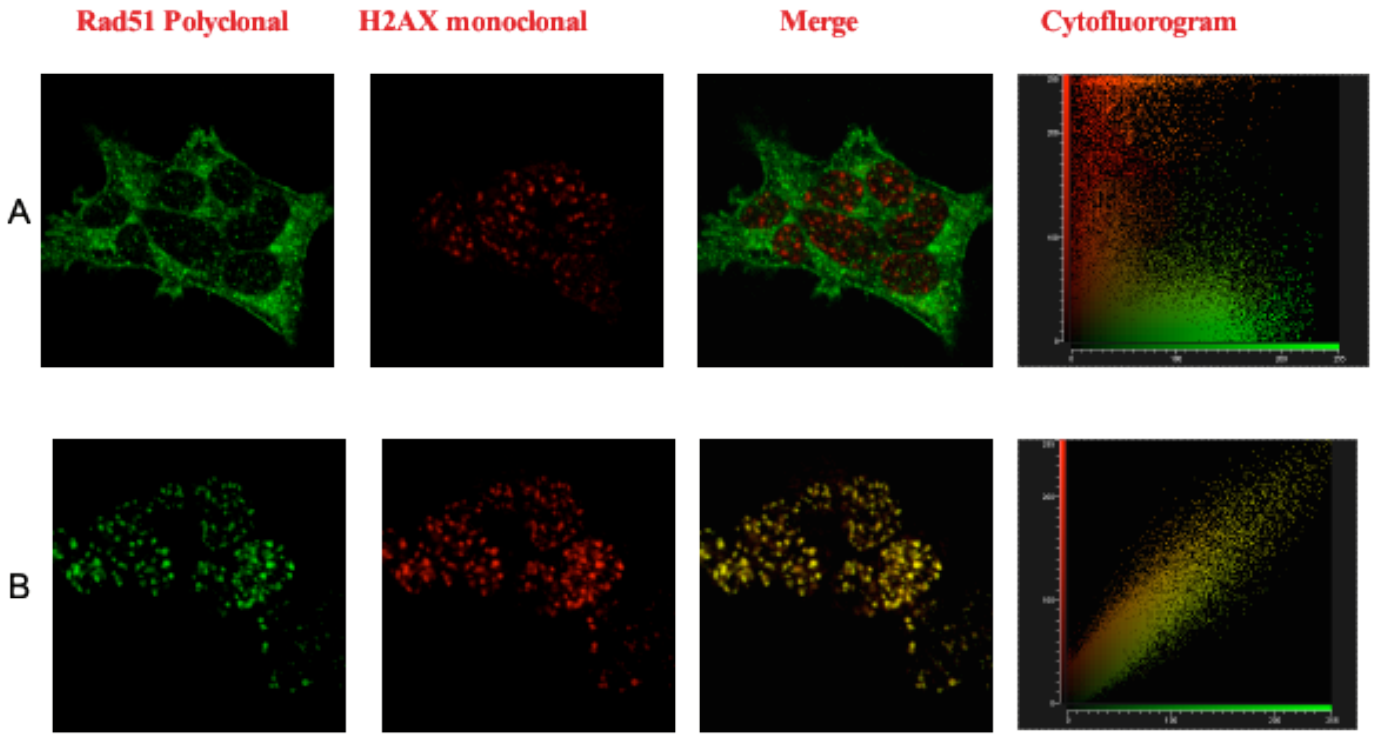

**Figure 8.2 – Quantification of coincident staining for Rad51 and gamma H2AX 2 hours post 8 Gy ionizing radiation.** HEK293 cells were sustained, damaged, fixed and immunostained as previously described. Panels A and B, moving from right to left are staining against Rad51 (green), gamma H2AX (red) and a merge of the two channels. The final panel, far left, is a cytofluorogram which demonstrates the joint distribution of pixel intensities for each channel.

H2AX (red) and that along the X axis is Rad51 (green). Any signal that lies along the 45 degree diagnol represents pixels that share signal from each channel individually, and in row A this area is largely unoccupied.

Therefore, the cytofluorogram supports the merge image in which little to no coincident staining for these two proteins is observed [note that the merge image in row A was featured on the cover of J. Cell. Biochem. 2005 Dec 15; 96(6)]. In row B, we have repeated our use of an antibody cocktail for staining as described in Chapter V. In this case the cytofluorogram shows nearly perfect coincidence of pixel values in the two channels. While it would be my hope that any image demonstrating coincidence to this degree would be questioned regarding its authenticity, i.e. it's too good to be true, we make it clear in Chapter V that this result is an artifact of the use of an antibody cocktail. Note that the fluorophores chosen for these experiments have no overlap in their emission and excitation spectra. Beyond cytofluorogram data it is the aim of this research to collect Z-series, 3-D renderings, of spatial localization for all three proteins with possible coincident partner proteins.

Toward this, in Figure 8.3 I show preliminary data demonstrating that the plane and angle of image reconstruction plays a part in claims of coincident staining. This shows a 112 series Z-stack (3-D) that has been rendered a maximum projection for the sake of 2-D presentation. The maximum projection is an image in which the maximum voxel (3-D pixel) values are determined along the chosen axis (throughout the Z stack) and displayed in a 2-D format.

**FIGURE 8.3**

**Maximum projection of Xrcc3 and γH2AX following treatment with IR**

**(separation of signal)**

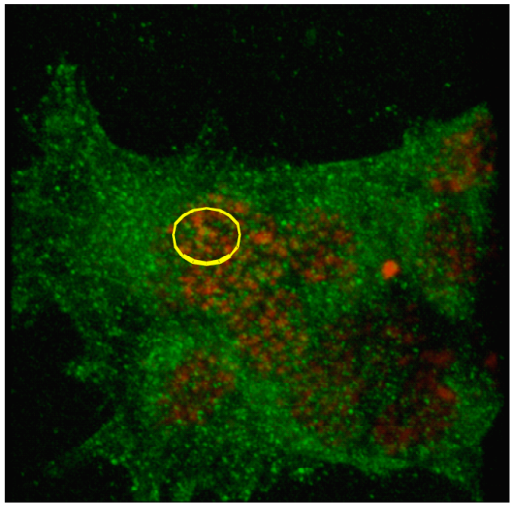

Circle indicates whereby cytofluorogram, at this angle we have equal voxel intensity values for both channels

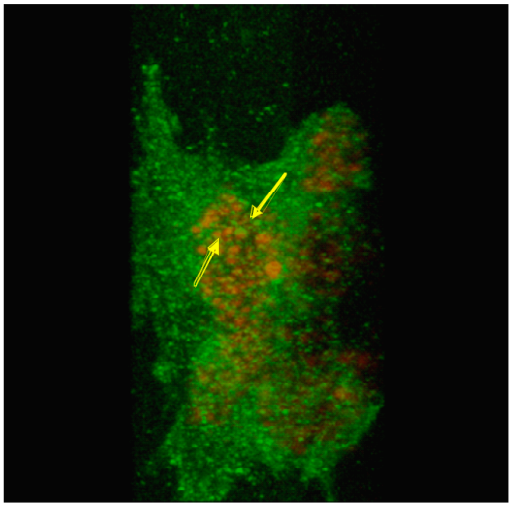

Arrows indicate that when this image is rotated and again put into maximum projection the voxel intensities are separated and there are two separate foci

**Figure 8.3 – Maximum projection of Xrcc3 and gamma H2AX demonstrates coincidence and subsequent separation of signal and/or coincidence.** HEK293 cells were sustained, damaged, fixed and immunostained as previously described. The two images shown represent the same cell shown in a maximum projection (122 slice, 3 dimensional Z-series). Green staining is that of Xrcc3 where red is that of gamma H2AX. Right hand panel shows coincident staining for both channels (confirmed by voxel cytofluorogram, data not shown) while the left panel is the same image rotated 180 degrees. The later image shows that, in fact, the signal of the two separate channels was some distance apart.

Here we are visualizing 112 plains compressed into a 2-D rendering, thus the image looks busy and dirty. The data was analyzed in 3-D for evidence of coincident staining and the renderings in this figure show a 90 degree rotation displaying the same foci from different plains within the image. The left panel has an encircled area in which there are examples of data showing that voxel intensities for both channels are equal. However when we rotate the image 90 degrees and again made a maximum projection, it is clear that coincidence is no longer apparent (indicated by arrows). Therefore, these data show that coincident staining can also arise simply by how a stained image is viewed. While this may seem a simple technical issue, it is remarkable how many manuscripts claim co-localization from single 2-D images without further analysis. This work will be enhanced by employing FRET and 4Pi methods (see below).

Our initial efforts to test for coincident staining of Rad51/Rad51C and Rad51/Xrcc3 pairs are shown in Figure 8.4. HEK293 cells were grown for 2 hr after exposure to 10 Gy ionizing radiation and stained sequentially with a monoclonal antibody against either Rad51C (A) or Xrcc3 (B) followed by a polyclonal antibody against Rad51. Clearly, these images show distinct Rad51C and Xrcc3 nuclear foci that do not co-localize with Rad51. This is interesting because both Rad51 paralog proteins have been shown to interact with Rad51, and the Rad51/Rad51C interaction is enhanced in the presence of Xrcc3 (Schild et al., 2000). In contrast to the nucleus, there appears to be a significant amount of coincident staining of both protein pairs in the cytoplasm. While this interpretation must be tempered given the apparent protein clustering in this region, use of Z stacks and 3-D imaging will help resolve this ambiguity.

**FIGURE 8.4**

**A**

**Co Staining of HsRad51 and HsRad51C 2 Hours Post 10Gy Ionizing Radiation**

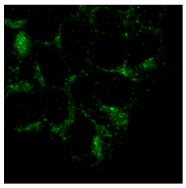

anti – HsRad51C monoclonal/ Alexa 488

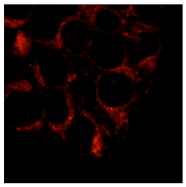

anti – HsRad51 polyclonal/ Alexa 647

- Nuclear Rad51 and Rad51C foci are independent spatially from one another
- Cytoplasmic Rad51 and Rad51C demonstrate a high level of coincident staining.

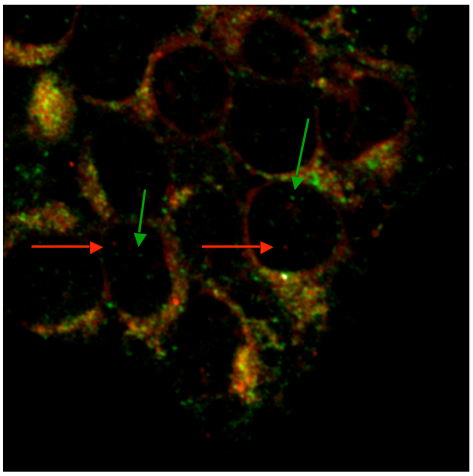

Green arrow shows Hs**Rad51C** foci

Red arrow shows HsRad51 foci

**B**

**Co Staining of HsRad51 and HsXrcc3 2 Hours Post 10Gy Ionizing Radiation**

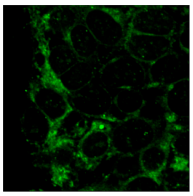

anti – HsXrcc3 monoclonal/ Alexa 488

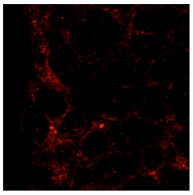

anti – HsRad51 polyclonal/ Alexa 647

- Nuclear Rad51 and Xrcc3 foci are independent spatially from one another
- Cytoplasmic Rad51 and Xrcc3 demonstrate a high level of coincident staining.

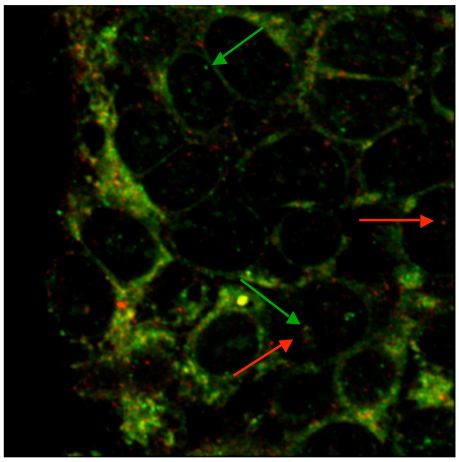

Green arrow shows HsXrcc3 foci

Red arrow shows HsRad51 foci

**Figure 8.4 The protein pairs Rad51/Rad51C and Rad51/Xrcc3 show coincident staining in the cytoplasm but not the nucleus 2 hours after DNA damage.** HEK293 cells were fixed and stained as described 2 hr following exposure to 10 Gy IR. Sequential staining for Rad51/Rad51C (A) and Rad51/Xrcc3 was performed as described (Chapter V) using the antibodies indicated. Red and green arrows indicate nuclear foci that do not coincide.

Other than the monoclonal antibodies against Rad51C and Xrcc 3 used here, there are currently no polyclonal antibodies available for either protein, thus precluding co-localization studies. One of my goals is to develop anti-Rad51C and Xrcc3 antibodies for this purpose. Further studies will examine all pairs as a function of time after DNA damage in an attempt to discern possible transient interactions. RNAi studies similar to those described in Chapter IV (Bennett and Knight, 2005) will be used to dissect the dependency of possible pair-wise interactions on the other protein, e.g. does cytoplasmic coincidence of Rad51C and Rad51 depend on Xrcc3. In addition to FRET and 3D analysis of layered immunofluorescent images mentioned above, as well as 4Pi microscopy (see below), we will also use sub-cellular fractionation and immunoprecipitation methods to follow the distribution and localization of Rad51C, Xrcc3 and Rad51 throughout the time course of DNA damage and repair (see Chapter VI).

**Future Direction 2 – Mechanism and Regulation of Rad51, Rad51C and Xrcc3 Trafficking in Response to DNA Damage**. In addition to verifying the DNA damage-dependent formation of Rad51 nuclear foci, we have shown that significant levels of Rad51 exist in the cytoplasm before and after DNA damage. Additionally, we find that Rad51C and Xrcc3 form distinct foci in both the cytoplasm and nucleus before and after DNA damage. In new data shown below, we find that cytoplasmic Rad51 associates with cytoskeletal proteins. In a continuation of this work, we will test 2 hypotheses: 1. that the pre-damage Rad51C and Xrcc3 foci may assist in Rad51's movement to the nucleus and/or deposition at a DNA break following DNA damage and; 2. that Rad51 and possibly Rad51C and Xrcc3 may utilize microtubules as a means of trafficking in response to DNA damage. As described in Chapter VI, while published data suggests that the interaction of Brca2 and Rad51 accounts for the nuclear localization of Rad51 following damage,

our data strongly supports the presence of a Brca2-independent pathway for cytoplasmic-nuclear shuttling in response to DNA damage.

The significant cytoplasmic signal we observe for Rad51, Rad51C and Xrcc3 suggested that each protein may interact with the cytoskeletal architecture and exploit this association as a potential mechanism for cytoplasmic-nuclear trafficking in response to DNA damage. In addition to their role in cellular architecture and dynamics, microtubules have gained notice for their direct role in cytoplasmic-nuclear of various proteins (Giannakakou et al., 2002; Gundersen and Cook, 1999; Lam et al., 2002; Pockwinse et al., 2005; Roczniak-Ferguson and Reynolds, 2003; Ziegelbauer et al., 2001). Therefore, we analyzed the possible association of Rad51 with tubulin. Figure 8.5 demonstrates that staining of Rad51 and beta tubulin share a high coincidence in the cytoplasm. Rad51 (green) and beta tubulin (red) appear in punctuate foci throughout the cytoplasm and yellow seen throughout the cytoplasm represents possible areas of coincidence (blue is gamma H2AX and indicates cells have beem exposed to ionizing radiation). While the high level of coincident staining is intriguing we note that beta tubulin is not in its typical fibrillar form. This is consistent with other studies showing that exposure of cells to DNA damaging agents can disrupt the microtubules network (Zamansky et al., 1991; Zamansky et al., 1992). Careful time courses and dose responses will be required to understand the functional relevance of the interactions between DNA repair and cytoskeletal proteins.

**FIGURE 8.5**

## Rad51 association with beta-tubulin in HEK293 cells following exposure to 8 Gy IR

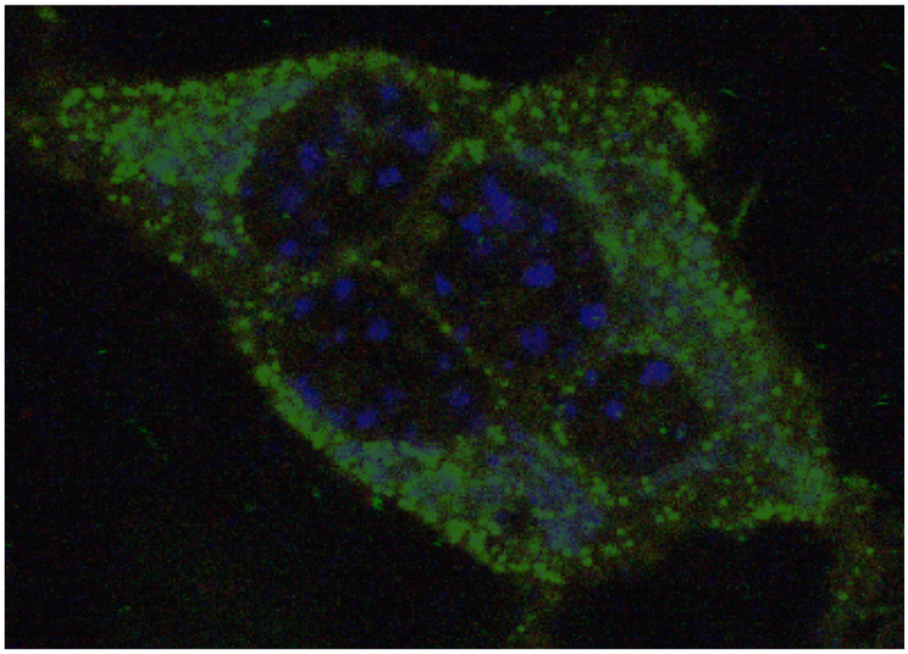

**Figure 8.5 – Rad51 association with beta tubulin following DNA damage.** HEK293 cells were sustained, damaged, fixed and stained as previously described. Rad51 polyclonal antibody was applied first in a sequential staining methodology followed by a beta tubulin-directed monoclonal, and finally a biotin conjugated antibody directed against gamma H2AX. Secondary antibodies were anti rabbit Alexa 488 (green), anti mouse Alexa 647 (red) and streptavidin Alexa 405 (blue). Areas of yellow staining represent possible coincidence for Rad51 and beta tubulin.

A promising technical advance now available to us is 4Pi microscopy. Our first use of 4Pi to image endogenous nuclear proteins in human cells, as well as a description of the technology, is presented in Chapter VII. I have also begun 4Pi investigations of microtubule proteins given that my initial confocal images suggested an association with cytoplasmic Rad51. Figure 8.6 demonstrates the difference in resolution between standard confocal and 4Pi microscopy. The upper left panel shows an image of HEK293 cells stained with an anti human alpha tubulin primary and Alexa 488 secondary imaged using standard confocal microscopy. An image of the same cell was then collected using a second opposing objective, the addition of multiphoton excitation and calculation of the resolution by analysis of the point spread function. The upper right hand image shows this raw data set. Below the cell on the lower cover slip are 100nm beads, used as standards to assist with image deconvolution. The lower left panel is the same image after being run though the linear filter. This image represents 512 individual slices in an average projection (using the average voxel intensity through the given plain) with a step size of 26 nm. Notice that the beads no longer show the side lobes, with their spherical shape indicating the increase in collection of the maximal spherical wavefront.

I have collected 3-D movies of these cells in which significantly more detail is seen than previously available. It is with this new methodology that we will further our exploration of the cellular dynamics of Rad51 and associated proteins and move toward what I have termed, “visual cellular biochemistry”.

FIGURE 6.1

**Re-distribution of cellular Rad51 in response to ionizing radiation**

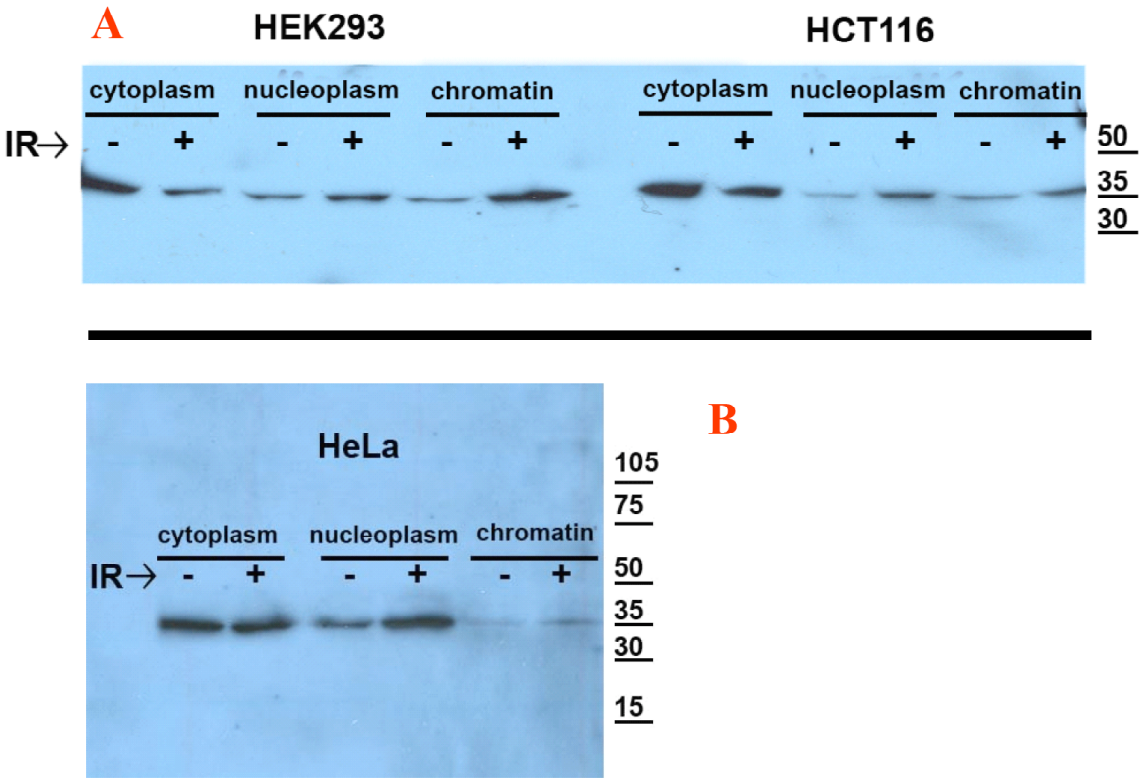

**Figure 8.6 – Imaging of alpha tubulin and comparison of conventional confocal microscopy vs. 4Pi.** HEK293 Cells were sustained, plated, grown, fixed and mounted by a licensed method. Upper left hand panel shows HeLa cell stained with an anti alpha tubulin primary followed by an anti mouse Alexa488. In the lower plain of the image we see 100 nm beads with an Alexa488 conjugated to the surface. This image was taken by standard confocal microscopy technique. The upper right hand panel shows a raw 4Pi image of the dame cell, noting the side lobes as an indicator of point spread function and resolution. The lower left hand image is a 4Pi image after being deconvolved. The absence of the side lobes indicates a final resolution of approximately 100 nm by referencing the 100 nm beads.

# REFERENCES

Albala, J. S., Thelen, M. P., Prange, C., Fan, W., Christensen, M., Thompson, L. H., and Lennon, G. G. (1997). Identification of a novel human RAD51 homolog, RAD51B. Genomics *46*, 476-479.

Aten, J. A., Stap, J., Krawczyk, P. M., van Oven, C. H., Hoebe, R. A., Essers, J., and Kanaar, R. (2004). Dynamics of DNA double-strand breaks revealed by clustering of damaged chromosome domains. Science *303*, 92-95.

Bekker-Jensen, S., Lukas, C., Melander, F., Bartek, J. and Lukas, J. (2005) Dynamic assembly and sustained retention of 53BP1 at the sites of DNA damage are controlled by Mdc1/NFBD1. J Cell Biol *170*, 201-211.

Bennett, B. T., and Knight, K. L. (2005). Cellular localization of human Rad51C and regulation of ubiquitin-mediated proteolysis of Rad51. J Cell Biochem *96*, 1095-1109.

Bhattacharyya, A., Ear, U. S., Koller, B. H., Weichselbaum, R. R., and Bishop, D. K. (2000). The breast cancer susceptibility gene BRCA1 is required for subnuclear assembly of Rad51 and survival following treatment with the DNA cross-linking agent cisplatin. J Biol Chem *275*, 23899-23903.

Bischof, O., Kim, S. H., Irving, J., Beresten, S., Ellis, N. A., and Campisi, J. (2001). Regulation and localization of the Bloom syndrome protein in response to DNA damage. J Cell Biol *153*, 367-380.

Bishop, D. K., Ear, U., Bhattacharyya, A., Calderone, C., Beckett, M., Weichselbaum, R. R., and Shinohara, A. (1998). Xrcc3 is required for assembly of Rad51 complexes in vivo. J Biol Chem *273*, 21482-21488.

Bleuyard, J. Y., and White, C. I. (2004). The Arabidopsis homologue of Xrcc3 plays an essential role in meiosis. EMBO J *23*, 439-449.

Bouquet, F., Muller, C. and Salles, B. The Loss of gammaH2AX Signal is a Marker of DNA Double Strand Breaks Repair Only at Low Levels of DNA Damage. Cell Cycle *5*, 1116-1122.

Braybrooke, J. P., Spink, K. G., Thacker, J., and Hickson, I. D. (2000). The RAD51 family member, RAD51L3, is a DNA-stimulated ATPase that forms a complex with XRCC2. J Biol Chem *275*, 29100-29106.

Brenneman, M. A., Weiss, A. E., Nickoloff, J. A., and Chen, D. J. (2000). XRCC3 is required for efficient repair of chromosome breaks by homologous recombination. Mutat Res *459*, 89-97.

Canitrot, Y., Capp, J. P., Puget, N., Bieth, A., Lopez, B., Hoffmann, J. S., and Cazaux, C. (2004). DNA polymerase beta overexpression stimulates the Rad51-dependent homologous recombination in mammalian cells. Nucleic Acids Res *32*, 5104-5112.

Cartwright, R., Dunn, A. M., Simpson, P. J., Tambini, C. E., and Thacker, J. (1998). Isolation of novel human and mouse genes of the recA/RAD51 recombination-repair gene family. Nucleic Acids Res *26*, 1653-1659.

Chen, F., Nastasi, A., Shen, Z., Brenneman, M., Crissman, H., and Chen, D. J. (1997). Cell cycle-dependent protein expression of mammalian homologs of yeast DNA double-strand break repair genes Rad51 and Rad52. Mutat Res *384*, 205-211.

Chen, J., Silver, D. P., Walpita, D., Cantor, S. B., Gazdar, A. F., Tomlinson, G., Couch, F. J., Weber, B. L., Ashley, T., Livingston, D. M., and Scully, R. (1998). Stable interaction

between the products of the BRCA1 and BRCA2 tumor suppressor genes in mitotic and meiotic cells. Mol Cell *2*, 317-328.

Chen, J. J., Silver, D., Cantor, S., Livingston, D. M., and Scully, R. (1999). BRCA1, BRCA2, and Rad51 operate in a common DNA damage response pathway. Cancer Res *59*, 1752s-1756s.

Chowdhury, D., Keogh, M. C., Ishii, H., Peterson, C. L., Buratowski, S. and Lieberman, J. (2005) gamma-H2AX dephosphorylation by protein phosphatase 2A facilitates DNA double-strand break repair. Mol Cell *20*, 801-809.

Conway, A. B., Lynch, T. W., Zhang, Y., Fortin, G. S., Fung, C. W., Symington, L. S., and Rice, P. A. (2004). Crystal structure of a Rad51 filament. Nat Struct Mol Biol *11*, 791-796.

Daboussi, F., Dumay, A., Delacote, F., and Lopez, B. S. (2002). DNA double-strand break repair signalling: the case of RAD51 post-translational regulation. Cell Signal *14*, 969-975.

Davies, A. A., Masson, J. Y., McIlwraith, M. J., Stasiak, A. Z., Stasiak, A., Venkitaraman, A. R., and West, S. C. (2001). Role of BRCA2 in control of the RAD51 recombination and DNA repair protein. Mol Cell *7*, 273-282.

Dong, Z., Zhong, Q., and Chen, P. L. (1999). The Nijmegen breakage syndrome protein is essential for Mre11 phosphorylation upon DNA damage. J Biol Chem *274*, 19513-19516.

Dosanjh, M. K., Collins, D. W., Fan, W., Lennon, G. G., Albala, J. S., Shen, Z., and Schild, D. (1998). Isolation and characterization of RAD51C, a new human member of the RAD51 family of related genes. Nucleic Acids Res *26*, 1179-1184.

Egner, A., Verrier, S., Goroshkov, A., Soling, H. D. and Hell, S. W. (2004) 4Pi-microscopy of the Golgi apparatus in live mammalian cells. J Struct Biol *147*, 70-76.

Essers, J., Houtsmuller, A. B., van Veelen, L., Paulusma, C., Nigg, A. L., Pastink, A., Vermeulen, W., Hoeijmakers, J. H., and Kanaar, R. (2002). Nuclear dynamics of RAD52 group homologous recombination proteins in response to DNA damage. EMBO J *21*, 2030-2037.

Fernandez-Capetillo, O., Celeste, A. and Nussenzweig, A. (2003) Focusing on foci: H2AX and the recruitment of DNA-damage response factors. Cell Cycle *2*, 426-427

Forget, A. L., Bennett, B. T., and Knight, K. L. (2004). Xrcc3 is recruited to DNA double strand breaks early and independent of Rad51. J Cell Biochem *93*, 429-436.

French, C. A., Masson, J. Y., Griffin, C. S., O'Regan, P., West, S. C., and Thacker, J. (2002). Role of mammalian RAD51L2 (RAD51C) in recombination and genetic stability. J Biol Chem *277*, 19322-19330.

French, C. A., Tambini, C. E., and Thacker, J. (2003). Identification of functional domains in the RAD51L2 (RAD51C) protein and its requirement for gene conversion. J Biol Chem *278*, 45445-45450.

Giannakakou, P., Nakano, M., Nicolaou, K. C., O'Brate, A., Yu, J., Blagosklonny, M. V., Greber, U. F., and Fojo, T. (2002). Enhanced microtubule-dependent trafficking and p53 nuclear accumulation by suppression of microtubule dynamics. Proc Natl Acad Sci U S A *99*, 10855-10860.

Godthelp, B. C., Artwert, F., Joenje, H., and Zdzienicka, M. Z. (2002). Impaired DNA damage-induced nuclear Rad51 foci formation uniquely characterizes Fanconi anemia group D1. Oncogene *21*, 5002-5005.

Golub, E. I., Gupta, R. C., Haaf, T., Wold, M. S., and Radding, C. M. (1998). Interaction of human rad51 recombination protein with single-stranded DNA binding protein, RPA. Nucleic Acids Res *26*, 5388-5393.

Gugel, H., Bewersdorf, J., Jacobs, S., Engelhardt, J., Storz, R., and Hell, S. W. (2004) Cooperative 4Pi excitation and detection yields sevenfold sharper optical sections in live-cell microscopy. Biophys J *87*, 4146-4152.

Gundersen, G. G., and Cook, T. A. (1999). Microtubules and signal transduction. Curr Opin Cell Biol *11*, 81-94.

Haaf, T., Golub, E. I., Reddy, G., Radding, C. M., and Ward, D. C. (1995). Nuclear foci of mammalian Rad51 recombination protein in somatic cells after DNA damage and its localization in synaptonemal complexes. Proc Natl Acad Sci U S A *92*, 2298-2302.

Haaf, T., Raderschall, E., Reddy, G., Ward, D. C., Radding, C. M., and Golub, E. I. (1999). Sequestration of mammalian Rad51-recombination protein into micronuclei. J Cell Biol *144*, 11-20.

Hashizume, R., Fukuda, M., Maeda, I., Nishikawa, H., Oyake, D., Yabuki, Y., Ogata, H., and Ohta, T. (2001). The RING heterodimer BRCA1-BARD1 is a ubiquitin ligase inactivated by a breast cancer-derived mutation. J Biol Chem *276*, 14537-14540.

Hauptner, A., Dietzel, S., Drexler, G. A., Reichart, P., Krucken, R., Cremer, T., Friedl, A. A., and Dollinger, G. (2004). Microirradiation of cells with energetic heavy ions. Radiat Environ Biophys *42*, 237-245.

Hays, S. L., Firmenich, A. A., and Berg, P. (1995) Complex formation in yeast double-strand break repair: participation of Rad51, Rad52, Rad55 and Rad57 proteins. Proc Natl Acad Sci, USA 92, 6925-6929.

Hell, S. W. (1990) European Patent 0491289.

Hell, S. and Stelzer, E. H. K. (1992) Fundamental improvement of resolution with a 4Pi-confocal fluorescence microscope using two-photon excitation. Opt Commun *93*, 277-282.

Henry-Mowatt, J., Jackson, D., Masson, J. Y., Johnson, P. A., Clements, P. M., Benson, F. E., Thompson, L. H., Takeda, S., West, S. C., and Caldecott, K. W. (2003). XRCC3 and Rad51 modulate replication fork progression on damaged vertebrate chromosomes. Mol Cell *11*, 1109-1117.

Huebert, D. J. and Bernstein, B. E. Genomic views of chromatin. Curr Opin Genet Dev *15*, 476-481.

Hussain, S., Wilson, J. B., Medhurst, A. L., Hejna, J., Witt, E., Ananth, S., Davies, A., Masson, J. Y., Moses, R., West, S. C., de Winter, J. P., Ashworth, A., Jones, N. J., and Mathew, C. G. (2004). Direct interaction of FANCD2 with BRCA2 in DNA damage response pathways. Hum Mol Genet *13*, 1241-1248.

Hussain, S., Witt, E., Huber, P. A., Medhurst, A. L., Ashworth, A., and Mathew, C. G. (2003). Direct interaction of the Fanconi anaemia protein FANCG with BRCA2/FANCD1. Hum Mol Genet *12*, 2503-2510.

Irinopoulou, T., Vassy, J., Beil, M., Nicolopoulou, P., Encaoua, D. and Rigaut, J. P. (1997) Three-dimensional DNA image cytometry by confocal scanning laser microscopy in thick tissue blocks of prostatic lesions. Cytometry *27*, 99-105

Ivanov, A., Cragg, M. S., Erenpreisa, J., Emzinsh, D., Lukman, H., and Illidge, T. M. (2003). Endopolyploid cells produced after severe genotoxic damage have the potential to repair DNA double strand breaks. J Cell Sci *116*, 4095-4106.

Johnson, R. D., and Symington, L. S. (1995) Functional differences and interactions among the putative RecA homologs Rad51, Rad55 and Rad57. Mol Cell Biol 15, 4843-4850.

Johnson, R. D., and Jasin, M. (2001). Double-strand-break-induced homologous recombination in mammalian cells. Biochem Soc Trans *29*, 196-201.

Kagawa, W., Kurumizaka, H., Ishitani, R., Fukai, S., Nureki, O., Shibata, T., and Yokoyama, S. (2002). Crystal structure of the homologous-pairing domain from the human Rad52 recombinase in the undecameric form. Mol Cell *10*, 359-371.

Kanamoto, T., Hellman, U., Heldin, C. H., and Souchelnytskyi, S. (2002). Functional proteomics of transforming growth factor-beta1-stimulated Mv1Lu epithelial cells: Rad51 as a target of TGFbeta1-dependent regulation of DNA repair. EMBO J *21*, 1219-1230.

Kao, G. D., McKenna, W. G., Guenther, M. G., Muschel, R. J., Lazar, M. A., and Yen, T. J. (2003). Histone deacetylase 4 interacts with 53BP1 to mediate the DNA damage response. J Cell Biol *160*, 1017-1027.

Keogh, M. C., Kim, J. A., Downey, M., Fillingham, J., Chowdhury, D., Harrison, J. C., Onishi, M., Datta, N., Galicia, S., Emili, A., Lieberman, J., Shen, X., Buratowski, S., Haber, J. E., Durocher, D., Greenblatt, J. F. and Krogan, N. J. (2006) A phosphatase complex that dephosphorylates gammaH2AX regulates DNA damage checkpoint recovery. Nature *439*, 497-501.

Kim, J. S., Krasieva, T. B., LaMorte, V., Taylor, A. M. and Yokomori, K. Specific recruitment of human cohesin to laser-induced DNA damage. (2002) J Biol Chem *277*, 45149-45153.

Knowles, D. W., Sudar, D., Bator-Kelly, C., Bissell, M. J. and Lelievre, S. A. Automated local bright feature image analysis of nuclear protein distribution identifies changes in tissue phenotype. Proc Natl Acad Sci U S A *103*, 4445-4450

Kovalenko, O. V., Plug, A. W., Haaf, T., Gonda, D. K., Ashley, T., Ward, D. C., Radding, C. M., and Golub, E. I. (1996). Mammalian ubiquitin-conjugating enzyme Ubc9 interacts with Rad51 recombination protein and localizes in synaptonemal complexes. Proc Natl Acad Sci U S A *93*, 2958-2963.

Kraakman-van der Zwet, M., Overkamp, W. J., van Lange, R. E., Essers, J., van Duijn-Goedhart, A., Wiggers, I., Swaminathan, S., van Buul, P. P., Errami, A., Tan, R. T., Jaspers, N. G., Sharan, S. K., Kanaar, R., and Zdzienicka, M. Z. (2002). Brca2 (XRCC11) deficiency results in radioresistant DNA synthesis and a higher frequency of spontaneous deletions. Mol Cell Biol *22*, 669-679.

Krogan, N. J., Lam, M. H., Fillingham, J., Keogh, M. C., Gebbia, M., Li, J., Datta, N., Cagney, G., Buratowski, S., Emili, A., and Greenblatt, J. F. (2004). Proteasome involvement in the repair of DNA double-strand breaks. Mol Cell *16*, 1027-1034.

Krogh, B. O. and Symington, L. S. (2004) Recombination proteins in yeast. Annu. Rev. Genet. *38*, 233-271.

Kruhlak, M. J., Celeste, A., Dellaire, G., Fernandez-Capetillo, O., Muller, W. G., McNally, J. G., Bazett-Jones, D. P. and Nussenzweig, A. (2006) Changes in chromatin structure and mobility in living cells at sites of DNA double-strand breaks. J Cell Biol *172*, 823-834.

Kurumizaka, H., Ikawa, S., Nakada, M., Eda, K., Kagawa, W., Takata, M., Takeda, S., Yokoyama, S., and Shibata, T. (2001). Homologous-pairing activity of the human DNA-repair proteins Xrcc3.Rad51C. Proc Natl Acad Sci U S A *98*, 5538-5543.

Lam, M. H., Thomas, R. J., Loveland, K. L., Schilders, S., Gu, M., Martin, T. J., Gillespie, M. T., and Jans, D. A. (2002). Nuclear transport of parathyroid hormone (PTH)-related protein is dependent on microtubules. Mol Endocrinol *16*, 390-401.

Lam, Y.A., Lawson, T.G., Velayutham, M., Zweier, J. L. and Pickart, C. M. (2002). A proteasomal ATPase subunit recognizes the polyubiquitin degradation signal. Nature *416*, 763-767.

Lesca, C., Germanier, M., Raynaud-Messina, B., Pichereaux, C., Etievant, C., Emond, S., Burlet-Schiltz, O., Monsarrat, B., Wright, M., and Defais, M. (2005). DNA damage induce gamma-tubulin-RAD51 nuclear complexes in mammalian cells. Oncogene *24*, 5165-5172.

Li, M. J., and Maizels, N. (1997). Nuclear Rad51 foci induced by DNA damage are distinct from Rad51 foci associated with B cell activation and recombination. Exp Cell Res *237*, 93-100.

Lim, D. S. and Hasty, P. (1996) A mutation in mouse rad51 results in an early embryonic lethal that is suppressed by a mutation in p53. Mol. Cell. Biol. *16*, 7133-7143.

Lio, Y. C., Schild, D., Brenneman, M. A., Redpath, J. L., and Chen, D. J. (2004). Human Rad51C deficiency destabilizes XRCC3, impairs recombination, and radiosensitizes S/G2-phase cells. J Biol Chem *279*, 42313-42320.

Lisby, M., Mortensen, U. H. and Rothstein, R. (2003) Colocalization of multiple DNA double-strand breaks at a single Rad52 repair centre. Nat Cell Biol *5*, 572-577

Liu, N., Lamerdin, J. E., Tebbs, R. S., Schild, D., Tucker, J. D., Shen, M. R., Brookman, K. W., Siciliano, M. J., Walter, C. A., Fan, W., Narayana, L. S., Zhou, Z. Q., Adamson, A. W., Sorensen, K. J., Chen, D. J., Jones, N. J., and Thompson, L. H. (1998). XRCC2 and

XRCC3, new human Rad51-family members, promote chromosome stability and protect against DNA cross-links and other damages. Mol Cell *1*, 783-793.

Liu, N., and Lim, C. S. (2005). Differential roles of XRCC2 in homologous recombinational repair of stalled replication forks. J Cell Biochem *95*, 942-954.

Liu, N., Schild, D., Thelen, M. P., and Thompson, L. H. (2002). Involvement of Rad51C in two distinct protein complexes of Rad51 paralogs in human cells. Nucleic Acids Res *30*, 1009-1015.

Liu, Y., Masson, J. Y., Shah, R., O'Regan, P., and West, S. C. (2004a). RAD51C is required for Holliday junction processing in mammalian cells. Science *303*, 243-246.

Liu, Y., Stasiak, A. Z., Masson, J. Y., McIlwraith, M. J., Stasiak, A., and West, S. C. (2004b). Conformational changes modulate the activity of human RAD51 protein. J Mol Biol *337*, 817-827.

Lorick, K. L., Jensen, J. P., Fang, S., Ong, A. M., Hatakeyama, S., and Weissman, A. M. (1999). RING fingers mediate ubiquitin-conjugating enzyme (E2)-dependent ubiquitination. Proc Natl Acad Sci U S A *96*, 11364-11369.

Lovettt, S. T., and Mortimer, R. K. (1987) Characterization of null mutants of the RAD55 gene of *Saccharomyces cereviae*: effects of temperature, osmotic strength and mating type. Genetics *116*, 547-553.

Lusetti, S., Hobbs, M. D., Stohl, E. A., Chitteni-Pattu, S., Inman, R. B., Seifert, H. S., and Cox, M. M. (2006) The RecF protein antagonizes RecX function via direct interaction. Mol Cell *21*, 41-50.

Marmorstein, L. Y., Ouchi, T., and Aaronson, S. A. (1998). The BRCA2 gene product functionally interacts with p53 and RAD51. Proc Natl Acad Sci U S A *95*, 13869-13874.

Martini, N., Bewersdorf, J. and Hell, S. W. A new high-aperture glycerol immersion lens and its application to 3D-fluorescence microscopy. J. Microsc. *206*, 146-151

Maser, R. S., Monsen, K. J., Nelms, B. E., and Petrini, J. H. (1997). hMre11 and hRad50 nuclear foci are induced during the normal cellular response to DNA double-strand breaks. Mol Cell Biol *17*, 6087-6096.

Masson, J. Y., Stasiak, A. Z., Stasiak, A., Benson, F. E., and West, S. C. (2001a). Complex formation by the human RAD51C and XRCC3 recombination repair proteins. Proc Natl Acad Sci U S A *98*, 8440-8446.

Masson, J. Y., Tarsounas, M. C., Stasiak, A. Z., Stasiak, A., Shah, R., McIlwraith, M. J., Benson, F. E., and West, S. C. (2001b). Identification and purification of two distinct complexes containing the five RAD51 paralogs. Genes Dev *15*, 3296-3307.

McGrew, D. A., and Knight, K. L. (2003). Molecular design and functional organization of the RecA protein. Crit Rev Biochem Mol Biol *38*, 385-432.

Miller, K. A., Hinz, J. M., Yamada, N. A., Thompson, L. H., and Albala, J. S. (2005). Nuclear localization of Rad51B is independent of Rad51C and BRCA2. Mutagenesis *20*, 57-63.

Miller, K. A., Yoshikawa, D. M., McConnell, I. R., Clark, R., Schild, D., and Albala, J. S. (2002). RAD51C interacts with RAD51B and is central to a larger protein complex in vivo exclusive of RAD51. J Biol Chem *277*, 8406-8411.

Morrison, C., Shinohara, A., Sonoda, E., Yamaguchi-Iwai, Y., Takata, M., Weichselbaum, R. R., and Takeda, S. (1999). The essential functions of human Rad51 are independent of ATP hydrolysis. Mol Cell Biol *19*, 6891-6897.

Moynahan, M. E., Pierce, A. J., and Jasin, M. (2001). BRCA2 is required for homology-directed repair of chromosomal breaks. Mol Cell *7*, 263-272.

Munkel, C., Eils, R., Dietzel, S., Zink, D., Mehring, C., Wedemann, G., Cremer, T. and Langowski, J. (1999) Compartmentalization of interphase chromosomes observed in simulation and experiment. J Mol Biol *285*, 1053-1065.

Nelms, B. E., Maser, R. S., MacKay, J. F., Lagally, M. G. and Petrini, J. H. (1998) In situ visualization of DNA double-strand break repair in human fibroblasts. Science *280*, 590-592.

Nussenzweig, A. and Paull, T. DNA repair: tails of histones lost. (2006) Nature *439*, 406-407.

O'Driscoll, M. and Jeggo, P. A. (2006) The role of double-strand break repair - insights from human genetics. Nat Rev Genet *7*, 45-54.

O'Regan, P., Wilson, C., Townsend, S., and Thacker, J. (2001). XRCC2 is a nuclear RAD51-like protein required for damage-dependent RAD51 focus formation without the need for ATP binding. J Biol Chem *276*, 22148-22153.

Paques, F., and Haber, J. E. (1999). Multiple pathways of recombination induced by double-strand breaks in Saccharomyces cerevisiae. Microbiol Mol Biol Rev *63*, 349-404.

Patel, K. J., Yu, V. P., Lee, H., Corcoran, A., Thistlethwaite, F. C., Evans, M. J., Colledge, W. H., Friedman, L. S., Ponder, B. A., and Venkitaraman, A. R. (1998). Involvement of Brca2 in DNA repair. Mol Cell *1*, 347-357.

Paull, T. T., Rogakou, E. P., Yamazaki, V., Kirchgessner, C. U., Gellert, M., and Bonner, W. M. (2000). A critical role for histone H2AX in recruitment of repair factors to nuclear foci after DNA damage. Curr Biol *10*, 886-895.

Pellegrini, L., Yu, D. S., Lo, T., Anand, S., Lee, M., Blundell, T. L., and Venkitaraman, A. R. (2002). Insights into DNA recombination from the structure of a RAD51-BRCA2 complex. Nature *420*, 287-293.

Peterson, C. L. and Cote, J. (2004) Cellular machineries for chromosomal DNA repair. Genes Dev *18*, 602-616.

Petes, T. D., Malone, R. E., and Symington, L. S. (1991) Recombination in yeast. in The Molecular and Cellular Biology of the Yeast *Saccharomyces*, J. R. Broach, J. R. Pringle, and E. W. Jones, eds. (New York: Cold Spring Harbor Laboratory press), pp. 407-522.

Pichierri, P., Averbeck, D., and Rosselli, F. (2002). DNA cross-link-dependent RAD50/MRE11/NBS1 subnuclear assembly requires the Fanconi anemia C protein. Hum Mol Genet *11*, 2531-2546.

Pierce, A. J., Johnson, R. D., Thompson, L. H., and Jasin, M. (1999). XRCC3 promotes homology-directed repair of DNA damage in mammalian cells. Genes Dev *13*, 2633-2638.

Pockwinse, S. M., Rajgopal, A., Young, D. W., Mujeeb, K. A., Nickerson, J., Javed, A., Redick, S., Lian, J. B., van Wijnen, A. J., Stein, J. L., Stein, G. S., and Doxsey, S. J. (2005). Microtubule-dependent nuclear-cytoplasmic shuttling of Runx2. J Cell Physiol

Rahman, N., and Stratton, M. R. (1998). The genetics of breast cancer susceptibility. Annu Rev Genet *32*, 95-121.

Rijkers, T., Van Den Ouweland, J., Morolli, B., Rolink, G., Baarends, W. M., Van Sloun, P. P., Lohman, P. H., and Pastink, A. (1998) Targeted inactivation of mouse *RAD52* reduces homologous recombination but not resistance to ionizing radiation. Mol Cell Biol *18*, 6423-6429.

Roczniak-Ferguson, A., and Reynolds, A. B. (2003). Regulation of p120-catenin nucleocytoplasmic shuttling activity. J Cell Sci *116*, 4201-4212.

Rogakou, E. P., Boon, C., Redon, C. and Bonner, W. M. (1999) Megabase chromatin domains involved in DNA double-strand breaks in vivo. J Cell Biol *146*, 905-916.

Rogakou, E. P., Pilch, D. R., Orr, A. H., Ivanova, V. S., and Bonner, W. M. (1998). DNA double-stranded breaks induce histone H2AX phosphorylation on serine 139. J Biol Chem *273*, 5858-5868.

Ruffner, H., Joazeiro, C. A., Hemmati, D., Hunter, T., and Verma, I. M. (2001). Cancer-predisposing mutations within the RING domain of BRCA1: loss of ubiquitin protein ligase activity and protection from radiation hypersensitivity. Proc Natl Acad Sci U S A *98*, 5134-5139.

Schild, D., Lio, Y. C., Collins, D. W., Tsomondo, T., and Chen, D. J. (2000). Evidence for simultaneous protein interactions between human Rad51 paralogs. J Biol Chem *275*, 16443-16449.

Sharan, S. K., Morimatsu, M., Albrecht, U., Lim, D. S., Regel, E., Dinh, C., Sands, A., Eichele, G., Hasty, P., and Bradley, A. (1997). Embryonic lethality and radiation hypersensitivity mediated by Rad51 in mice lacking Brca2. Nature *386*, 804-810.

Shen, Z., Pardington-Purtymun, P. E., Comeaux, J. C., Moyzis, R. K., and Chen, D. J. (1996). UBL1, a human ubiquitin-like protein associating with human RAD51/RAD52 proteins. Genomics *36*, 271-279.

Shroff, R., Arbel-Eden, A., Pilch, D., Ira, G., Bonner, W. M., Petrini, J. H., Haber, J. E. and Lichten, M. (2004) Distribution and dynamics of chromatin modification induced by a defined DNA double-strand break. Curr Biol *14*, 1703-1711.

Sigurdsson, S., Van Komen, S., Bussen, W., Schild, D., Albala, J. S., and Sung, P. (2001). Mediator function of the human Rad51B-Rad51C complex in Rad51/RPA-catalyzed DNA strand exchange. Genes Dev *15*, 3308-3318.

Sonoda, E., Takata, M., Yamashita, Y. M., Morrison, C., and Takeda, S. (2001). Homologous DNA recombination in vertebrate cells. Proc Natl Acad Sci U S A *98*, 8388-8394.

Spain, B. H., Larson, C. J., Shihabuddin, L. S., Gage, F. H., and Verma, I. M. (1999). Truncated BRCA2 is cytoplasmic: implications for cancer-linked mutations. Proc Natl Acad Sci U S A *96*, 13920-13925.

Stark, J. M., Hu, P., Pierce, A. J., Moynahan, M. E., Ellis, N., and Jasin, M. (2002) ATP hydrolysis by mammalian RAD51 has a key role during homology-directed DNA repair. J. Biol. Chem. 277, 20185-20194.

Strom, L., Lindroos, H. B., Shirahige, K. & Sjogren, C. (2004) Postreplicative recruitment of cohesin to double-strand breaks is required for DNA repair. Mol Cell *16*, 1003-1015.

Stucki, M. & Jackson, S. P. (2006) gammaH2AX and MDC1: Anchoring the DNA-damage-response machinery to broken chromosomes. DNA Repair (Amst) *5*, 534-543.

Sung, P. (1997) Yeast Rad55 and Rad57 proteins form a heterodimer that functions with replication protein A to promote DNA strand exchange by Rad51 recombinase. Genes Dev *11*, 1111-1121.

Sung, P., Krejci, L., Van Komen, S., and Sehorn, M. G. (2003). Rad51 recombinase and recombination mediators. J Biol Chem *278*, 42729-42732.

Symington, L. S. (2002) Role of *RAD52* epistasis group genes in homologous recombination and double-strand break repair. Micro. Molec. Biol. Rev. *66*, 630-670.

Takata, M., Sasaki, M. S., Tachiiri, S., Fukushima, T., Sonoda, E., Schild, D., Thompson, L. H., and Takeda, S. (2001). Chromosome instability and defective recombinational repair in knockout mutants of the five Rad51 paralogs. Mol Cell Biol *21*, 2858-2866.

Tambini, C. E., George, A. M., Rommens, J. M., Tsui, L. C., Scherer, S. W., and Thacker, J. (1997). The XRCC2 DNA repair gene: identification of a positional candidate. Genomics *41*, 84-92.

Tarsounas, M., Davies, A. A., and West, S. C. (2004b). RAD51 localization and activation following DNA damage. Philos Trans R Soc Lond B Biol Sci *359*, 87-93.

Tarsounas, M., Davies, D., and West, S. C. (2003). BRCA2-dependent and independent formation of RAD51 nuclear foci. Oncogene *22*, 1115-1123.

Tarsounas, M., Munoz, P., Claas, A., Smiraldo, P. G., Pittman, D. L., Blasco, M. A., and West, S. C. (2004a). Telomere maintenance requires the RAD51D recombination/repair protein. Cell *117*, 337-347.

Tashiro, S., Walter, J., Shinohara, A., Kamada, N., and Cremer, T. (2000). Rad51 accumulation at sites of DNA damage and in postreplicative chromatin. J Cell Biol *150*, 283-291.

Tebbs, R. S., Zhao, Y., Tucker, J. D., Scheerer, J. B., Siciliano, M. J., Hwang, M., Liu, N., Legerski, R. J., and Thompson, L. H. (1995). Correction of chromosomal instability and sensitivity to diverse mutagens by a cloned cDNA of the XRCC3 DNA repair gene. Proc Natl Acad Sci U S A *92*, 6354-6358.

Thacker, J. (1999). A surfeit of RAD51-like genes? Trends Genet *15*, 166-168.

Thacker, J. (2005). The RAD51 gene family, genetic instability and cancer. Cancer Lett *219*, 125-135.

Thiriet, C. and Hayes, J. J. (2005) Chromatin in need of a fix: phosphorylation of H2AX connects chromatin to DNA repair. Mol Cell *18*, 617-622.

Thompson, L. H., and Schild, D. (2001). Homologous recombinational repair of DNA ensures mammalian chromosome stability. Mutat Res *477*, 131-153.

Thompson, L. H., and Schild, D. (2002). Recombinational DNA repair and human disease. Mutat Res *509*, 49-78.

Tsuzuki, T., Fujii, Y., Sakumi, K., Tominaga, Y., Nakao, K., Sekiguchi, M., Matsushiro, A., Yoshimura, Y., and Morita., T. (1996) Targeted disruption of the Rad51 gene leads to lethality in embryonic mice. Proc Natl Acad Sci USA *93*, 6236-6240.

Unal, E., Arbel-Eden, A., Sattler, U., Shroff, R., Lichten, M., Haber, J. E. and Koshland, D. (2004) DNA damage response pathway uses histone modification to assemble a double-strand break-specific cohesin domain. Mol Cell *16*, 991-1002.

van Veelen, L. R., Cervelli, T., van de Rakt, M. W., Theil, A. F., Essers, J., and Kanaar, R. (2005). Analysis of ionizing radiation-induced foci of DNA damage repair proteins. Mutat Res *574*, 22-33.

West, S. C. (2003). Molecular views of recombination proteins and their control. Nat Rev Mol Cell Biol *4*, 435-445.

Wiese, C., Collins, D. W., Albala, J. S., Thompson, L. H., Kronenberg, A., and Schild, D. (2002). Interactions involving the Rad51 paralogs Rad51C and XRCC3 in human cells. Nucleic Acids Res *30*, 1001-1008.

Wolner, B., van Komen, S., Sung, P., and Peterson, C. L. (2003) Recruitment of the recombinational repair machinery to a DNA double-strand break in yeast. Mol Cell *12*, 221-232.

Wong, A. K., Pero, R., Ormonde, P. A., Tavtigian, S. V., and Bartel, P. L. (1997). RAD51 interacts with the evolutionarily conserved BRC motifs in the human breast cancer susceptibility gene brca2. J Biol Chem *272*, 31941-31944.

Wu, G., Jiang, X., Lee, W. H., and Chen, P. L. (2003). Assembly of functional ALT-associated promyelocytic leukemia bodies requires Nijmegen Breakage Syndrome 1. Cancer Res *63*, 2589-2595.

Wu, Y., He, Y., Moya, I. A., Qian, X., and Luo, Y. (2004). Crystal structure of archaeal recombinase RADA: a snapshot of its extended conformation. Mol Cell *15*, 423-435.

Yamaguchi-Iwai, Y., Sonoda, E., Buerstedde, J. M., Bezzubova, O., Morrison, C., Takata, M., Shinohara, A., and Takeda, S. (1998) Homologous recombination, but not DNA repair, is reduced in vertebrate cells deficient in *RAD52*. Mol Cell Biol. *18*, 6430-6435.

Yang, H., Jeffrey, P. D., Miller, J., Kinnucan, E., Sun, Y., Thoma, N. H., Zheng, N., Chen, P. L., Lee, W. H., and Pavletich, N. P. (2002). BRCA2 function in DNA binding and recombination from a BRCA2-DSS1-ssDNA structure. Science *297*, 1837-1848.

Yonetani, Y., Hochegger, H., Sonoda, E., Shinya, S., Yoshikawa, H., Takeda, S., and Yamazoe, M. (2005). Differential and collaborative actions of Rad51 paralog proteins in cellular response to DNA damage. Nucleic Acids Res *33*, 4544-4552.

Yoshihara, T., Ishida, M., Kinomura, A., Katsura, M., Tsuruga, T., Tashiro, S., Asahara, T., and Miyagawa, K. (2004). XRCC3 deficiency results in a defect in recombination and increased endoreduplication in human cells. EMBO J *23*, 670-680.

Yoshikawa, K., Ogawa, T., Baer, R., Hemmi, H., Honda, K., Yamauchi, A., Inamoto, T., Ko, K., Yazumi, S., Motoda, H., Kodama, H., Noguchi, S., Gazdar, A. F., Yamaoka, Y., and

Takahashi, R. (2000). Abnormal expression of BRCA1 and BRCA1-interactive DNA-repair proteins in breast carcinomas. Int J Cancer *88*, 28-36.

Yu, D. S., Sonoda, E., Takeda, S., Huang, C. L., Pellegrini, L., Blundell, T. L., and Venkitaraman, A. R. (2003). Dynamic control of Rad51 recombinase by self-association and interaction with BRCA2. Mol Cell *12*, 1029-1041.

Yuan, S. S., Chang, H. L., and Lee, E. Y. (2003). Ionizing radiation-induced Rad51 nuclear focus formation is cell cycle-regulated and defective in both ATM(-/-) and c-Abl(-/-) cells. Mutat Res *525*, 85-92.

Yuan, S. S., Lee, S. Y., Chen, G., Song, M., Tomlinson, G. E., and Lee, E. Y. (1999). BRCA2 is required for ionizing radiation-induced assembly of Rad51 complex in vivo. Cancer Res *59*, 3547-3551.

Zamansky, G. B., Nguyen, U., and Chou, I. N. (1992). An immunofluorescence study of the effects of ultraviolet radiation on the organization of microfilaments, keratin intermediate filaments, and microtubules in human keratinocytes. Cell Motil Cytoskeleton *22*, 296-306.

Zamansky, G. B., Perrino, B. A., and Chou, I. N. (1991). Disruption of cytoplasmic microtubules by ultraviolet radiation. Exp Cell Res *195*, 269-273.

Zhang, H., Tombline, G., and Weber, B. L. (1998). BRCA1, BRCA2, and DNA damage response: collision or collusion? Cell *92*, 433-436.

Ziegelbauer, J., Shan, B., Yager, D., Larabell, C., Hoffmann, B., and Tjian, R. (2001). Transcription factor MIZ-1 is regulated via microtubule association. Mol Cell *8*, 339-349.